Mechanotransduction via Airway Epithelial Cells: The Effect of Compressive Stress

by

Nikola Kojić

M.S. Mechanical Engineering, MIT 2003

Submitted to the Harvard-Massachusetts Institute of Technology Division of Health Sciences and Technology
in partial fulfillment of the requirements for the degree of

Doctor of Philosophy

in Biomedical Engineering

at the
Massachusetts Institute of Technology
June 2007

Signature of author: _____
Harvard-MIT Division of Health Sciences and Technology
May, 2007

Certified by: _____
Jeffrey M. Drazen, M.D.
Distinguished Parker B. Francis Professor of Medicine, Harvard MedicalSchool,
Thesis Supervisor

Accepted by: _____
Martha L. Gray, Ph.D.
Edward Hood Taplin Professor of Medical and Electrical Engineering
Director, Harvard-MIT Division of Health Sciences and Technology

Mechanotransduction via Airway Epithelial Cells: The Effect of Compressive Stress

by

Nikola Kojić

Submitted to the Harvard-Massachusetts Institute of Technology
Division of Health Sciences and Technology on May 16, 2007 in partial fulfillment of the requirements for the degree of Doctor of Philosophy in Biomedical Engineering

ABSTRACT

A classic finding in asthma is a change in the structural organization of the airway epithelium. This complex process known as airway remodeling is not fully understood, and we believe that the forces accompanying airway constriction activate the epithelium and contribute to airway remodeling. To better understand this mechanotransduction mechanism we used an in vitro system of cultured normal human bronchial epithelial cells that could simulate compressive stresses experienced by the epithelium during bronchoconstriction. The application of a transcellular pressure gradient (10-50cmH_2O) for 10 minutes resulted in transient activation of the epidermal growth factor receptor (EGFR) – MAP kinase (ERK) signaling pathway. Furthermore, specialized real-time high-speed imaging revealed an exponential decrease in the volume of the compliant lateral intercellular space (LIS) separating neighboring cells. The measured LIS volume collapse curves were directly inputted into 2-D and 3-D numerical finite element models, whose output was EGFR-ligand concentration dynamics in the LIS. During the first three minutes under pressure, the calculated increase in ligand concentration (specifically HB-EGF, which is made by the cells and shed into the LIS, thereby constituting an autocrine loop with the EGFR) matched the measured phosphorylated EGFR (pEGFR) dynamics. The model thus provided crucial insight into how an observed change in LIS geometry resulted in activation of the EGFR signaling pathway. This insight, coupled to EGFR signaling models, could one day be applied to the design of novel pharmacogenetic therapeutics aimed at preventing airway over-activation and potentially hindering airway remodeling progression in asthmatic patients.

Thesis Supervisor: Jeffrey M. Drazen
Title: Distinguished Parker B. Francis Professor of Medicine, Harvard Medical School

Acknowledgements

I would like to thank my brother Aleksandar, my mother Gordana, and my father Miloš for their tremendous support over the years. I am deeply grateful to my father with whom I collaborated intensively during the past years (especially on numerical modeling using the finite element analysis software package PAK) and his entire team from the University of Kragujevac, Serbia.

I send my appreciation to my thesis advisors, Dr. Jeffrey M. Drazen and Prof. Daniel J. Tschumperlin for their guidance and understanding through my graduate years at HST. It has been a real pleasure to learn from you! I am very thankful to all of the members of my thesis committee, Profs. Roger Kamm, Peter So, and Doug Lauffenburger, for their valuable advice and supervision and Prof. Bora Mikić for his help with mass transfer. I am deeply indebted to Dr. Euiheon Chung who spent countless hours on the two-photon microscope and Austin Huang for his enormous effort in developing the image analysis algorithms.

I wish to acknowledge the entire Airway MechanoBiology Lab at the Harvard School of Public Health. It has really been an honor to be part of the lab!

Finally I would like to express gratitude to my friends from C3 for being there for me during the last ten years of my life.

Table of Contents

1. Introduction

1.1 The role of the airway epithelium in asthma

The epithelial cells that line the human airway serve as the body's natural barrier against a wide range of unwanted gases and particulate matter. But they are more than a simple barrier. In disease states, such as asthma, the structural organization of the airway epithelium may change. For example, depending on the severity of their disease, an asthmatic can have pronouncedly thickened epithelium, thickening of the collagen layer just below the true basement membrane, smooth muscle cell proliferation, and other structural changes that together decrease the airway luminal area. Furthermore, mast cells in the asthmatic epithelium can serve as a sensor for allergens, thus recruiting an immune response that can ultimately lead to progression of the disease.

Recently, another role for the epithelium has emerged whereby the epithelium is involved in mechanotransduction of forces that accompany airway constriction. Elucidating the mechanism by which the epithelium transduces mechanical stimuli, such as compressive stress, could lead to a better understanding of the role played by the epithelium in a complex disease such as asthma. Ultimately one could envision new drugs that could help break the vicious cycle involving the epithelium, the immune system and the subepithelial tissue that contributes to the progression of asthma. Also, it is likely that the mechanotransduction mechanism involved in airway epithelial cells could be applicable to other epithelial cells or tissues in the body, increasing the need to uncover the underlying processes.

1.2 The lateral intercellular space (LIS) of airway epithelial cells

Neighboring airway epithelial cells are connected at the apical surface via tight junctions that are impermeable to larger molecules, such as proteins (Tschumperlin et al., 2004; Willumsen, 1994). These tight junctions serve as the natural barrier from the outside world and their intactness is crucial for normal function. Below the tight junctions, on the lateral side of neighboring cells, lies an extracellular area termed the lateral intercellular space (LIS). The LIS is thus defined on the apical side by the tight junction, the lateral surfaces of neighboring cells, and basally by the basement membrane *in vivo*, or porous substrate on which cells are grown *in vitro* (see Fig. 1.1).

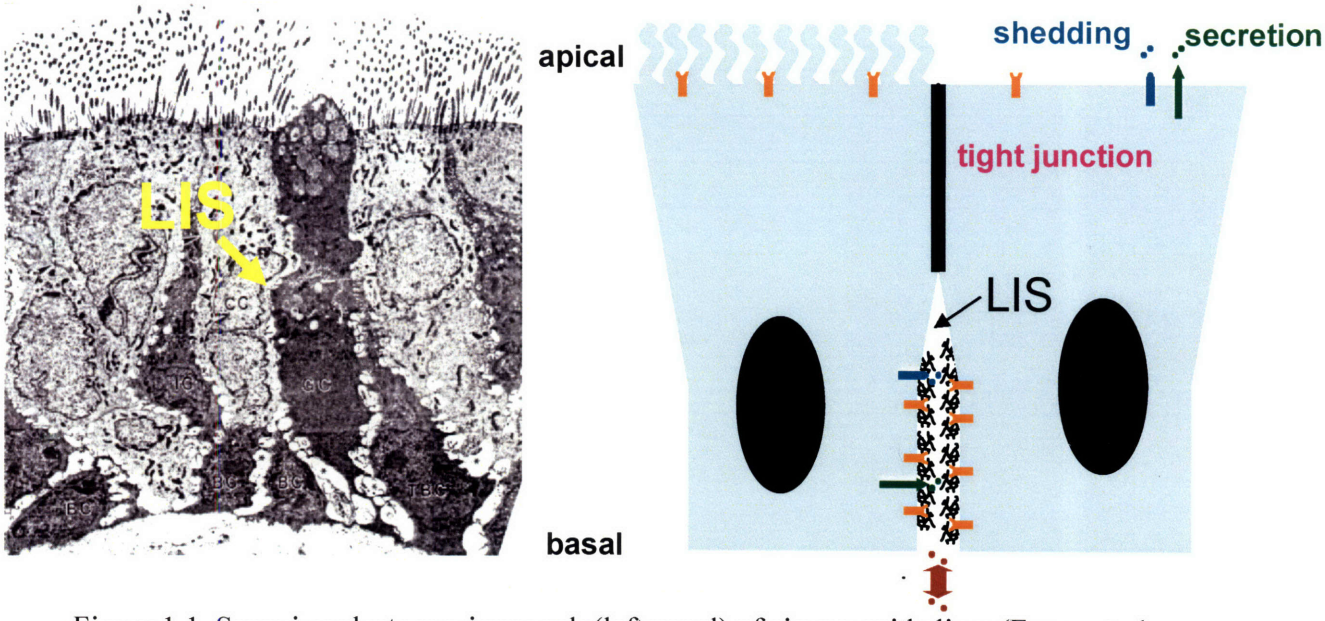

Figure 1.1 Scanning electron micrograph (left panel) of airway epithelium (Evans et al., 2001) and schematic (right panel) of the LIS separating two neighboring epithelial cells.

On the lateral surface of the cells there are a host of different membrane bound ligands and their corresponding receptors. The bound ligands are released from the cell surface into the LIS via the action of a sheddase that cleaves the connecting bond (Harris

et al., 2003). If a ligand is released into a collapsing LIS, its local concentration will increase. If the process occurs uniformly along the lateral surface, this establishes a concentration gradient in the apico-basal direction of the LIS, whereby the highest concentration is near the tight junction and the lowest, essentially zero, concentration is at the basal surface.

In the LIS, glycoprotein projections from the lateral cell surface form a mesh called the glycocalyx. The dense network of the glycocalyx could play a crucial role in hindering the diffusion of large molecules (Kovbasnjuk et al., 2000). Furthermore, being charged the glycocalyx could also provide significant chemical impedance to positively charged ligands thus hindering movement down their concentration gradient to the area below the basal surface of the cell where their concentration is likely to be quite small. The effect of the glycocalyx on the diffusion coefficient of large molecules has been studied in the LIS of canine epithelial cells, showing a several fold decrease in diffusion coefficient and thus effectively a corresponding increase in resistance to diffusion, since diffusion coefficient ~ 1/(diffusion resistance) (Kovbasnjuk et al., 2000). Although the apical surface is also rich in ligand secretion activity and glycocalyx, the presence of a large reservoir of apical fluid will keep effective concentrations low, making the most important changes that occur during prolonged bronchoconstriction in the LIS.

1.3 The EGF-receptor autocrine loop in the LIS

As mentioned above, numerous receptors extend into the LIS from the cellular surface. One type of receptor that plays a crucial role in mechanotransduction is the epidermal growth factor (EGF) receptor (Tschumperlin et al., 2002). We have previously shown

that the EGF receptor (EGFR) functions as part of an autocrine loop in normal human bronchial epithelial (NHBE) cells (see Fig. 1.2). An activating signal can be an increase in the number of ligands bound through an increase in local ligand concentration.

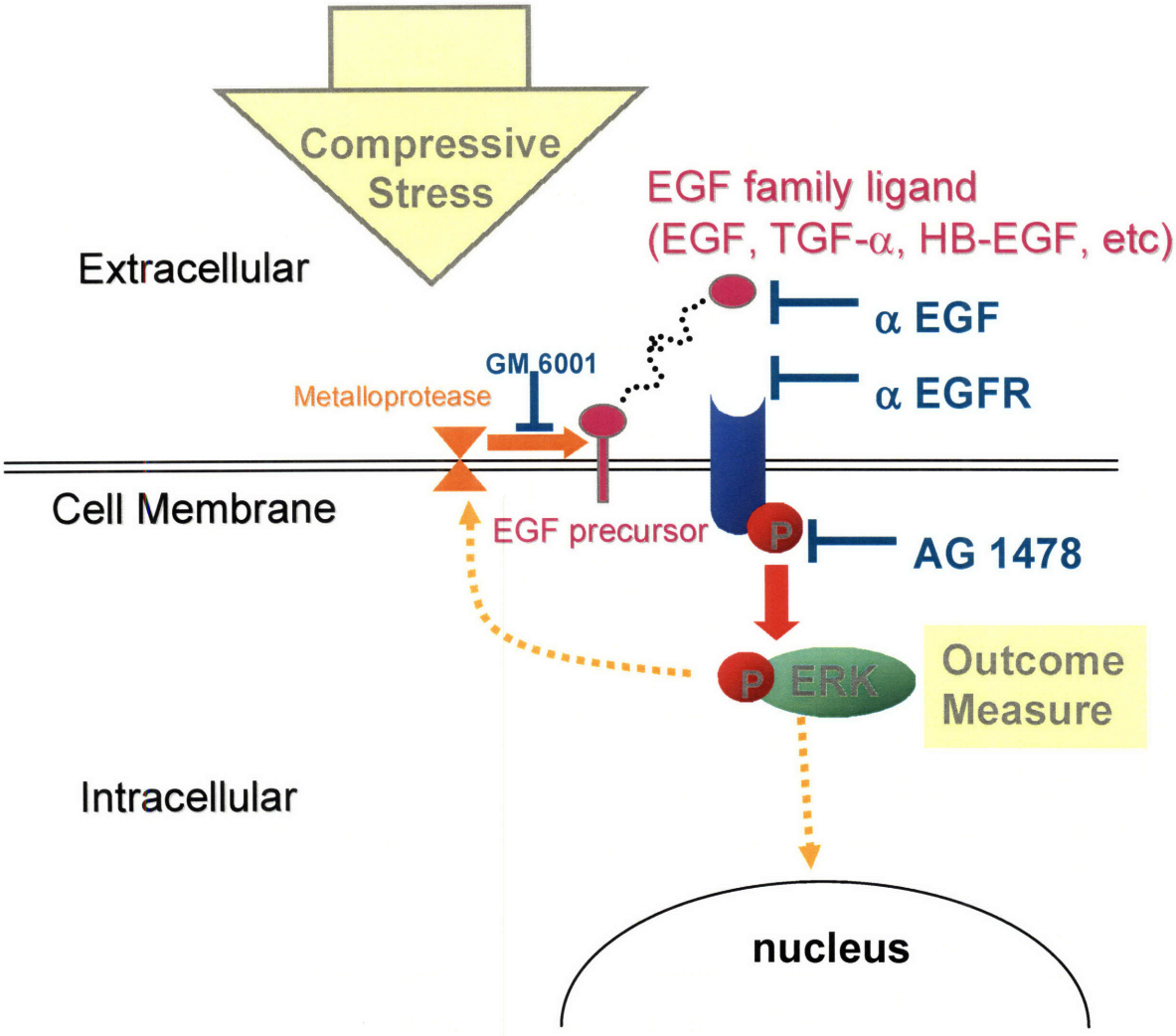

Figure 1.2 Schematic of the epidermal growth factor receptor (EGFR) autocrine loop. Light blue indicates antibodies that block various sites (GM6001 blocks metalloprotease activity, ligand and receptor antibodies are labeled with an α , AG1478 blocks EGFR phosphorylation). Phosphorylated mitogen-activated protein kinase ERK was the outcome measure.

There are at least four known members of the EGF receptor family (erbB1-4) and our main focus will be on erbB1, also known as the classical EGF receptor (referred to as EGFR) (Yarden and Sliwkowski, 2001). The EGFR contains three domains: an intrinsic kinase domain in the cytoplasm, a membrane spanning domain, and an ectodomain that binds EGFR ligands. When the ligand binds to the receptor, the monomeric receptors dimerize and phosphorylate specific cytoplasmic tyrosine residues. The phosphorylated residues then serve as a site of attachment for effector molecules that further activate signal transduction pathways (Raab and Klagsbrun, 1997). Downstream from receptor activation phosphorylation of the mitogen-activated protein kinase ERK occurs (Tschumperlin et al., 2002). The next step in the pathway is translocation of p-ERK to the nucleus (see Fig. 1.2) where it helps activate various transcription factors such as *cfos* and *jun*, hence forming the loop: **ligand-EGFR-ERK-transcription-ligand**.

Phosphorylated ERK can also signal to metalloproteases to cleave the membrane bound ligand (Harris et al., 2003) forming another autocrine loop: **ligand-EGFR-ERK-metalloprotease-ligand**. It should be noted that the two loops mentioned above could be interconnected and part of other, broader feedback mechanisms utilized by the cell to sense and appropriately respond to changes in the local environment.

1.4 Modeling the effects of compressive stress on epithelial cells in vitro

During bronchonstriction, because the basement membrane is relatively inelastic, the epithelium buckles under the influence of contracting smooth muscle. The pattern of buckling depends on the mechanical properties of the airway components as well as the thickness of the epithelium. Previous numerical modeling studies and experiments have

shown that a thicker epithelium needs smaller luminal pressures to cause airway closure (Hrousis et al., 2002; Wiggs et al., 1997). Depending on the "state" of the epithelium the cells will thus fold in different patterns (by state we mean the degree of airway remodeling that has occurred as a result of disease).

In an asthmatic airway the effect of airway remodeling is the classic rosette folding pattern (see Fig. 1.3) in which neighboring cells located in the cleft areas get squeezed against each other during bronchoconstriction. Thus they experience a compressive stress, whose magnitude is ~ 30 cmH_2O (Wiggs et al., 1997).

Figure 1.3 A constricted remodeled airway. The box indicates an area where cells get pushed against each other.

To test the effects of this compressive stress *in vitro* we use a system that can apply a pneumatic pressure gradient across cultured normal human bronchial epithelial (NHBE) cells (Ressler et al., 2000; Swartz et al., 2001). The cells (obtained from Clonetics) are grown on microporous polyester substrates (pore size 0.4 microns, Transwell-Clear).

Initially, for the first week, the cells are fed from the top and bottom. After this, for the next two weeks the cells are only fed through the bottom pores, and a cell-air interface is established at the top. This interface is a signal for the cells to polarize and differentiate into the NHBE phenotype. Once the cells are fully differentiated, the pressure device is used to apply compressive stress (see Fig. 1.4). The device consists of a plug for the transwell and a pressure tank that supplies compressed air (with 5% CO_2) through a tube going through the plug to the apical surface of the cells. The media bath below the substrate remains at atmospheric pressure, hence a pressure gradient can be established across the cells.

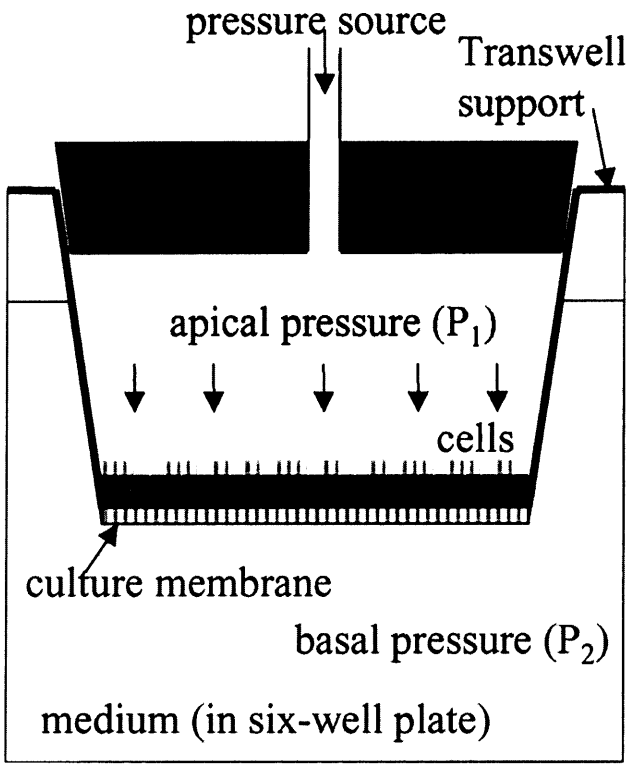

Figure 1.4 The pressure device supplies a pressure gradient P_1-P_2 across the cells.

1.5 Previous model and experimental findings

Earlier experiments with this pressure device provided several key findings about the effects of compressive stress (Tschumperlin et al., 2004):

1) The EGFR via signaling through one of its ligands, heparin-binding epidermal growth factor (HB-EGF), plays a key role in transducing the mechanical stimulus.
2) ERK phosphorylation occurs downstream of the EGFR.
3) Metalloproteases involved in shedding of ligand into the LIS are an integral part of the mechanotransduction pathway.
4) The LIS collapses, decreasing its volume substantially due to compression.

In order to have a more accurate picture of how the collapsing LIS results in increased signaling through the EGFR a 1-D LIS model based on diffusion has been put forth (Tschumperlin et al., 2004). The proposed mechanism functions as follows. Under compression, the LIS width (and thus volume) decreases pushing out the intercellular fluid basally through the porous substrate (since tight junctions form an impermeable barrier on the apical surface). HB-EGF, a large, charged protein, known to be released into the LIS remains there due to its size and charge, hence the LIS concentration of HB-EGF increases. In other words, the HB-EGF in the LIS finds itself in a smaller volume and thus the concentration increases. This increase in turn causes a greater number of HB-EGF molecules to be bound to EGFR than before the LIS collapse, effectively activating the mechanotransduction loop described above.

The model can be expressed in mathematical form assuming that diffusion of HB-EGF occurs in the apical-to-basal direction down its concentration gradient, where the

highest concentration is immediately below the impermeable tight junctions and the lowest (essentially zero) concentration is in the media bath. Hence,

$$\frac{\partial C}{\partial t} = D\frac{\partial^2 C}{\partial x^2} + \frac{2q}{w} \tag{1}$$

where C is the ligand (HB-EGF) concentration, t is time, x is the apico-basal direction, D is the diffusion coefficient of ligand through the LIS/glycocalyx matrix, q is the rate of shedding of ligand from the cell surface into the LIS and w is the LIS width. Here we assume that the LIS collapse can be regarded as two parallel plates coming closer together. From equation (1), the steady-state solution

$$C = \frac{q}{wD}(h^2 - x^2) \tag{2}$$

indicates that the concentration is inversely proportional to the width, thus C increases as w decreases; here h is the LIS height (see Fig. 1.5). Such a deduction could be viewed as satisfactory from a qualitative standpoint, but for deeper engineering insight the LIS dynamics must be taken into account.

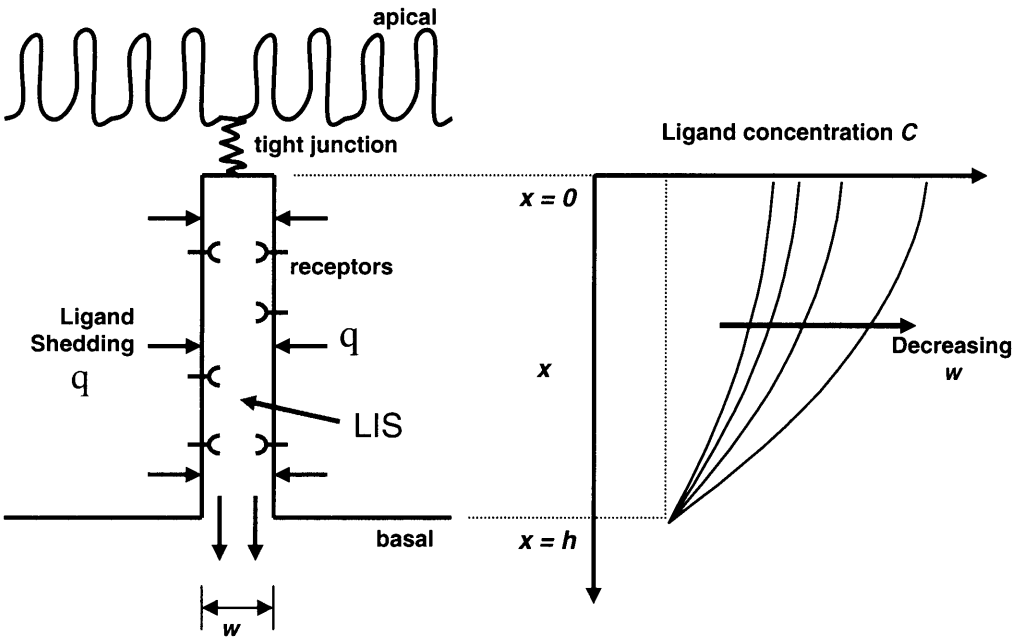

Figure 1.5 Schematic of the initial LIS model (left panel) and the corresponding steady-state solutions (right panel).

1.6 Rationale for a focus on HB-EGF

Previous experiments (Tschumperlin et al., 2004; Tschumperlin and Drazen, 2001; Tschumperlin et al., 2002) have shown that HB-EGF is the key EGFR ligand in the mechanotransduction pathway. These experiments revealed that if antibodies were used against other common EGFR ligands, such as EGF or TGF-α, there was no measurable deterioration of ERK phosphorylation, whereas an HB-EGF antibody substantially downgraded the signal. This begs the question why HB-EGF, and not one or all of the other ligands?

We believe that two major characteristics distinguish HB-EGF, namely its size and charge. For example, HB-EGF has a molecular weight of about 22kDa, whereas TGF-α and EGF are both only about 5.5kDa. In experiments performed in Spring's

laboratory (Kovbasnjuk et al., 2000), the diffusion coefficient in a similar LIS architecture decreased by an order of magnitude as the size of the molecule probed increased from 3kDa to 10kDa. Thus it is conceivable that just due to size alone HB-EGF would have a much smaller diffusion coefficient and would be "left behind" relative to the other ligands during the "washout" phase of a LIS collapse where fluid is squeezed out. Furthermore, HB-EGF is more likely to get trapped or hindered in the glycocalyx due to its positively charged domains (Raab and Klagsbrun, 1997) that could interact with negatively charged areas of the glycocalyx.

The end result would be a relatively higher increase in concentration of HB-EGF compared to other ligands in the collapsing LIS. In other words, the concentration of HB-EGF would increase drastically (while the concentration of other ligands would be mostly unchanged) and hence would provide a new input signal to the cell, initiating the mechanotransduction pathway. Further experimental evidence for such a mechanism comes from exogenously adding a bolus of HB-EGF and seeing a similar response in ERK phosphorylation as in the case of compressive stress (Tschumperlin et al., 2004). Therefore, since an increase in HB-EGF can cause the same cellular response as compressive stress, it is feasible that the collapsing LIS does just that: increases local HB-EGF concentration via the mechanism described above. In following chapters we explore these possibilities in more detail through the use of computer models.

1.7 Role of computer modeling

The established system of epithelial stress by pneumatic pressure was used to examine mechanotransduction in cultured human airway epithelial cells (Tschumperlin et al., 2004). However, the experiments performed can only provide a partial view of the system. To have a more complete and general understanding, mathematical and computer models are necessary. Specifically, not every quantity can be measured experimentally in real time, and even if such such measures were possible, one would still have to determine the relative importance of various ligand-receptor pairs in signal transduction. Computer models therefore become a valuable tool in this selection process and can also provide valuable insight that was not initially apparent. When coupled to experiments, these models allow for a more complete understanding of observed phenomena.

Once validated through experiments, computer models enable efficient exploration of a wide range of conditions. The models developed here are intimately related to experiments: the model input is the measured change in LIS geometry (due to compressive stress) and the output is the resulting change in extracellular ligand concentration. Different generations of the computer model presented in subsequent chapters reflect higher levels of complexity, all aimed at not only having a deeper understanding of the experimental results, but also elucidating the mechanisms involved in mechanotransduction of compressed airway epithelial cells.

1.8 Thesis organization

The thesis is organized as follows. The first generation model, based on one-dimensional dynamic diffusion is introduced in Chapter 2. Then, in the next chapter the previous model is expanded to include convection, thus providing a complete transport equation for extracellular ligand. In this second generation model, the geometric domain examined is extended into the sub-cellular space. Chapter 4 describes the measurement of EGFR-ligand shed into the LIS, both at a basal state and under pressure. Subsequent Chapters 5 and 6 deal with real-time imaging and quantification of the change in LIS geometry due to the application of pressure. Finally, in Chapter 7, the experimentally determined geometrical changes of the LIS are incorporated into both the 2-D and 3-D numerical models.

2. First generation model – dynamic diffusion

2.1 Introduction

In the previous chapter, we described a 1-D steady-state (i.e. time independent) model of LIS ligand concentration, developed by Tschumperlin and colleagues (Tschumperlin et al., 2004). This model yielded the parabolic concentration profiles (see Fig. 1.5) in the LIS for HB-EGF ligand for only two time points: first for the steady-state pre-collapse condition, and then, depending on the change in LIS width w, the final post-collapse steady-state. The implicit assumption was that after the collapse occurs, the LIS width stays constant and equal to the width at the end of the collapse.

The key result of the steady-state model was that the ligand concentration was inversely proportional to the LIS width. Thus, during a pressure-induced collapse the LIS width would decrease and the final, steady-state concentration would proportionally increase. This was an important first step in establishing the plausibility of the mechanotransduction mechanism via an increase in LIS concentration. However, the steady-state model could not address how the concentration changes during a collapse because all of the time-dependent terms were set to zero. Since ligand dynamics can dominate signal transduction (Sasagawa et al., 2005), we present in this chapter a dynamic diffusion model that outputs LIS ligand concentration as a function of both time and space. We then explore the parameter space of the model by varying the rate of width decrease, the diffusion coefficient, and the shedding rate of ligand into the LIS.

2.2 The dynamic diffusion equation

The steady-state model was based on removing the time-dependence from the concentration, effectively making the concentration a function of only the spatial coordinate x. Hence the basic diffusion equation becomes

$$\frac{\partial C}{\partial t} = 0 = D\frac{\partial^2 C}{\partial x^2} + \frac{2q}{w} \tag{1}$$

where C is the ligand (HB-EGF) concentration, x is the apico-basal direction, D is the diffusion coefficient of ligand through the LIS/glycocalyx matrix, q is the rate of shedding of ligand from the cell surface into the LIS and w is the LIS width. Solving equation (1), the steady-state concentration profile becomes

$$C(x) = \frac{q}{wD}(h^2 - x^2) \tag{2}$$

Here h is the total apical-basal height of the LIS. From this equation we see how for a given w we can obtain a steady-state concentration profile. Clearly, a smaller width results in a greater concentration.

Although this was an important initial step in linking geometric changes of the LIS to extracellular ligand concentration, many important issues could not be addressed from this simple model. One such issue is the time-dependence of changes in ligand concentration as the LIS collapses. In other words, the key question becomes: how does the LIS ligand concentration change over time during and after the collapse?

To answer this question we needed to employ numerical methods to solve the diffusion equation in which C and w are considered to be a function of time:

$$\frac{\partial C(x,t)}{\partial t} = D\frac{\partial^2 C}{\partial x^2} + \frac{2q}{w(t)} \tag{3}$$

2.3 Finite element model of dynamic diffusion

In order to solve equation (3) we first discretize the LIS space into 1-D finite elements (see Figure 2.1). Then, using the Galerkin weighted method (Huebner, 1975) we transform equation (3) into the following form:

$$\int_L \psi(x)\left[\frac{\partial C}{\partial t}+\frac{\partial}{\partial x}\left(D\frac{\partial C}{\partial x}\right)+q_V=0\right]dL \qquad (4)$$

where $\psi(x)$ is a weighted function, $q_V=\frac{2q}{w}$ is the source term due to the shedding, and L is the selected domain. Equation (4) represents the so-called *weak form* (Bathe, 1996; Hughes, 1987) of the differential equation (3) since the equation (3) is not necessarily satisfied at each point of the domain.

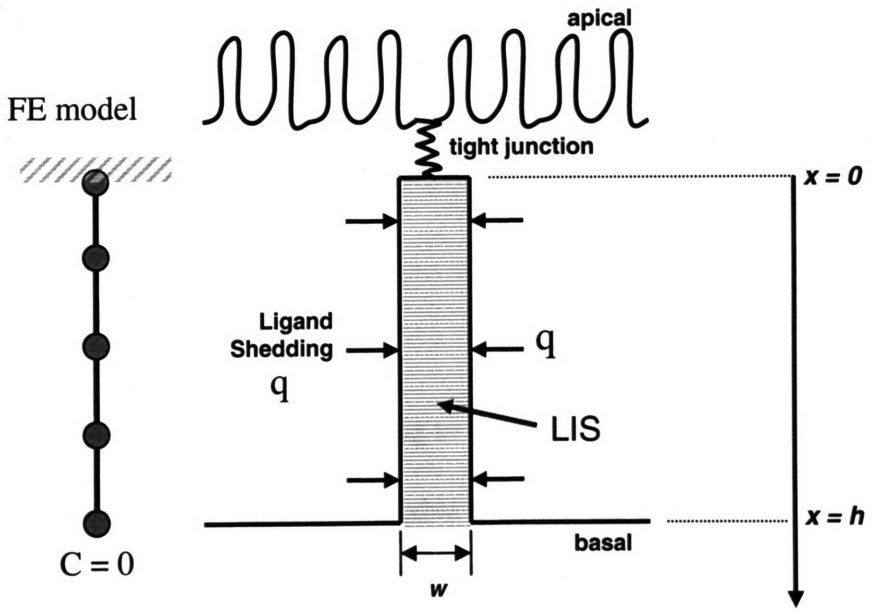

Figure 2.1 Schematic of the 1-D LIS finite element (FE) model. At the apical surface of the LIS (x=0) there is an impermeable wall (tight junction) and at the basal surface (x=h) we assume the ligand concentration is zero. Each finite element consists of two nodes (depicted as circles); note: FE model not drawn to scale.

In the isoparametric formulation of a 1-D finite element of the length L we use interpolation functions N_K as the weighted functions (where the subscript K refers to the node number) (Huebner, 1975). The nodes of the finite elements are represented with circles in Fig. 2.1. Therefore, we obtain N weak-form equations for a finite element,

$$\int_L N_K \left[-\frac{\partial C}{\partial t} + \frac{\partial}{\partial x}\left(D\frac{\partial C}{\partial x} \right) + q_V = 0 \right] dL \qquad K = 1,2,...,N \tag{5}$$

where N is the number of nodes per element. In our case there are two nodes per element, thus K=1,2. Applying Gauss' theorem to the diffusion term within the integral we obtain

$$\int N_K \frac{\partial}{\partial x}\left(D\frac{\partial C}{\partial x} \right) dL = \int_S N_K D\frac{\partial C}{\partial x} dS - \int_L D\frac{\partial N_K}{\partial x}\frac{\partial C}{\partial x} dL \tag{6}$$

where S is the element surface and the term $D\dfrac{\partial C}{\partial x}$ represents the flux q_s of C through the element surface, which in our case are the two cross-sectional areas (one at each of the element nodes and equal to $w \times (unit\ depth)$). The surface integral can then be written as

$$Q_K^S = \int_S N_K D\frac{\partial C}{\partial x} dS = \int_S N_K\, q_s\, dS \tag{7}$$

where $Q_K^S(t)$ is the surface flux corresponding to the node 'K'.

Next we perform the interpolation of the variable C within the element as

$$C = N_K C^K = N_1 C^1 + N_2 C^2 + ... + N_N C^N \tag{8}$$

where C^K are the nodal values of C. Now, we substitute equations (6) and (8) into (5) and also use (7), to obtain

$$\mathbf{M}\dot{\mathbf{C}} + \mathbf{K}\mathbf{C}^{\mathbf{K}} = \mathbf{Q}^{\mathbf{S}} + \mathbf{Q}^{\mathbf{V}} \ , \quad \text{or} \quad M_{KJ}\dot{C}^{J} + K_{KJ}C^{J} = Q_K^S + Q_K^V, \quad K, J = 1,2,...,N \qquad (9)$$

Here $\mathbf{C}$ is the vector of nodal values C^K, $\dot{\mathbf{C}}$ is the vector of time derivatives at nodal points, and the matrices and vectors are:

$$M_{KJ} = \int_L N_K N_J \, dL \, , \; K_{KJ} = \int_L D \frac{\partial N_K}{\partial x} \frac{\partial N_J}{\partial x} dL \, , \; Q_K^S = \int_S N_K q_S dS \, , \; Q_K^V = \int_S N_K q_V dS \qquad (10)$$

The system of equations (9) represents the equations of balance for a finite element. Assemblage of the element equations is then performed and appropriate boundary conditions must be implemented prior to solving the equations of the whole system. The equation of balance for the finite element assemblage retains the form of equation (9). Note that the surface fluxes Q_K^S cancel over the internal surfaces of the finite elements, i.e. the flux leaving one node of the finite element is equal to the flux going into the same node of the neighboring finite element which shares that node. Therefore, the contribution to the system surface vector $\mathbf{Q}^S$ comes only from the flux through the surface of the whole domain.

The incremental form for time integration of equation 9 can be written as

$$\left(\frac{1}{\Delta t}\mathbf{M} + \mathbf{K}\right) {}^{n+1}\mathbf{C} = {}^{n+1}\mathbf{Q}^{\mathbf{S}} + {}^{n+1}\mathbf{Q}^{\mathbf{V}} - \frac{1}{\Delta t}\mathbf{M} \, {}^{n}\mathbf{C} \qquad (11)$$

where Δt is the time step, and the upper left indices n and $n+1$ denote values at the start and end of the n-th time step (Kojic and Bathe, 2005).

2.4 Exploring the parameter space of the diffusion equation

Based on the diffusion equation (3), the ligand concentration C depends on three parameters: the diffusion coefficient D, the shedding rate q, and the LIS width w. To investigate the effect of these parameters on the changes in concentration we employed

our finite element (FE) model to see the interdependence of the three parameters and thus get a sense of the relative importance of experimentally determining each/all of them.

The LIS geometry was regarded as a 1-D rod (see Fig. 2.1), consisting of 50 finite elements. The boundary conditions were: no flux through the top, apical surface; and zero-concentration at the bottom, basal surface (see Fig. 2.1). The diffusion equation (3) was then transformed to the appropriate 1-D finite element form (see equation (11)) and solved using the PAK software package (Kojic et al., 1997). We define x as the depth coordinate, being 0 at the most apical (tight junction) surface (see Fig. 2.1).

To explore the effect on concentration, the parameters D, w, and q were changed. We first assume constant D and q, while the width w changes. We further assume that the LIS width w decreases linearly during the prescribed time of collapse. For example, in previous work (Tschumperlin et al., 2004) it was established that the LIS width shrinks to close to 90% in a time that is less than 20 minutes. Exactly how fast the LIS shrinks was unclear since the imaging technique only allowed measurements at 20 minute intervals. Thus, we first solved the ligand concentration profiles for a very rapid (1 second) LIS collapse from w=2 to 0.6 microns (see Fig. 2.2). The diffusion coefficient was taken from the literature and estimated to be 18 $\mu m^2/s$ (Kovbasnjuk et al., 2000), whereas the shedding rate was roughly approximated to be 12.6 (ng.μm)/(mL.s) (based on personal communication with Dr. Ivan Maly, unpublished results). The height h of the LIS was taken from previous experiments (Tschumperlin et al., 2004) to be h=17μm. The open red circles (see Fig. 2.2) represent the analytical solution (see equations 1 & 2) for w=2 μm, which is in agreement with our numerical solution. The curves to the right of initial t=0 curve, represent the time evolution of concentration increase as the LIS collapses

from w=2 to 0.6 μm in 1 second. The curve at t =50s is the new steady-state concentration profile corresponding to w=0.6 μm.

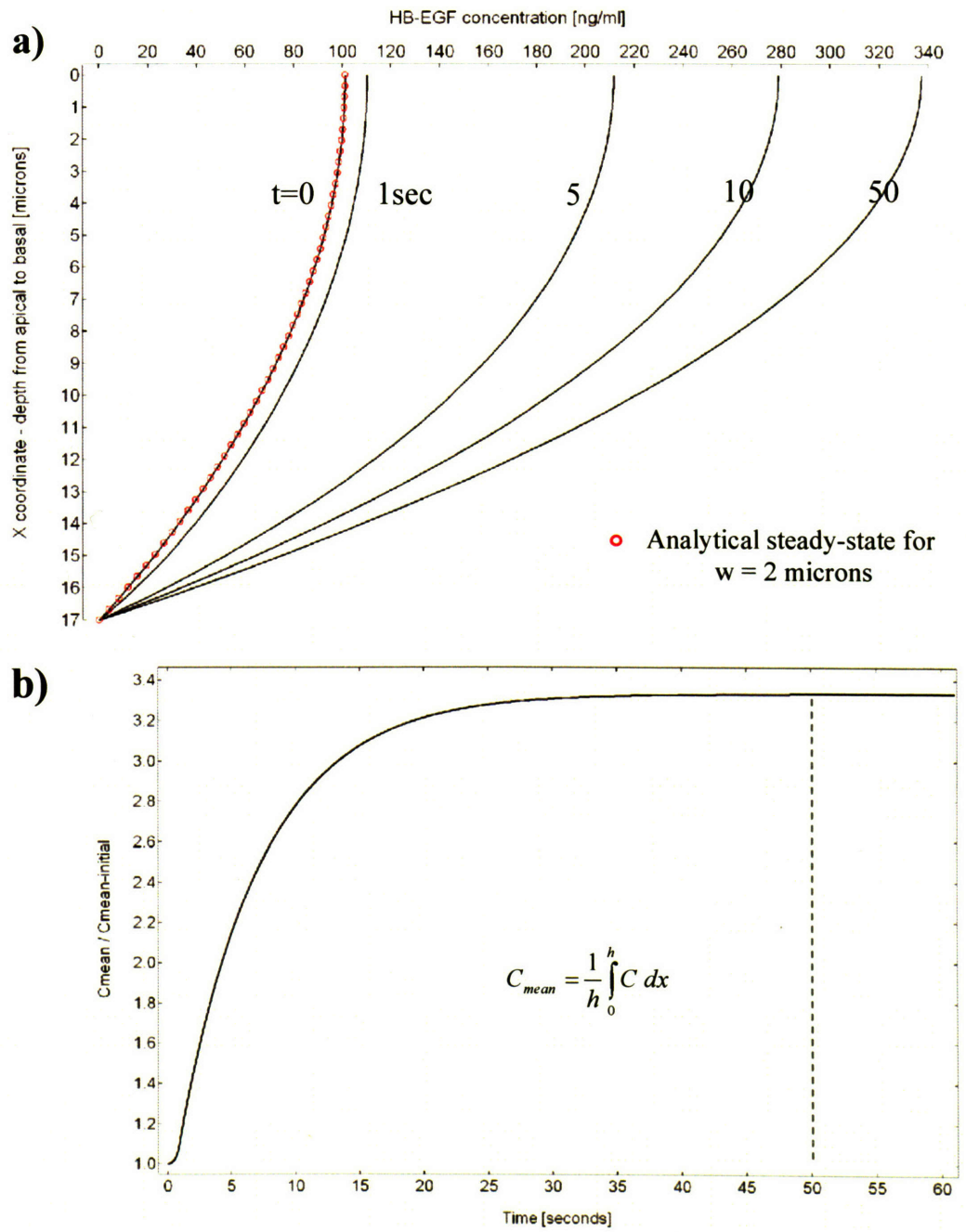

Figure 2.2 Case for w = 2 → 0.6 μm in 1 second, D =18 μm^2/s, q =12.6 (ng.μm)/(mL.s)

a) Numerical solution for concentration profiles along the LIS depth
b) Corresponding fold increase in mean LIS concentration

In addition to looking at the concentration profile along the depth of the LIS it is worthwhile to examine the relative fold increase of the mean LIS concentration defined as:

$$C_{mean} = \frac{1}{h}\int_0^h C\,dx \tag{12}$$

The ratio of *Cmean* over the initial *Cmean*, i.e. the fold increase in mean LIS ligand concentration, for the same conditions of LIS collapse as described above, indicates an initial rapid increase followed by a steady-state plateau (see Fig. 2.2b).

Previously we have stated that we observed a change in LIS volume of about 90% in <20min and we show the effects of a rapid 1second collapse in Fig. 2.2. Next we show how the LIS concentration dynamics change when the time of collapse increases. Specifically, we examine 4 cases: $t_{collapse}$=1, 100, 500, 1000 seconds, and assume that LIS width changes from w = 2 to 0.2 μm during the prescribed time of collapse, with all other parameters being the same as above in Fig. 2.2. The results for these 4 cases are shown in Fig. 2.3. As the figure indicates, the varying time-of-collapse has a profound effect on the dynamics, where the longer $t_{collapse}$ results in a slower approach to steady-state.

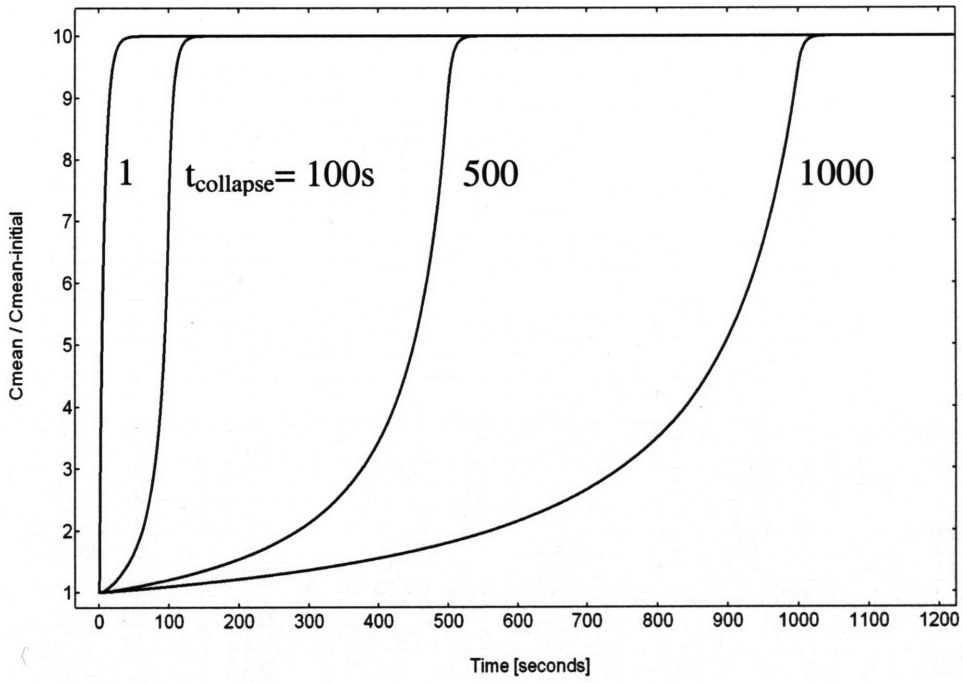

Figure 2.3 Variable $t_{collapse}$ (number next to each curve indicates duration of collapse) for $w = 2 \rightarrow 0.2\mu m$, $D = 18\ \mu m^2/s$, $q = 12.6$ (ng.μm)/(mL.s)

In all of the above calculations, both the diffusion coefficient and the shedding rate were assumed to be constant during and after the LIS collapse. We next explore what are the effects of variable diffusion coefficient D on the diffusion process in the LIS. Namely, it is likely that the ligand diffusion coefficient through the LIS can change as a result of structural changes in the LIS glycocalyx. In effect, the glycocalyx matrix becomes "denser" and further hinders diffusion of a large molecule like HB-EGF (molecular weight of 22kDa) (Kovbasnjuk et al., 2000; Xia et al., 1998). To see how a changing diffusion coefficient affects the mean concentration, we assume that the diffusion coefficient D decreases linearly with LIS collapse. In other words, D is a linear function of w: D=18 $\mu m^2/s$ for w=2 μm and D=1.8 $\mu m^2/s$ for w=0.2 μm. The results are

displayed in Fig. 2.4. For comparison, we also plot the previously determined case of constant D =18 $\mu m^2/s$ (broken blue line). The decreasing diffusion coefficient has a retarding effect on the concentration increase toward the new steady-state for each of the four $t_{collapse}$ cases.

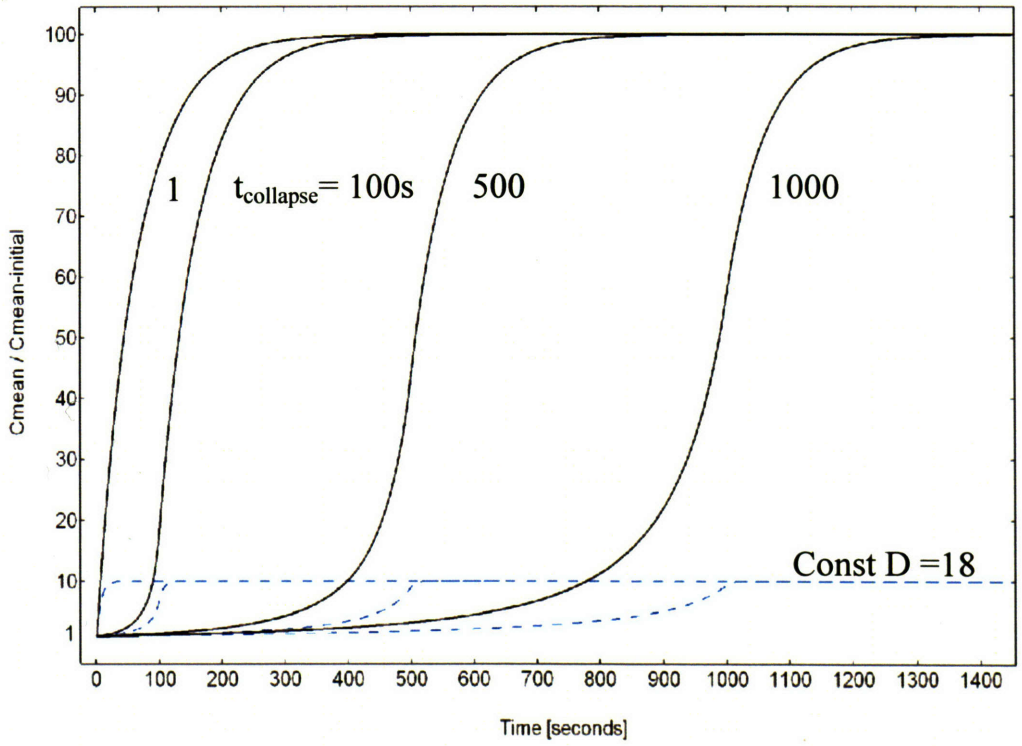

Figure 2.4 Variable diffusion coefficient and variable $t_{collapse}$ for:

$w = 2 \rightarrow 0.2\mu m$, $D = 18 \rightarrow 1.8\ \mu m^2/s$, q =12.6 (ng.μm)/(mL.s)

Broken blue line represents Fig. 2.3, with constant D=18 $\mu m^2/s$.

The third, final parameter that could be variable (and was until now assumed constant) is the shedding rate q. It is conceivable that the LIS autocrine loop involving the EGFR-ERK-metalloprotease mechanism (see Fig. 1.2) could change due to increased ligand binding to the EGFR. We examine two cases of changing q: one being a linear

and sustained 5-fold increase (broken blue line in Fig. 2.5); and the other being a transient 5-fold increase followed by a symmetric, linear decrease to the initial value of q (solid line in Fig. 2.5). For clarity, we only consider one time of collapse: $t_{collapse}$=1second. The resulting concentration curves differ in shape and character, prompting the need to further investigate and experimentally determine not only how q might change, but also how all of the parameters in the diffusion equation behave in the *in vitro* pressure system.

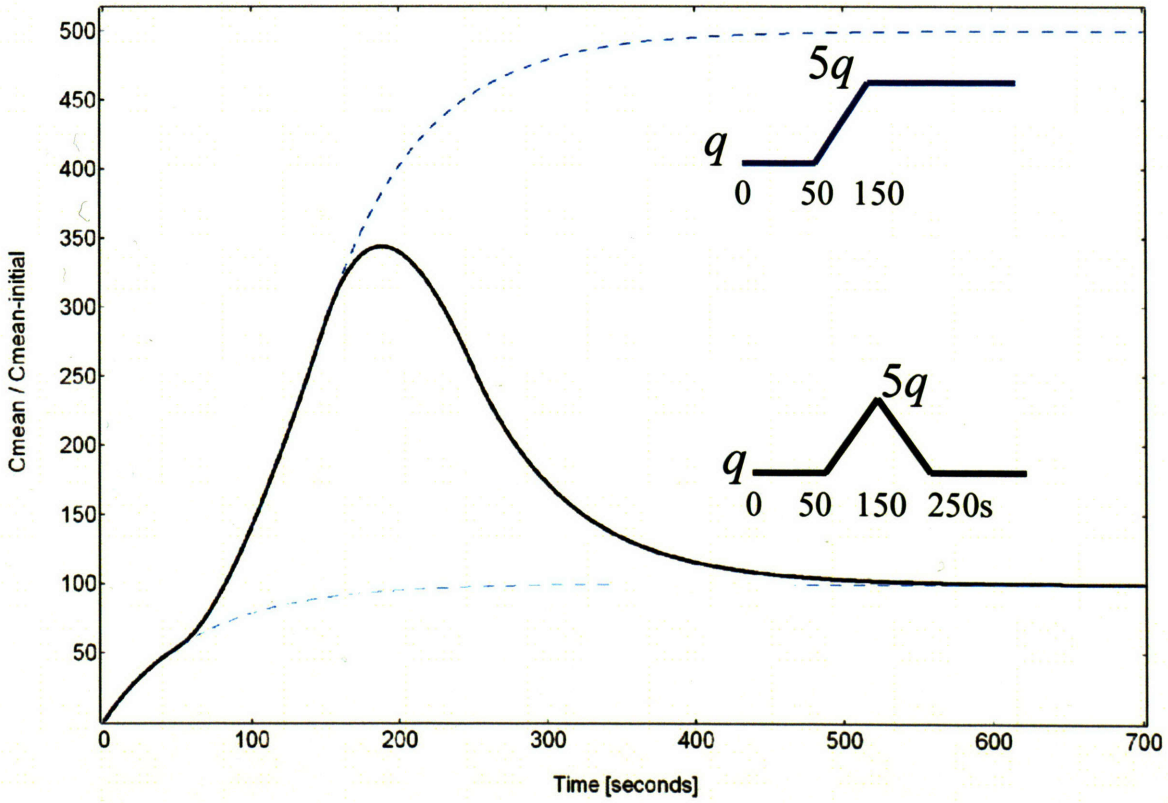

Figure 2.5 Variable q, w, D: w =2 → 0.2 μm in 1 second, D =18 → 1.8 μm^2/s.

Top broken line: change in q =12.6 → 63(ng.μm)/(mL.s) during 50→150s.

Solid line: q =12.6 → 63 during 50→150s followed by q =63 → 12.6 during 150→250s.

Bottom broken line represents Fig. 2.2b) where q=const=12.6(ng.μm)/(mL.s).

The modeling results presented in this chapter were based on dynamic diffusion and hence yielded LIS ligand concentrations as a function of time and space. By varying parameters in the diffusion equation we were able to gain insight into ligand dynamics for a range of conditions (e.g. fast vs. slow change in LIS geometry). The dynamic diffusion model was built upon the steady-state model and represented an important step forward in understanding how LIS collapse affects ligand concentration. However, the effect of convection, i.e. fluid flow, was completely neglected. The assumption of a purely diffusive process meant that the fluid squeezed out of the LIS did not carry any concentration with it (or it carried such a small amount that it was negligible). Such an assumption may not be valid, especially for a rapid collapse, where most of the fluid in LIS flows into the underlying reservoir in a short period of time. Another issue that the pure-diffusion model could not address was what happens in the underlying reservoir close to the LIS boundary. To adequately examine these and other convection-related issues, we had to develop a more complete transport model, which coupled diffusion and convection, and also included the underlying media reservoir. We present this diffusion-convection model next.

3. Second generation model – dynamic diffusion & convection

3.1 Introduction

In the previous chapter we examined dynamic diffusion in the lateral intercellular space of two neighboring airway epithelial cells. The model presented in Chapter 2 was a continuation of previous work, which established only the steady-state LIS ligand concentration profiles. Furthermore, the dynamic diffusion model was based on pure diffusion and neglected potentially important effects of convection.

In this chapter we develop a generalized finite-element solution of the coupled 1-D diffusion-convection equation to evaluate the temporal changes in ligand concentration occurring in a dynamically collapsing interstitial space between epithelial cells (Kojic et al., 2006). We introduce a new geometry for the model that accommodates diffusion and convection of ligands that are shed into a lateral intercellular space that is continuous with an underlying media reservoir (Kojic et al., 2006). Employing the model, we explore the parameter space of the governing equations, examining the effect of ligand diffusivity, shedding rate, and rate of extracellular space change on the kinetics of ligand accumulation. The new model geometry reveals the transient effect of convection on ligand concentration changes in the underlying space (e.g media for the *in vitro* case or tissues *in vivo*), suggesting a potential mechanism for communication of a change in the mechanical state of the epithelium to underlying tissues. Moreover, the diffusion-convection model offers a novel explanation for how cells could discriminate between mechanical processes occurring over a range of rates in different physiological scenarios. We use insights gained from the model to propose two explanations for a selective contribution of the EGF family-ligand heparin-binding EGF (HB-EGF) to the

transduction of mechanical stress via autocrine signaling in a collapsing extracellular space.

3.2 Finite element model of coupled diffusion and convection

We modeled the lateral intercellular space (LIS) separating neighboring cells as idealized parallel plates and assumed free diffusion of ligand into the media reservoir below the LIS. Boundary conditions to represent the special case of an epithelial layer were imposed: impermeable tight junction at the apical surface; open to a large reservoir (e.g. the underlying media) such that sufficiently far below the basal surface the ligand concentration is assumed to be zero (see Fig. 3.1). Previously we solved the 1-D diffusion equation (Fick's Law) analytically, with a source term included to account for the constitutive shedding of ligand into the LIS, to obtain the steady-state ligand concentration profile within the LIS:

$$\frac{\partial C}{\partial t} = D_{LIS}\frac{\partial^2 C}{\partial x^2} + \frac{2q}{w} \tag{1}$$

Here the ligand shedding rate q (distributed uniformly along the lateral cell boundary) and ligand diffusion coefficient in the LIS D_{LIS} are assumed to be constants, and w is the LIS width. Solving for the steady-state ligand concentration $C(x)$ yields:

$$C(x) = C_h + \frac{q}{wD}\left(h^2 - x^2\right) \tag{2}$$

where C_h is the ligand concentration at the LIS boundary $x=h$.

To account for convective effects, as well as to determine how the concentration at and below the LIS boundary changes during a collapse, we now introduce an extended model geometry with three domains: LIS, transitional, and radial (see Fig. 3.1). The LIS domain includes the LIS space, from the tight junction to the basal boundary. The transitional domain corresponds to the space between LIS and radial domains, where we numerically switch from a cartesian to a cylindrical coordinate system. The radial domain represents the outside space (i.e. underlying media or tissues) and allows for radial diffusion of ligand once it leaves the LIS. The governing transport equations for each domain are

LIS: $$\frac{\partial C}{\partial t} = D_{LIS}\frac{\partial^2 C}{\partial x^2} + \frac{2q}{w} - V_x\frac{\partial C}{\partial x} \tag{3a}$$

Transitional: $$\frac{\partial C}{\partial t} = D_{out}\frac{\partial^2 C}{\partial x^2} - V_t\frac{\partial C}{\partial x} \tag{3b}$$

Radial: $$\frac{\partial C}{\partial t} = D_{out}\frac{\partial^2 C}{\partial r^2} + D_{out}\frac{1}{r}\frac{\partial C}{\partial r} - V_r\frac{\partial C}{\partial r} \tag{3c}$$

where D_{LIS} and D_{out} are the ligand diffusivities in the LIS and outside space, respectively, V_x is the bulk fluid velocity in the LIS caused by changes in LIS dimensions, V_t is the fluid velocity in the transitional domain (assumed to be uniform), and V_r is the radial fluid velocity at a radius r measured from the LIS boundary. Notice that in equations (3b,c) there is no q (ligand shedding) term because shedding is assumed to occur only from the lateral surfaces of the LIS.

By conservation of mass and fluid incompressibility it can be shown that in the LIS:

$$V_x = \frac{\dot{w}}{w}x \tag{4a}$$

where $\dot{w} = dw/dt$ is the rate of change of LIS width, while in the radial domain:

$$V_r \pi r = const. \tag{4b}$$

The transitional regime was included to avoid numerical difficulties that can occur when switching form cartesian to cylindrical coordinate systems. The transitional region begins at the LIS boundary and extends to a distance $R_t = w/\pi$ below the LIS. This distance was determined by matching the fluxes corresponding to cartesian (w) and radial (πR_t) lengths, through which the flux passes. We further approximate the velocity field in this domain as uniform, being equal to the bulk velocity at the LIS exit $V_t = V_x(x = h)$. The approximations made in this domain have little impact on the overall concentration profile inside and outside of the LIS.

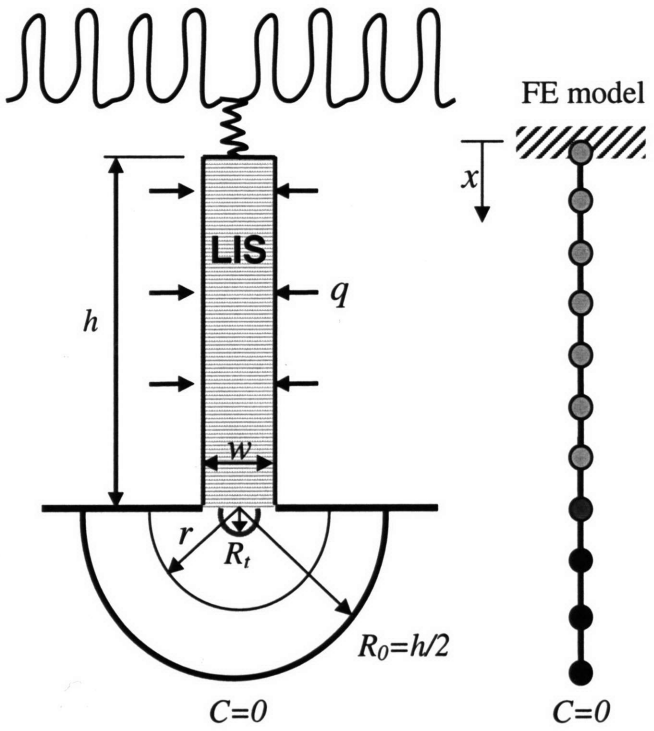

$$\frac{\partial C}{\partial t} = D_{LIS}\frac{\partial^2 C}{\partial x^2} + \frac{2q}{w} - V_x\frac{\partial C}{\partial x}$$

$$\frac{\partial C}{\partial t} = D_{out}\frac{\partial^2 C}{\partial x^2} - V_t\frac{\partial C}{\partial x}$$

$$\frac{\partial C}{\partial t} = D_{out}\frac{\partial^2 C}{\partial r^2} + D_{out}\frac{1}{r}\frac{\partial C}{\partial r} - V_r\frac{\partial C}{\partial r}$$

Figure 3.1 Schematic of LIS finite element (FE) model. Neighboring cells are separated by the LIS. Ligands are constitutively shed into LIS from the cell surface at a rate q. In the space below the LIS it is assumed that at a radial distance $R_0=h/2$ (where h is the LIS height) the ligand concentration is zero. The second boundary condition is an impermeable wall at the top due to the tight junctions (no flux at x=0). Using 1-D isoparametric finite elements we discretize the space into three domains: LIS (for $0< x <h$), transitional (for $h< x <h+R_t$) and radial (for $R_t< r <R_0$). Note that the finite elements are not to scale. Each of the domains has its own governing diffusion-convection equation. In the three domains the corresponding bulk fluid velocities are V_x in the LIS, V_t in the transitional, and V_r in the radial domain. The diffusivities D_{LIS} and D_{out} (inside and outside the LIS, respectively) may be different. The transitional domain extends $R_t = w/\pi$ below the LIS.

The radial domain encompasses the region between R_t (end of the transitional domain) and $R_0 = h/2$ (where we assume the ligand concentration to be zero). Mathematically, the zero-concentration boundary would be infinitely far away from the LIS (i.e. $R_0 \rightarrow \infty$), but for efficient numerical simulations we determined that for a LIS height h=15 microns (Tschumperlin et al., 2004), $R_0 = 7.5\mu m$ is sufficiently far away from the LIS boundary such that further increasing R_0 had little effect on the overall concentration profile (data not shown). Hence, for all of the simulations we fixed the value of $R_0 = 7.5\mu m$ to be half of the previously measured LIS height h=15 microns (Tschumperlin et al., 2004).

The diffusion-convection equations, along with the boundary conditions of no flux at the most apical point (impermeable tight junction) and zero concentration at R_0, were solved using the PAK finite element method software package (Kojic et al., 1997). The LIS and outside space were discretized by 1-D isoparametric finite elements (see Fig. 3.1). The governing differential equations 3a-c were first converted to the appropriate finite element system of first-order nonlinear differential equations, which were further linearized and integrated in time using a time-step Δt. A Newton-Raphson iterative scheme was employed for each time-step Δt (Kojic and Bathe, 2005) . The final system of incremental-iterative equilibrium equations for a time step is

$$\hat{\mathbf{K}}\,\Delta\mathbf{C}^{(i)} = {}^{t+\Delta t}\mathbf{Q}^{(i-1)} - {}^{t+\Delta t}\mathbf{F}^{(i-1)} \qquad (5)$$

where $\Delta\mathbf{C}$ is the vector of concentration increments at the finite element nodal points, $\hat{\mathbf{K}}$ is the system matrix, $\mathbf{Q}$ is the convection and shedding vector, and $\mathbf{F}$ is the out-of-balance vector; the left superscript $t+\Delta t$ shows that matrices and vectors were evaluated

at the end of the time step, while the right superscript indicates the equilibrium iteration counter. In component form, the terms of equation (5) are

$$\hat{K}_{KS} = M_{KS} + K_{KS} = \frac{1}{\Delta t}\int_L N_K N_S dx + \int_L D\frac{\partial N_K}{\partial x}\frac{\partial N_S}{\partial x}dx \tag{6a}$$

$${}^{t+\Delta t}Q_K^{(i=1)} = Q_K^V + Q_K^{Vel} = \int_L N_K \frac{2q}{w}dx - \int_L N_K\, {}^{t+\Delta t}V\frac{\partial {}^{t+\Delta t}C^{(i-1)}}{\partial x}dx \tag{6b}$$

$${}^{t+\Delta t}F_K^{(i-1)} = K_{KS}\, {}^{t+\Delta t}C_S^{(i-1)} - \frac{1}{\Delta t}M_{KS}({}^{t+\Delta t}C_S^{(i-1)} - {}^{t}C_S) \tag{6c}$$

where N_K are interpolation functions (see Chapter 2), L is the length of the finite element, C_S is concentration at node S of the finite element, while V and C are the velocity and concentration within the finite element.

In the radial domain below the LIS axially symmetric 1-D finite elements were used. From the equation of balance in cylindrical coordinates (see equation 3c) and integration over *rdr* instead of *dx* we obtain the finite element equations for the axially symmetric 1-D elements in the form of equation 6.

A time series of the concentration profiles $C(x,t)$ during a linear decrease in w by 85%, from 1.5 to 0.225 μm (based on previous experimental results (Tschumperlin et al., 2004)) over a 60 second duration is shown in Fig. 3.2a. The open circles correspond to the analytical, pre- and post-collapse steady-state solutions (see equation (2)). Each of the solid-line curves represents a solution of equations (3a-c) at different time points. The height of the LIS was chosen to be 15 μm and the LIS width w to be initially 1.5 μm (Tschumperlin et al., 2004) (thus the outside space extended to $R_0=h/2=5w_0=7.5\mu m$ below the LIS). For this example the ligand diffusivity and shedding rate were arbitrarily selected ($D_{LIS}=D_{out}=75\ \mu m^2/s$ and q=10 molecules/cell/minute).

a)

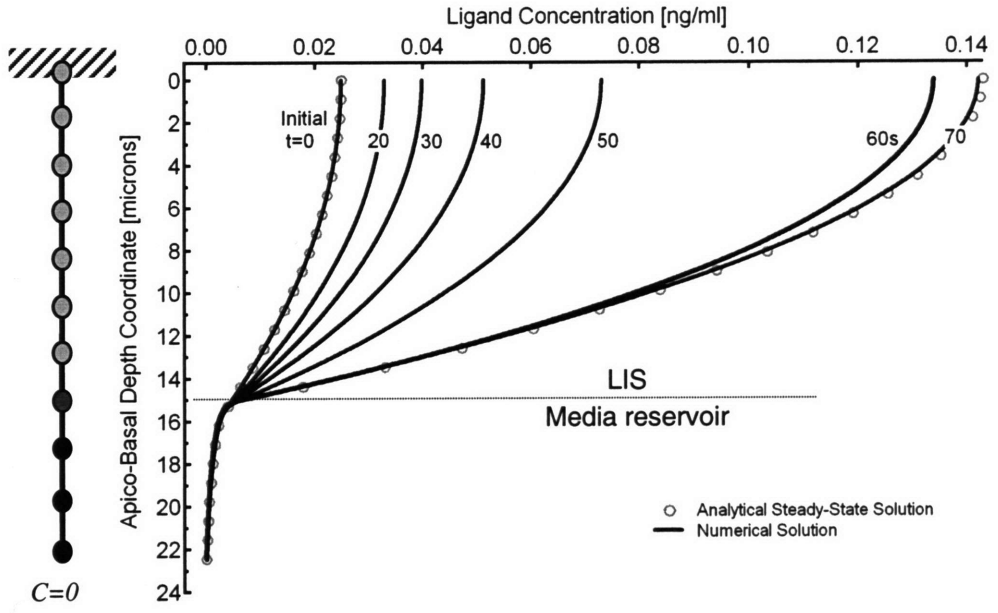

b)

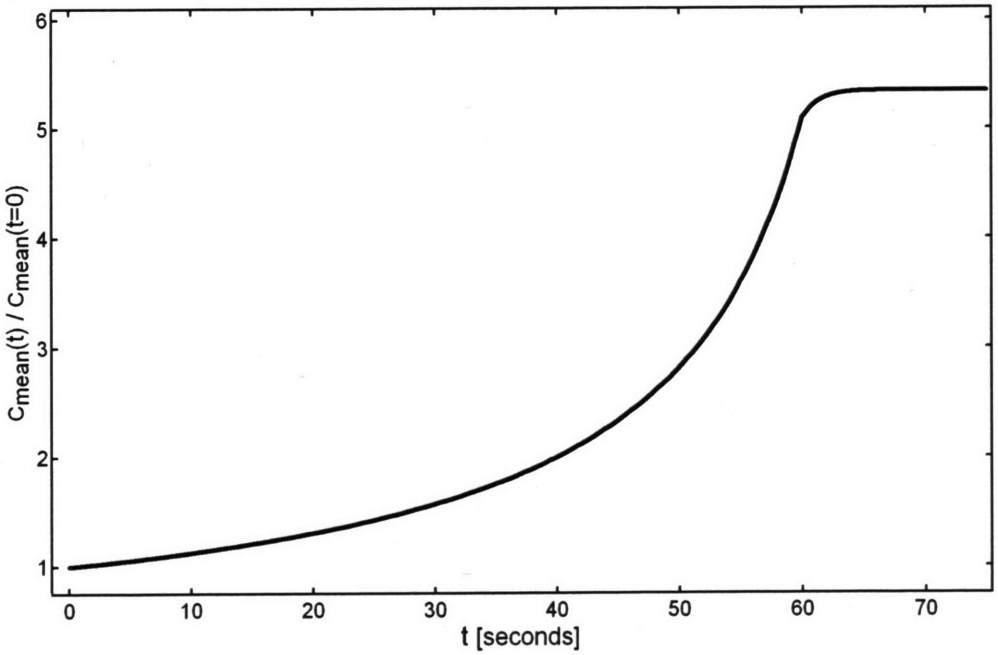

Figure 3.2 Solutions obtained by solving for the ligand concentration from the governing diffusion-convection equations. **a)** Evolution of the time-dependent concentration profile

during a LIS collapse to 15% of its original width (from 1.5 to 0.225 μm) over 60 sec. Concentration is plotted vs. the apico-basal depth coordinate, where x=0 at the apical tight junction, x=15 at the LIS boundary, and at a depth of 22.5 μm the concentration is zero. The corresponding finite element model is shown on the left. For comparison the open circles represent the analytical steady-state solution prior to LIS collapse and upon reaching the new, post-collapse steady-state. The numbers next to the curves indicate seconds after onset of collapse. **b)** Concentration profiles from **a)** plotted as fold-mean-concentrations: $C_{mean}(t)/C_{mean}(t=0)$. Here, $C_{mean}(t) = \frac{1}{h}\int_0^h C(x,t)\,dx$, where h is the LIS depth equal to 15 μm, and $C_{mean}(t=0)$ is the mean LIS ligand concentration just prior to the change in LIS width.

Another way to represent the same time series of ligand concentration profiles is to calculate the fold change in the mean ligand concentration: $C_{mean}(t)/C_{mean}(t=0)$ (Fig. 3.2b). Here, $C_{mean}(t) = \frac{1}{h}\int_0^h C(x,t)\,dx$ and $C_{mean}(t=0)$ is the mean LIS ligand concentration just prior to the change in LIS width.

3.3 Exploring the parameter space of the governing equations

Cells express a variety of autocrine mediators with a range of diffusivities dependent on molecular size and charge characteristics (Kovbasnjuk et al., 2000; Xia et al., 1998). These mediators are likely released at various rates, further influencing their kinetics within the LIS. We therefore explored the parameter space of the governing equations to

characterize the relative importance of ligand properties by varying the diffusion coefficient D and the shedding rate q over several orders of magnitude. In all these simulations, the LIS width was decreased to 15% of its initial, pre-collapse value (from 1.5 to 0.225 μm) linearly over 60 seconds. The magnitude of this change was selected to correspond to previous experimental results in bronchial epithelial cells compressed by an apical to basal pressure gradient of 30cmH_2O (Tschumperlin et al., 2004). The rate of LIS width change was arbitrarily selected; we address the importance of this parameter later.

The diffusion-convection Eqs. 3a-c were first solved for a constant q of 10 molecules per cell per minute (DeWitt et al., 2001) (evenly distributed along the cell boundary), with diffusion coefficients of 100, 10, 1, and 0.1 $\mu m^2/s$ (Fig. 3.3). Diffusivities on the order of 100 $\mu m^2/s$ characterize free diffusion of smaller molecules whose molecular weight ranges from about 0.1-10kDa, whereas D on the order of $10\mu m^2/s$ corresponds to free diffusion of larger molecules 10-1000kDa. The cases of D = 0.1 and $1\mu m^2/s$ represent hindered diffusion of large molecules (Kovbasnjuk et al., 2000). We further assumed equal diffusivities inside and outside of the LIS, $D_{LIS} = D_{out}$ (this assumption will be addressed later). The results of these simulations are plotted alongside each other in Fig. 3.3. The case of D = 0.1 $\mu m^2/s$ is shown in the inset due to the difference in the time scale. In general, the smaller the ligand diffusivity (or conversely the larger the ligand), the slower the increase in the normalized mean concentration during LIS width change.

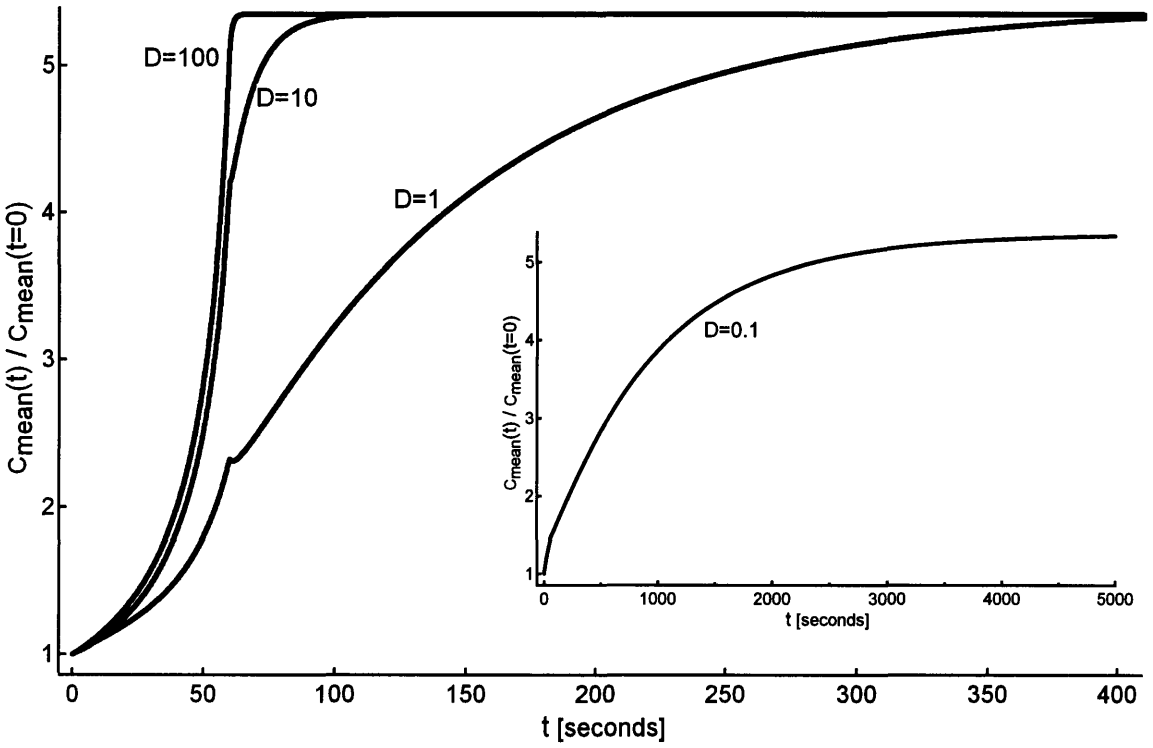

Figure 3.3 Effect of diffusion coefficient on concentration. A 60s collapse was examined for cases of D=0.1, 1, 10, 100 $\mu m^2/s$, where the LIS width decreases linearly to 15% of its original value (from 1.5 to 0.225 μm) over a 60 second interval. Diffusion coefficient units are $\mu m^2/s$. Inset is for the case of D=0.1 $\mu m^2/s$ (time scale goes to 5000s). All cases assume a constant shedding rate of q = 10 molecules/cell/min.

A similar order-of-magnitude analysis was performed for shedding rates from 0.1 to 1000 molecules/cell/min (DeWitt et al., 2001) (data not shown). While the shedding rate affected the absolute value of ligand concentration, it did not alter the normalized fold change in concentration induced by LIS collapse; this was true both at steady state and during the dynamic changes in LIS dimensions. Hence, the influence of shedding rate was limited to effects on the absolute ligand concentrations in our system.

3.4 Estimating the HB-EGF diffusion coefficient in the LIS

In the LIS of MDCK epithelial cells, which share a generally similar architecture with human bronchial epithelial cells, large molecules experience hindered diffusion due to the protrusion of a glycocalyx into the LIS (Kovbasnjuk et al., 2000). Specifically, while a 3kDa molecule diffuses in the LIS of MDCK cells as if in free solution, a significant decrease in diffusion coefficient is observed for a 10kDa molecule relative to that for free diffusion (Fig. 3.4). Because our previous work in human bronchial epithelial cells suggested a key role for HB-EGF in mechanotransduction (Tschumperlin et al., 2004; Tschumperlin et al., 2002), we used these existing diffusion data to estimate the diffusivity of HB-EGF in a typical LIS. HB-EGF that is proteolytically processed and shed into the LIS has a molecular weight of about 22kDa (Harris et al., 2003; Raab and Klagsbrun, 1997) and is heavily charged (Raab and Klagsbrun, 1997). Previous studies have shown that interactions between a charged molecule and the extracellular glycocalyx can hinder diffusion (Dowd et al., 1999). Therefore, we assumed that HB-EGF diffusion in the LIS would be significantly hindered, due to both charge interactions and given that this effect is readily apparent for a smaller 10kDa molecule (Kovbasnjuk et al., 2000) (Fig. 3.4). Based on these data we approximated the HB-EGF diffusion coefficient in the LIS as $D_{LIS} = 1.8\mu m^2/s$, while outside the LIS it was assumed to be an unhindered (free solution) value of $D_{out} = 75\mu m^2/s$. The choice of the hindered LIS diffusion coefficient is only an order-of-magnitude estimate based on hindered diffusion of large molecules in the LIS.

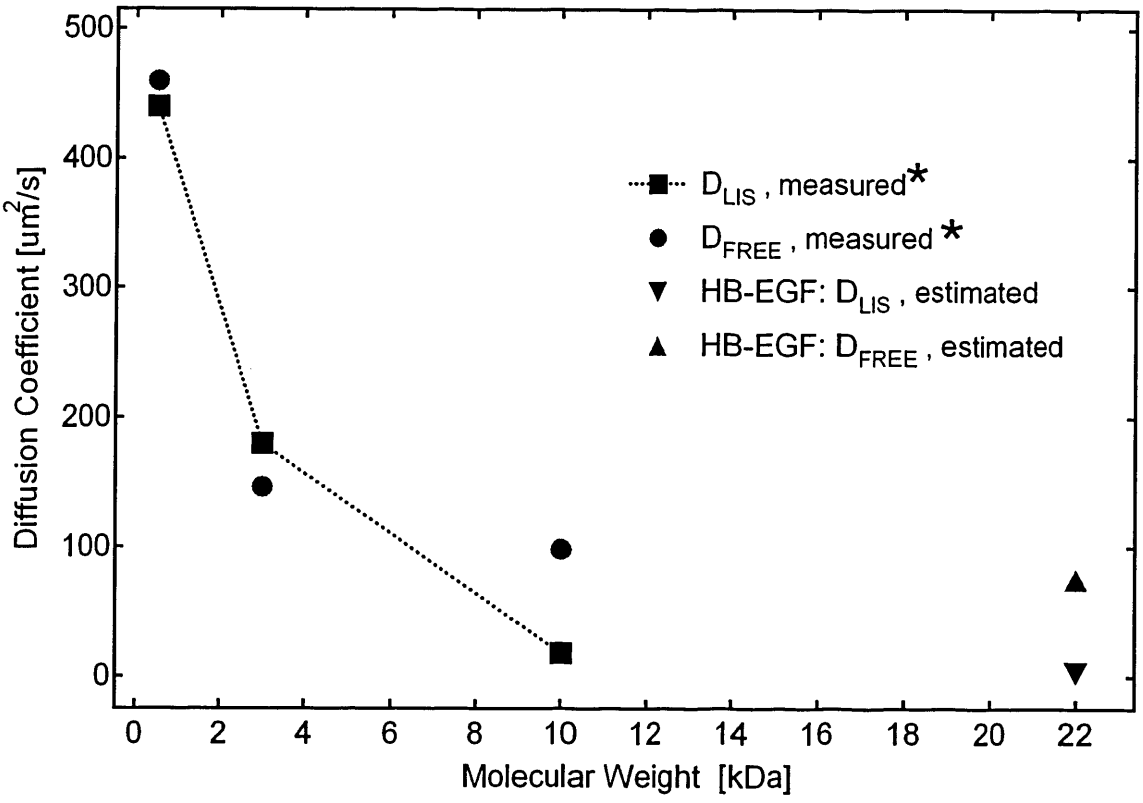

Figure 3.4 Diffusion coefficients for 524Da HPTS, and for 3 and 10kDa dextran molecules measured by Kovbasnjuk et al. (* indicates (Kovbasnjuk et al., 2000)) in the LIS of MDCK cells (squares connected by dashed line), and in free solution (circles). For a 10kDa dextran with D_{out} = D_{FREE} = 98 $\mu m^2/s$, hindered diffusion in the LIS was observed (D_{LIS}=18 $\mu m^2/s$) (6). For HB-EGF of size 22kDa we estimated a LIS diffusion coefficient of D_{LIS}=1.8 $\mu m^2/s$ (triangle pointing down), an order of magnitude less than that measured for a 10kDa dextran; outside the LIS the HB-EGF free solution value was estimated as D_{out} = D_{FREE} = 75 $\mu m^2/s$ (triangle pointing up), based on extrapolation of the measured free solution values assuming $D_{FREE} \propto (mol.wt.)^{-1/3}$

3.5 Rate sensitivity of extracellular mechanotransduction

Biomechanical forces develop on a range of time scales, from milliseconds for traumatic injury, to days to weeks or months for cellular proliferation and tissue morphogenesis. We have previously shown that the relevant time scale for compression of the LIS of airway epithelial cells and subsequent cellular signaling is on the order of seconds to minutes (Tschumperlin et al., 2004). Specifically, we know that at 20 minutes after the onset of $30cmH_2O$ of transcellular compressive stress a new steady state in LIS geometry is established, whereby the LIS width shrinks to 15% of its original value (Tschumperlin et al., 2004). However, due to limitations in the system available for imaging a few years ago we did not know the temporal behavior of the LIS width during this 20 minute span. We thus modeled a range of different rates of collapse of the LIS width occurring linearly over durations from 1 to 1200 seconds (Figs. 3.5a&b). We incorporated our estimates for hindered diffusion of HB-EGF inside the LIS, and free diffusion outside of the LIS. For clarity, the 60 second case is illustrated in both panels. As the figures indicate, the rate of change in LIS dimension plays a dominant role in defining both the rate of ligand accumulation, and the shape of relationship between ligand concentration and time.

a)

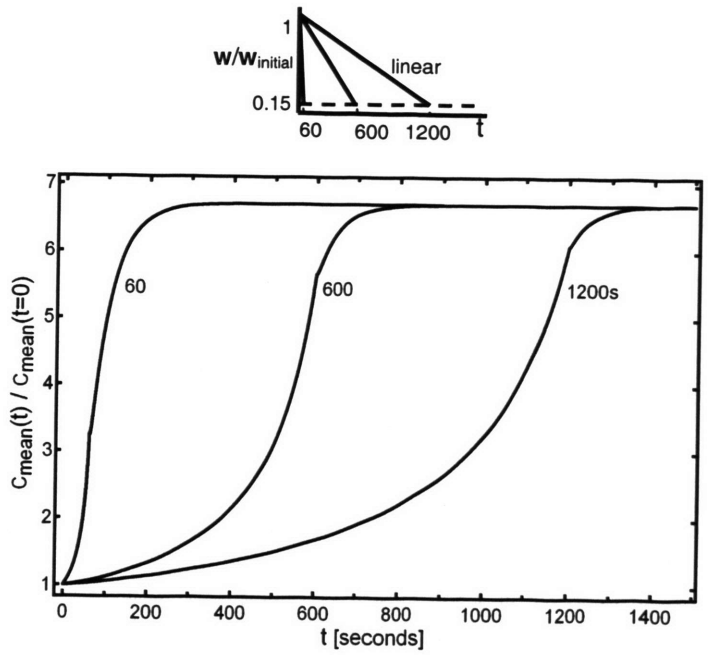

b)

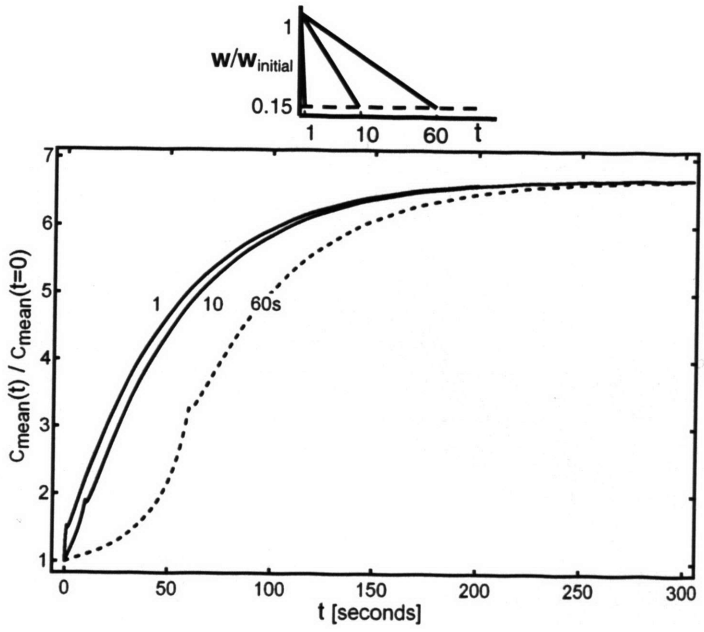

Figure 3.5 **a)** Incorporating the estimated HB-EGF diffusion coefficients (see Fig. 3.4), we examined three cases of LIS collapse when the LIS width decreased linearly to 15% of its initial, pre-collapse value (from1.5 to 0.225 μm) over $t_{collapse}$= 60, 600, 1200 seconds. **b)** Additional cases, where the same LIS collapse (to 15% of the initial width)

occurred in $t_{collapse}$= 1 and 10s (solid lines). The 60s collapse case from **a)** (dashed line) is shown for comparison. For all cases we assumed that the shedding rate is constant and equal to q = 10 molecules/cell/min.

In order to illustrate the localized variation in concentration induced by dynamic changes in LIS geometry, we calculated the HB-EGF concentration profiles in the LIS at several times during (solid lines) and after (dashed lines) LIS collapse for the 1 and 10s cases (Figs. 3.6a&b). These two cases are identical to those shown in Fig. 3.5b, but now represent concentration profiles as functions of depth and time.

Considering first the case where the LIS collapse occurs over 1s, we see that due to the rapid decrease in LIS width the concentration within the LIS becomes uniform, reaching a level equal to the most apical concentration (Fig. 3.6a). In the space immediately below the LIS the concentration tends to increase during the collapse due to convection, since velocities increase with width decrease (see equation (4a)). This increase in extra-LIS concentration (equaling about one quarter of the most apical LIS concentration at the end of the collapse) permeates several microns into the underlying media. After the collapse has ended, convection stops and diffusion alone becomes the governing process. This transition from a diffusive-convective to a purely diffusive regime results in a change in slope (at the end of the collapse) of the normalized mean concentration curve (Fig. 3.5b). After the conclusion of the LIS collapse the concentration profile transitions to a parabolic shape (Fig. 3.6a). Soon thereafter the effect of shedding ligand into a now much smaller space causes the concentration to increase until the new steady-state is reached after 300s (Fig. 3.6a).

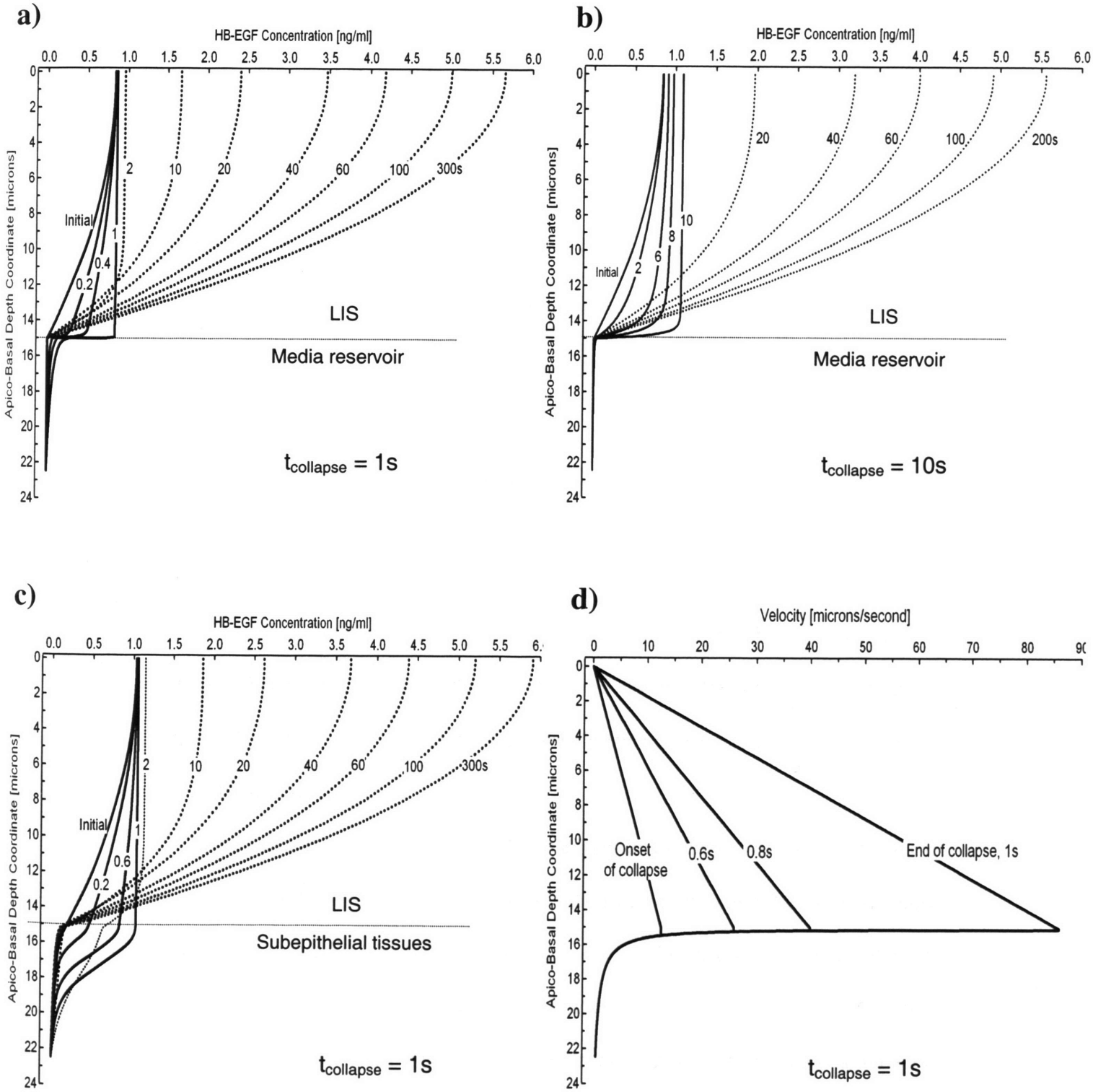

Figure 3.6 **a)** Evolution of concentration profiles for a 1s linear collapse (see Fig. 3.5b) for the *in vitro* case where: D_{LIS}=1.8 $\mu m^2/s$ and D_{out}=75 $\mu m^2/s$, LIS height h=15μm (boundary between LIS and underlying media), and concentration is assumed zero at 7.5

μm below the LIS boundary. Solid lines indicate times when the LIS width is changing (number next to curve represents the time in seconds corresponding to the profile), broken lines represent times after the LIS has reached its new steady-state geometry. **b)** Concentration profiles for a 10s linear collapse (see Fig. 3.5b) for the *in vitro* case with the same parameters as in part **a)**. **c)** Evolution of concentration profiles for a 1s linear collapse for the *in vivo* case where: $D_{LIS} = D_{out} = 1.8\ \mu m^2/s$. The geometry is the same as that described in part **a)**. **d)** Velocity profiles corresponding to case **a)**.

In the case of a 10s collapse (Fig. 3.6b) the concentration at the end of the collapse also tends to be uniform throughout the LIS and equal to the concentration at position x=0, however the x=0 concentration is greater at 10s than at the start of collapse. Another difference between the 1 and 10s cases is that much less increase in concentration below the LIS boundary is observed for the 10s collapse (diminished convective effects for the 10s case). The new steady-state is reached some 200s after the onset of collapse (Fig. 3.6b).

The previous two cases were intended to approximate the *in vitro* situation, where airway epithelial cells were grown on a porous substrate below which lies an essentially infinite reservoir of media. The HB-EGF diffusion coefficients inside and outside the LIS were assumed to be different based on the hindered diffusion in the LIS and free diffusion outside of the LIS. We modified these assumptions to simulate a scenario potentially encountered *in vivo*: instead of media below the cells, we assumed that sub-LIS tissues would hinder diffusion by the same amount as seen in the LIS ($D_{LIS} = D_{out} = 1.8\ \mu m^2/s$). For a very rapid 1s collapse, where again the LIS width decreases linearly to

15% of its initial, pre-collapse value, we determined the evolution of the concentration profiles (Fig. 3.6c). As in the 1s *in vitro* case there is a tendency toward uniform x=0 concentration throughout the LIS during the collapse. Here though, the concentration changes permeate much deeper below the cells. For instance, just prior to the end of collapse the ligand concentration 3 μm below the LIS reaches 40% of the LIS value, representing a 10-fold increase from an initial pre-collapse value of 0.04 to 0.4ng/ml in one second. These results highlight the fact that a rapid *in vivo* LIS collapse could transiently signal to underlying cells via a convective increase in ligand concentration that permeates into the surrounding tissues. This suggests a potential mechanism for communicating events that affect the epithelium to subepithelial tissues.

To see how the LIS collapse affects bulk velocity profiles inside and outside of the LIS, we examined the 1s *in vitro* case from above (see Figs. 3.6a&d). The bulk velocity profile inside the LIS is linear (starting from zero at the impermeable tight junction x=0), whereas outside the LIS the velocity decreases proportionally to the inverse of the radius (Fig. 3.6d and Fig. 3.1). Both the linear and 1/r dependence follow from conservation of mass (see equations (4a,b)). For the 1s *in vitro* case the corresponding local Peclet numbers along the depth of the LIS ($Pe = V_x h / D_{LIS}$) can be calculated to range from 0 at x=0 to >700 at the LIS boundary. Thus, since $Pe >> 1$ for most of the LIS, convection dominates during rapid collapse. Furthermore, a Peclet number can be obtained across the LIS width w, ranging from $Pe = \dot{w}(w/2)/D_{LIS} = 0.5$ at the LIS wall to 0 at a distance $w/2$ from the wall. Here $\dot{w}$ represents the rate of change of the width w, i.e. the velocity of the LIS wall. The small values of the Peclet number over the LIS width, combined with the large height-to-width

ratio of the LIS geometry, justify our use of a 1-D model in which we assume uniform concentrations across the LIS width.

3.6 Determining maximum rate of ligand concentration change during LIS collapse

Computational and experimental studies have demonstrated that receptor activation and downstream signaling are influenced not only by the magnitude, but also by the rate of ligand concentration change in the cellular microenvironment (Sasagawa et al., 2005). To explore this facet of transduction in our model, we first differentiated the normalized C_{mean} curves shown in Figs. 3.5a&b with respect to time and then found the maximum rate of concentration change. In Fig. 3.7, the maximum rate of concentration change (i.e. the maximum slope of the fold-mean curves of Figs. 3.5a&b) is plotted versus the time-derivative of the corresponding collapse of LIS width (see Figs. 3.5a&b $w/w_{initial}$ linear relationships). In our simulations the LIS width decreased linearly over time and the resulting time derivatives (i.e. rate of collapse) were constant for each case. The largest rate of concentration change was for the fastest collapsing LIS, i.e. the 1 second collapse. A 4-fold decrease in the maximum rate of ligand accumulation was observed when comparing the 10s case to the 1s case, with a small further decrement of 10% occurring between the 10 and 60s cases. The slower collapsing LIS cases (such as 600 and 1200s) exhibited maximum rates of ligand concentration change that were lower by more than an order of magnitude when compared to the 1s case. Thus, the rate of LIS geometry change profoundly affects the peak rate of LIS ligand concentration change.

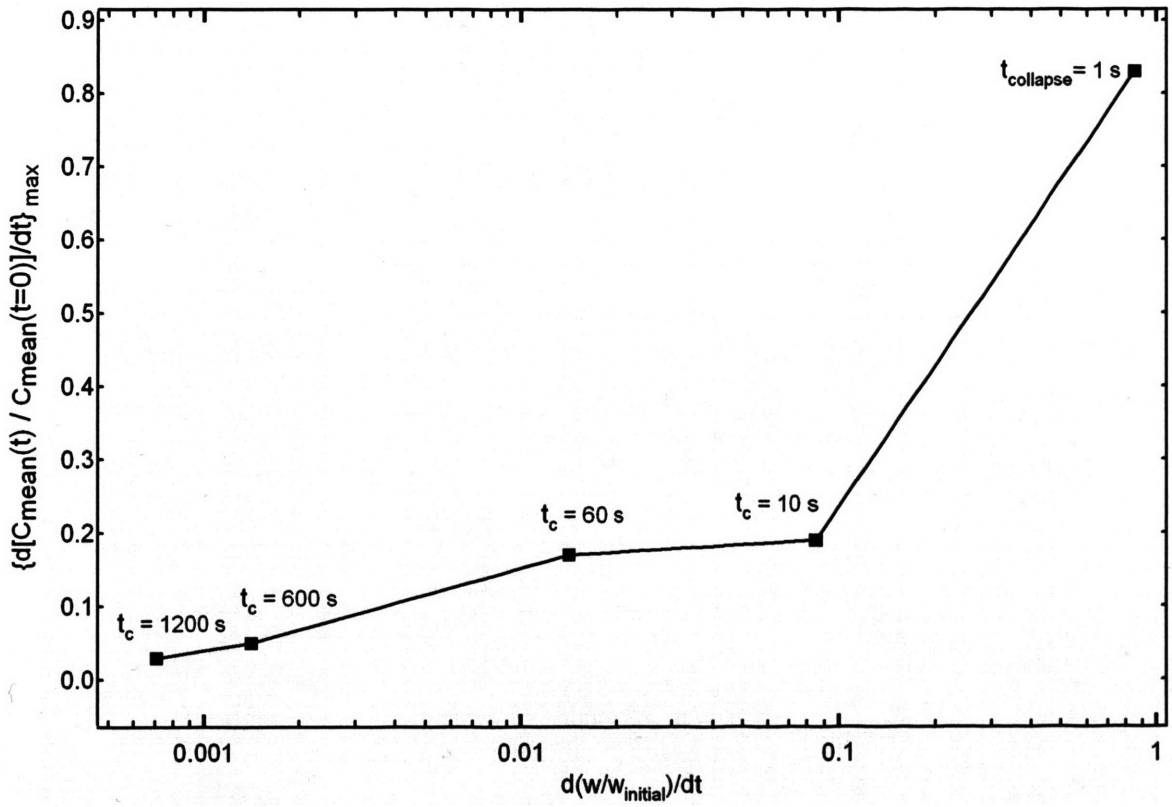

Figure 3.7 Maximum rate of change of the fold-mean-concentration as a function of the corresponding rate of LIS collapse for five cases from Figs. 3.5a&b. Individual squares represent the maximum rate of concentration change for a given rate of collapse. For example, in the case of $t_{collapse}$=10s the LIS collapses by 85% linearly over 10s and thus the rate of collapse is constant and equal to 0.085 s^{-1}. For this 10s collapse, the maximum rate of change of concentration was obtained by finding the largest slope of the $C_{mean}(t)/C_{mean}(t=0)$ curve (see 10s curve in Fig. 3.5b).

The results of our analysis demonstrate that while the magnitude of ligand concentration change depends on the change in w, the kinetics of ligand accumulation depend predominately on $\dot{w}$ and D. Strikingly, these results suggest that all other parameters being equal, the fastest change in ligand concentration will occur for the highest diffusivity (and hence, smallest) molecules. How then can we explain the selective role for HB-EGF in transducing mechanical stress in human airway epithelial cells exposed to compressive stress (Tschumperlin et al., 2004; Tschumperlin and Drazen, 2001; Tschumperlin et al., 2002) when it is known that these cells can shed other ligands that bind to the same receptor (e.g. TGF-alpha) and exhibit higher diffusivities?

3.7 HB-EGF vs. TGF-alpha concentration dynamics

While proteolytically processed and shed HB-EGF is ~22kDa in size, shed TGF-alpha (and EGF) is about 4 times smaller, being ~5.5kDa (Harris et al., 2003; Raab and Klagsbrun, 1997). If we were to assume free diffusion of each ligand, the difference in ligand size would predict a ~35% difference in the expected free diffusion coefficient for theses two ligands (Fig. 3.4). However, returning to the diffusivity measurements made in the LIS of MDCK cells, it was found that these two ligands straddle the molecular size range over which diffusion becomes significantly hindered in the LIS (Kovbasnjuk et al., 2000). Thus, the diffusivity in the LIS can be approximated as $D_{LIS} = 1.8\mu m^2/s$ for HB-EGF (22kDa), while for TGF-alpha (5.5kDa) the $D_{LIS} = 120\mu m^2/s$ is the same as for free diffusion (see Fig. 3.4). If we further assume both ligands are shed at the same rate q=10 molecules/cell/min, the solution of the governing diffusion-convection equations during a 60 second collapse yield the absolute mean concentration curves (not normalized) for

HB-EGF and TGF-alpha shown in Fig. 3.8a. For comparison, the case assuming free-diffusion for HB-EGF both inside and outside the LIS ($D_{LIS}=D_{out}=75$ $\mu m^2/s$) is also shown (dashed line in Fig. 3.8a). Note that the units here are picoM; thus while the mass concentration of free-diffusing HB-EGF is higher than for TGF-alpha, its molar concentration is lower due to its larger molecular weight.

We observe that for hindered HB-EGF in the LIS, the mean absolute concentrations are an order of magnitude higher those of TGF-alpha (Fig. 3.8a). A corollary to this result is that in order to have a similar LIS concentration for both ligands, with the assumption of hindered diffusion in the LIS for HB-EGF, the cell must shed TGF-alpha at a rate ~10 times higher than that of HB-EGF. Furthermore, this result reveals two potential explanations for a selective role for HB-EGF in extracellular mechanotransduction. In the first case, the different mean concentrations that arise in the LIS as a consequence of different ligand diffusivities could place HB-EGF and TGF-alpha on different parts of a EGFR-ligand binding curve (Lauffenburger et al., 1998) (see Fig. 3.8b). Assuming a constant and equivalent shedding rate for each ligand, and equivalent ligand-receptor affinities (Jones et al., 1999) and signaling properties, the absolute concentrations of each of the ligands at the start and end of collapse correspond to the values of Fig. 3.8a. Therefore, the differences in HB-EGF and TGF-alpha concentrations could result in HB-EGF shifting up the EGFR-ligand binding curve. On the other hand, the low concentration of TGF-alpha (as well as free-diffusing HB-EGF) could place it on the flat portion of the curve, rendering it an ineffective activator of the EGFR in response to mechanical deformation (Fig. 3.8b).

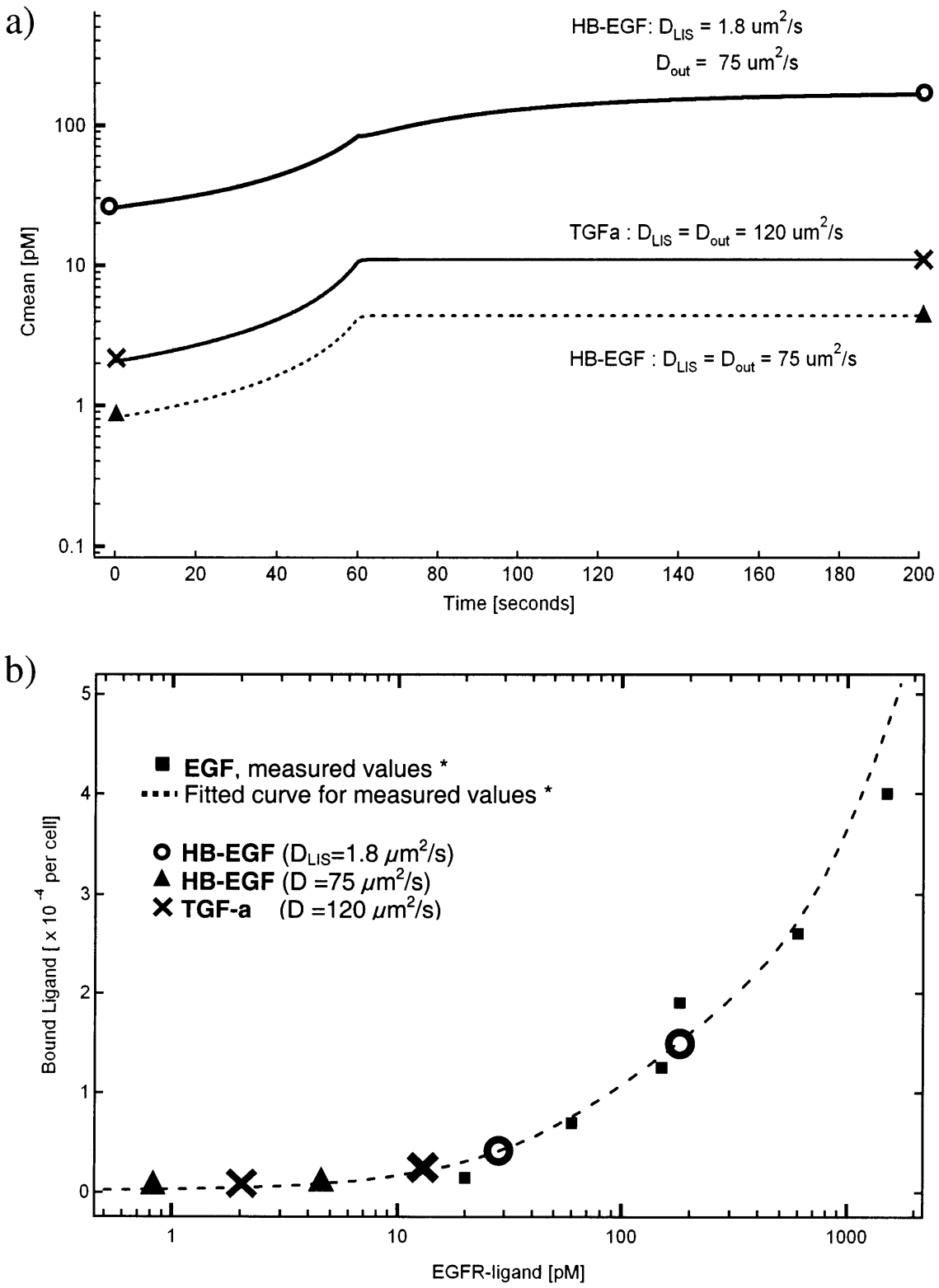

Figure 3.8 **a)** Mean molar LIS concentration for HB-EGF (top solid and bottom dashed curves) and TGF-alpha (solid middle curve) for a 60s LIS collapse when the LIS width

decreases to 15% of its initial, pre-collapse value (from 1.5 to 0.225 μm). For HB-EGF, we examined two cases: free solution inside and outside of LIS with $D_{LIS} = D_{out} = 75$ $\mu m^2/s$ (bottom dashed curve), and hindered diffusion in the LIS with $D_{LIS} = 1.8$ $\mu m^2/s$ and free diffusion outside of the LIS with $D_{out} = 75$ $\mu m^2/s$ (top solid curve). For TGF-alpha, free diffusion was assumed both inside and outside of LIS with $D_{LIS} = D_{out} = 120$ $\mu m^2/s$ (middle solid curve). In all cases shedding rate was constant and equal to q = 10 molecules/cell/min. The open circles represent hindered HB-EGF mean concentration at the start and after collapse, while crosses and triangles represent free diffusion of TGF-alpha and HB-EGF mean concentrations, respectively pre- and post-collapse. **b)** EGFR-ligand biding curve (dashed line) based on fitting the experimental values (solid squares) (* indicates (Lauffenburger et al., 1998)). A portion of the curve (relevant to our concentration ranges) was used. The final point on the actual curve was $20x10^3$ pM and the corresponding bound ligand was $11x10^4$ per cell (Lauffenburger et al., 1998). The mean concentrations for HB-EGF and TGF-alpha for pre- and after-collapse are represented by the symbols shown in panel **a)**. TGF-alpha concentration increases due to the collapse, but (like free-diffusion HB-EGF) remains on the flat part of the curve, whereas hindered HB-EGF concentration increases along the steep part of the curve, rendering it a more effective molecule for receptor activation.

A second potential explanation is that the molecular sieving properties of the LIS might become amplified by the geometric decrease in LIS space (Fig. 3.9). While we have thus far assumed that during the LIS collapse the shrinking of the intercellular space does not affect ligand diffusivity, the decrease in LIS width could form a more tightly

packed space and a greater barrier to diffusion, especially for large, highly charged molecules like HB-EGF, while leaving smaller ligands like TGF-alpha relatively unaffected. We modeled this putative effect by assuming that the size/charge interactions (Dowd et al., 1999; Kovbasnjuk et al., 2000) would decrease the HB-EGF diffusion coefficient during the course of a LIS collapse. In Fig. 3.9 we illustrate several scenarios in which the HB-EGF diffusivity decreases linearly along with the linear LIS width decrease over 60s (see Figs 3.5a & 3.9). A decrease in D_{LIS} during collapse could amplify the increase in HB-EGF concentration, potentially mediating or magnifying cellular mechanotransduction.

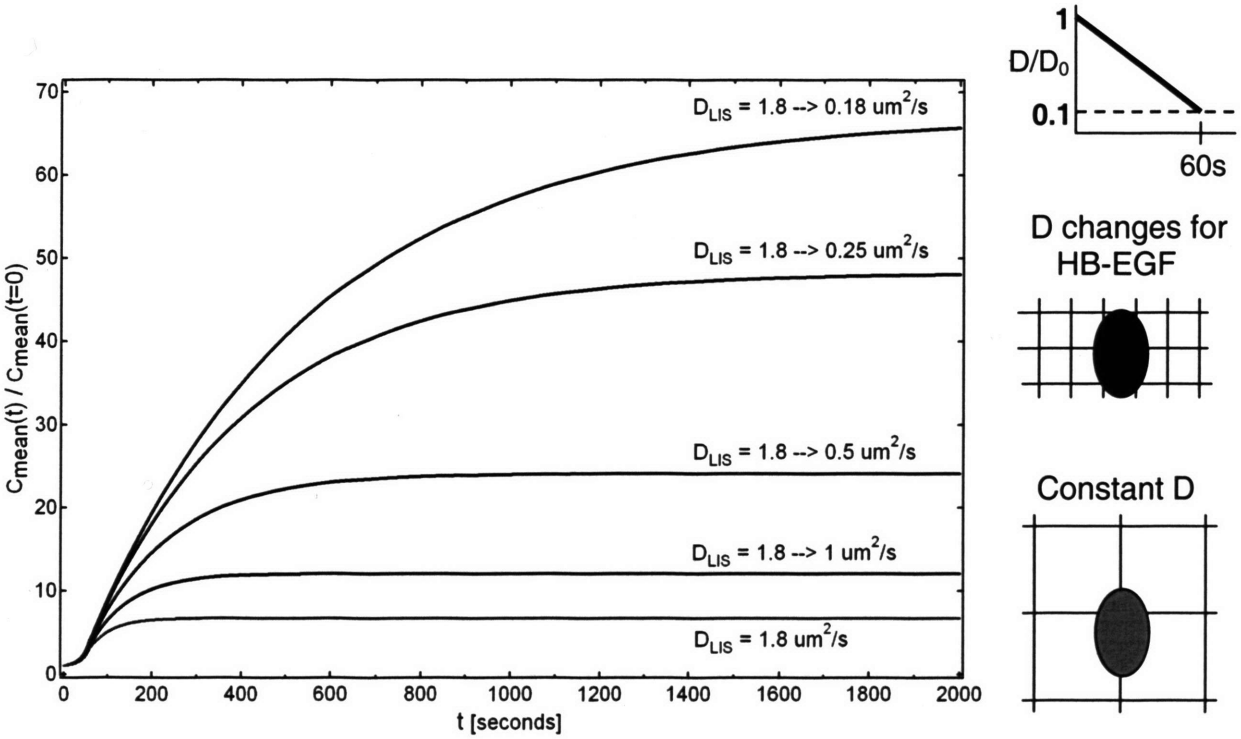

Figure 3.9 Fold change in mean concentrations for various geometry-dependent changes in diffusion coefficients during LIS collapse. All cases are for a 60s LIS collapse where the LIS width decreases to 15% of its initial, pre-collapse value (from 1.5 to 0.225 μm,

Fig. 3.5b). The case of constant HB-EGF diffusion coefficient D_{LIS}=1.8 $\mu m^2/s$ is shown as the bottom curve. In the other four cases we assume that the collapsing LIS causes a linear decrease (following LIS geometry) in HB-EGF diffusion coefficient during the 60 second collapse. For example, the top curve D_{LIS}=1.8→ 0.18 $\mu m^2/s$ indicates the case where the diffusion coefficient changes linearly over 60 seconds from the initial value of 1.8 $\mu m^2/s$ to the final value of 0.18 $\mu m^2/s$ (see side panel). In the other three cases of decreasing D_{LIS}, the diffusion coefficient linearly decreases over 60 seconds from 1.8 to 0.25, 0.5, and 1 $\mu m^2/s$. The side schematics illustrate how the shrinking volume of the LIS could considerably amplify the effect of hindered diffusion.

3.8 Discussion

In this chapter we developed a computational framework to help understand how the concentration of constitutively shed ligands changes as a result of simple geometric changes in the spaces separating cells. Our computational model includes both diffusive and convective effects, allowing us to study the temporal relationship between deformation and ligand accumulation, and the dependence of this relationship on system characteristics such as ligand diffusivity, shedding rate, and rate of deformation. The model geometry is expanded over previous efforts (Tschumperlin et al., 2004) to include both the LIS and the underlying space, thereby also providing an assessment of the effect of convection and diffusion on ligand concentration in the basal space underlying the LIS.

The modeling results reveal several key facets of extracellular mechanotransduction. How fast the local ligand concentration changes depends primarily on the rate of change of the extracellular geometry (Figs. 3.5a&b); on the other

hand, the magnitude of the change in concentration (at steady-state) is entirely determined by the magnitude of the geometry change. While the fold-change in ligand concentration that occurs with LIS collapse is independent of the ligand shedding rate, the absolute concentration of ligand is not (Fig. 3.8a). Thus, ligands with different shedding rates could occupy different regimes on a receptor dose-response curve (Fig. 3.8b). Similarly, the absolute concentration of a ligand depends on its diffusivity; low diffusivity molecules accumulate at higher baseline concentrations when shed into the LIS, and vice versa (see equation (2) and Fig. 3.8a). We used these system properties to propose two explanations for the selective role of HB-EGF as a key mechanotransduction ligand in bronchial epithelial cells (Tschumperlin et al., 2004; Tschumperlin et al., 2002); both mechanisms are based on the large size of HB-EGF relative to other EGF-family ligands (Harris et al., 2003), and the assumption that HB-EGF diffusion will be hindered in the LIS (Kovbasnjuk et al., 2000).

By including convection and expanding the model geometry, we were able to examine how dynamic changes in LIS geometry alter the ligand concentration in the underlying space (which we chose to be either a media reservoir or subepithelial tissues, Figs. 3.6a-c). We showed that for low diffusivity molecules and fast geometric changes, convection leads to large but transient increases in ligand concentration that permeate several microns below the cellular layer. This convective effect could allow nearly immediate communication of the mechanical state of epithelial cells to underlying cells, which frequently share responsibility for management of tissue architecture (Swartz et al., 2001).

The modeling results demonstrate how the varying kinetics of geometric changes in the extracellular space are translated into varying rates of change of ligand concentration (Fig. 3.6). Recent experimental and computational studies have clearly demonstrated that the rate of ligand concentration change encodes important signaling information (Sasagawa et al., 2005; Schoeberl et al., 2002). Together these observations raise the possibility that cellular mechanotransduction through the proposed extracellular mechanism could discriminate between different rate processes, based on the velocity of ligand accumulation and subsequent receptor activation.

Our results raise other questions. For example, what are the effects of varying the magnitude or rate of loading on geometric changes, and how do these loading conditions relate to various physiological scenarios? While not available when this model was first developed, dynamic measures of the geometric response of the interstitium to loading, as detailed in chapter 5, can be coupled to the model described here to predict the overall relationship between mechanical loading and local autocrine ligand concentration (see Chapter 7).

Computational modeling of the EGFR system, from autocrine activity (Maheshwari et al., 2001; Monine et al., 2005; Shvartsman et al., 2002a; Shvartsman et al., 2002b; Shvartsman et al., 2001) to receptor trafficking (Lauffenburger and Linderman, 1993; Resat et al., 2003; Wiley et al., 2003) and downstream signal pathways (Kholodenko et al., 1999; Sasagawa et al., 2005; Schoeberl et al., 2002; Wiley et al., 2003), has been essential to our understanding of this important biological pathway. The model described here explores a previously ignored idea in which changes in the concentration of shed ligands in an extracellular compartment, occur based solely on

geometric changes. If linked together with previously developed cell membrane and intracellular compartmental models of ligand kinetics, receptor trafficking, and intracellular signaling, the combined models could provide a comprehensive framework for understanding how mechanical or architectural changes in cells and tissues that modulate extracellular geometry are converted into biological signaling responses.

To further explore how the mechanical stimulus (i.e. an applied transcellular pressure gradient) affects both the ligand shedding rate and the LIS geometry we performed a series of biochemical and imaging experiments. The results and details of these experiments are described in the next two chapters, starting with the ligand shedding measurements. Finally, in the last chapter, we return to the numerical model presented here and incorporate our experimental findings.

4. Measuring shedding rates of EGFR ligands

4.1 Introduction

Cultured normal human bronchial epithelial (NHBE) cells express both the EGF receptor (EGFR) and the corresponding ligands. In previous work (Tschumperlin et al. 2004) we have established that the ligand HB-EGF is the key molecule linking changes in extracellular geometry to the autocrine loops involved in mechanotransduction. These loops consist of the EGFR and ligands that are constitutively produced and shed into the extracellular space.

Our modeling (see Chapter 3) has focused on the basolateral cell surface, where, via sheddase activity, ligands enter the lateral intercellular space (LIS). The cell synthesizes the ligands and inserts them on the cell membrane (this is the pro-form). Then the sheddase cleaves the pro-form so that the ligand is released into the LIS (soluble form). Once in the LIS, the ligand can diffuse down its concentration gradient, traversing the LIS in the apico-basal direction towards the underlying media reservoir. A concentration gradient for the ligands exists because at the apical side tight junctions form an impermeable barrier for ligands while on the basal side, in the underlying media reservoir, the concentration of ligand is essentially zero. This means that ligands shed in the LIS will tend to diffuse towards the basal side, since the concentration of ligand in the LIS (due to shedding) will always be higher that in the media reservoir (Kojic et al., 2006; Tschumperlin et al., 2004). Even though autocrine loops seem to play an important role in our cultured NHBE cells (Kojic et al., 2006; Tschumperlin et al., 2004), the exact rate of ligand shedding is not known. In this chapter, we present measurements of the rate

of ligand release, and also study the effect of a pressure-induced LIS collapse on the rate of shedding.

4.2 Measuring the autocrine release of EGFR ligands

In order to determine the release of EGFR ligands into the extracellular space we measured the concentrations of various ligands in the culture media below the cells at different time intervals (DeWitt et al., 2002; DeWitt et al., 2001; Dong et al., 1999; Dong and Wiley, 2000; Lauffenburger et al., 1998; Oehrtman et al., 1998). Our approach was based on the idea is that if ligands diffuse out of the LIS they should accumulate in the basal media (DeWitt et al., 2001; Lauffenburger and Linderman, 1993; Oehrtman et al., 1998). Through multiple sampling of the media over a given time period information about the kinetics of ligand release could be inferred (DeWitt et al., 2001; Oehrtman et al., 1998). We assume that a ligand cleaved from the pro to soluble form has one of two fates: it can bind to the EGF receptor somewhere on the LIS surface (and get internalized as part of the ligand-receptor complex) or it can diffuse towards the basal side and enter the media reservoir (see Fig. 4.1). The analysis of the media will thus give us a ligand escape rate (DeWitt et al., 2001; Oehrtman et al., 1998).

To get an estimate of the amount of ligand shed, an antibody was used to block the binding site of the EGFR. If all of the EGFR sites are blocked then all of the ligand shed into the LIS should diffuse down its concentration gradient and appear in the underlying media. Furthermore, a linearly increasing accumulation of ligand in the media over a given time period implies that the rate of ligand shedding is constant over the given time interval (DeWitt et al., 2001; Oehrtman et al., 1998).

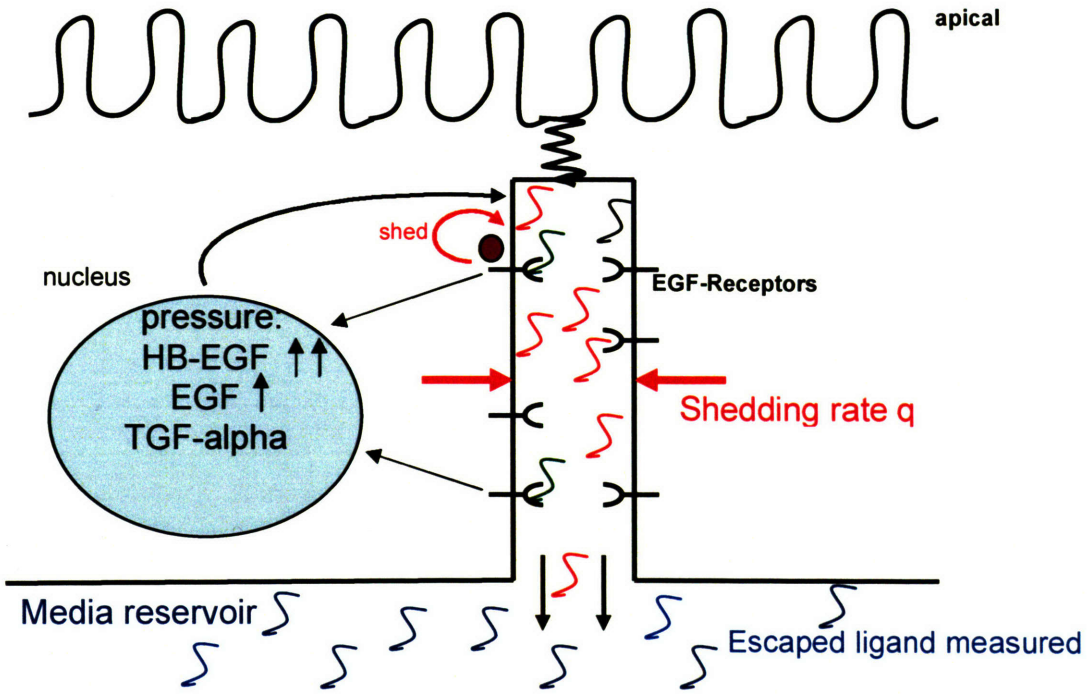

Figure 4.1 The EGFR-ligand autocrine loop. Black indicates the pro-form of the ligand; red represents soluble unbound ligand; green is bound ligand; and blue is ligand that has traversed the LIS and appeared in the underlying media reservoir. The previously determined effect of pressure on gene transcription of HB-EGF (highly increased), EGF (slightly increased) and TGF-alpha (no change) is shown in the light blue circle representing the nucleus.

Finally, the effect of pressure can be determined by establishing a transcellular pressure gradient and sampling the media. Applying the same principle of blocking the all of the EGFR receptors should allow the comparison between normal, basal shedding and the rate of shedding when cells are subjected to a transcellular pneumatic pressure gradient.

For media analysis we used ligand-specific Enzyme-Linked ImmunoSorbent Assays (ELISA). The first set of experiments involved measuring the effect of adding an antibody that would block the EGFR binding site. In order to determine what concentration of antibody should be used, we had to establish a dose-response curve. From this curve, we could pick out a concentration of antibody that would be close to the saturating response. Thus, we hoped to choose a concentration that would block the binding sites for almost all of the basolateral EGF receptors. To obtain the dose-response curve we focused on one specific ligand: TGF-alpha.

The procedure was as follows. The cell culture medium was changed to an EGF-free media the night before the experiment was started and again at the start of the experiment (t=0). This was done in order to minimize the amount of available EGFR-ligands. Then, at t=0, either EGF-free media or a prescribed concentration of an anti-EGFR antibody (termed the 225 antibody by its makers, Neomarkers, Fremont, CA) was put in each well. The specific values for the 225 antibody in the underlying media were 5, 10, 20, and 50 μg/ml. After 36 hours, the media was collected and a TGF-alpha ELISA was performed using a commercially available kit (R&D Systems, Minneapolis, MN). These results (see Fig. 4.2) suggested that 20μg/ml would be a concentration that would

give an almost saturating response and thus this concentration was used in subsequent experiments.

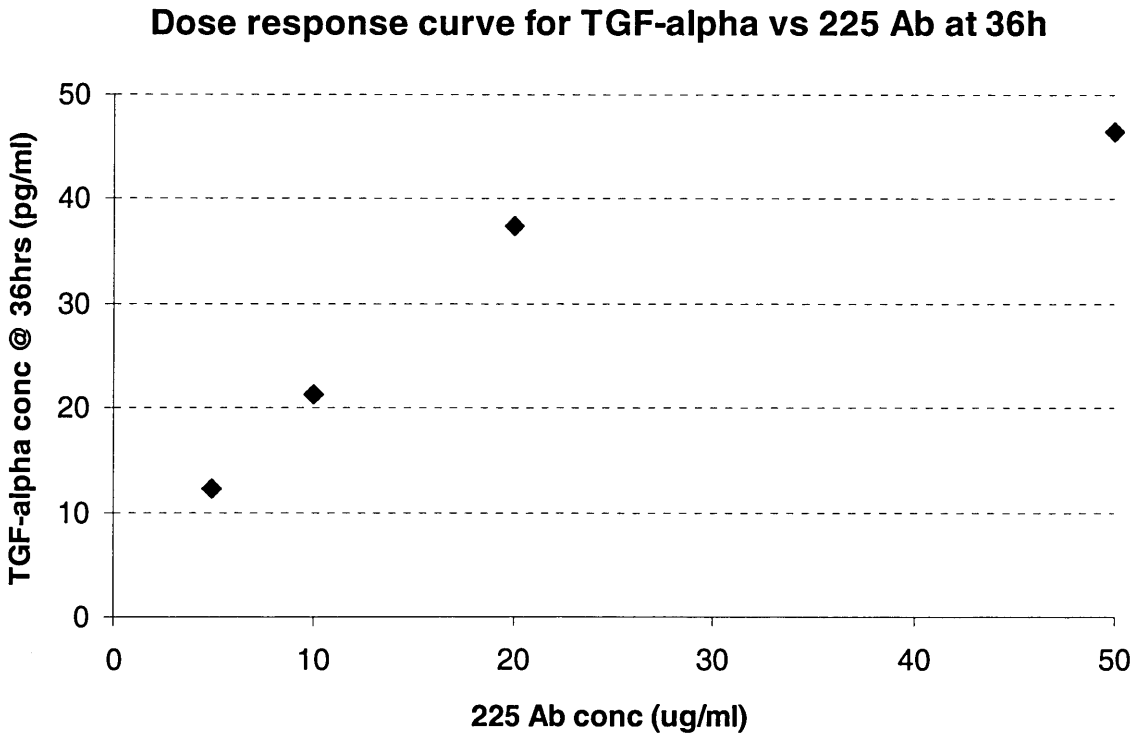

Figure 4.2 Preliminary dose-response curve for the 225 antibody, which blocks the ligand binding site on the EGFR. All samples were collected at 36 hours and analyzed for the amount of TGF-alpha present.

To determine if there was any effect of the time at which all of the samples were collected (36 hours in Fig. 4.2), a second round of experiments was performed where the time interval was increased to 48 hours. Also, an additional concentration of 225 Ab (1μg/ml) was examined and duplicate experiments were done to ensure reproducibility (see Fig. 4.3).

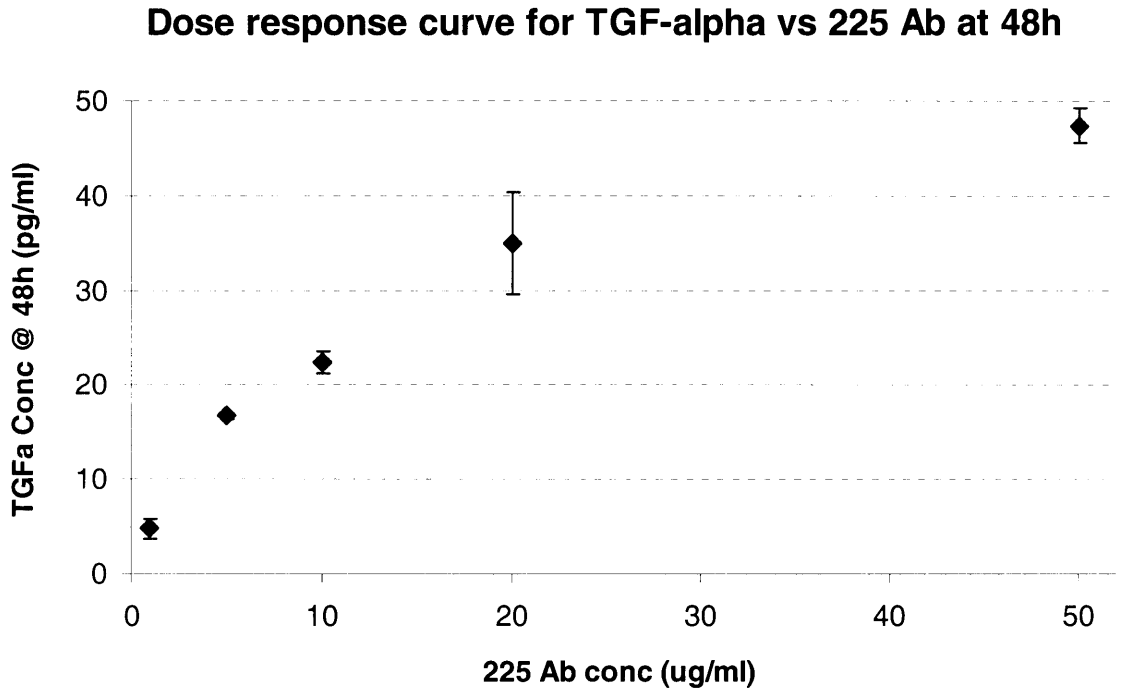

Figure 4.3 Dose-response curve for the 225 antibody, which blocks the ligand binding site on the EGFR. Duplicate experiments (error bars indicate the standard deviation) where all samples were collected at 48hours and analyzed for the amount of TGF-alpha present.

The dose-response curves for 36 and 48 hours are very similar, even though they were performed on different days with cells from different donors. This further justified the use of 20μg/ml as an appropriate EGFR-blocking antibody concentration.

Once the optimal concentration of antibody was chosen, experiments for the determination of the shedding rate of ligands under basal conditions were performed. Three ligands were examined: TGF-alpha, EGF, and HB-EGF. For all three ligands the conditions were identical, in fact the same media (collected from a given well) was used in the analysis for all of the ligands. The experimental conditions were such that media

was collected at time = 8, 24, and 48 hours. Thus three wells (one for each time-point) were treated with 20μg/ml of the 225 EGFR-blocking antibody and in another three wells nothing was added (these three wells represent the controls). To ensure reproducibility three identical experiments were performed. Also tested was the effect of using Full media (which is normally used to feed the cells and contains about 140 ng/mL of EGF) versus EGF-free media.

Data for each of the three ligands is presented separately. For TGF-alpha a commercial ELISA was used to analyze all of the above conditions and times. The first step was to obtain the standard curve for the ELISA plate on which the samples were analyzed. This was done by measuring known amounts of TGF-alpha (i.e. standard concentrations) and fitting a power-law curve through the standards (see Fig. 4.4).

A plate reader detected the optical density of the colorimetric reaction which was related to the TGF-alpha concentration by the power-law fit. Plotted on a log-log scale, the power-law curve should be a straight line (see Fig. 4.4). The lowest standard value on the standard curve represented the detection limit for the ELISA (in this case 15pg/ml).

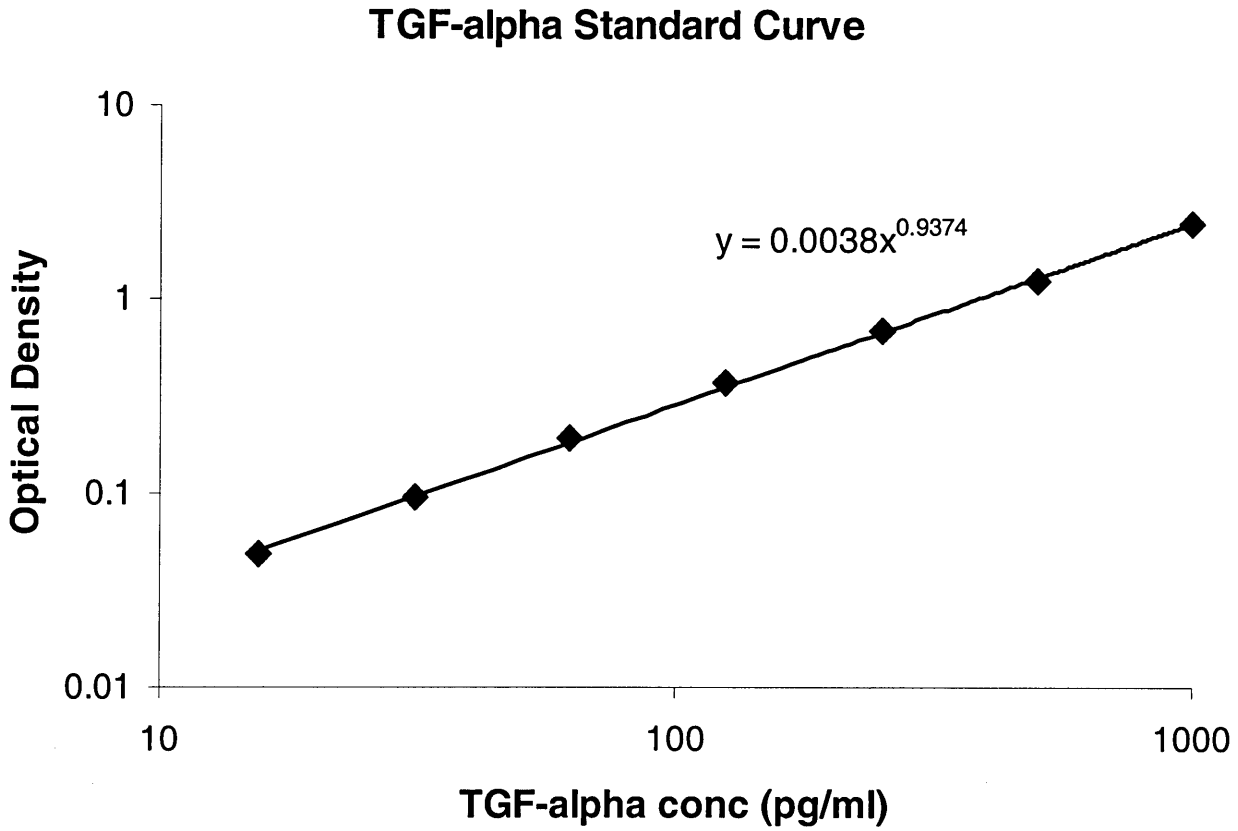

Figure 4.4 Standard curve for the TGF-alpha ELISA. Optical density was recorded by the plate reader and related to concentration by the power-law fit. The lowest concentration (15pg/ml) represents the detection limit of the ELISA.

The results of the shedding rate experiments are summarized in Figure 4.5, and indicate that there was no difference in TGF-alpha accumulation for Full media (with EGF present) and EGF-free media (i.e. very small difference in the corresponding values for the two types of media). Furthermore, all of the controls were well below the detection limit of the ELISA which suggests that normally very little TGF-alpha escapes the LIS and reaches the underlying media reservoir. In other words, the TGF-alpha capture efficiency in the LIS of our NHBE cells was very high (>90%).

The presence of 20μg/ml of the 225 EGFR-blocking antibody resulted in a detectable amount of TGF-alpha in the media (see red squares and dark blue diamonds in Fig. 4.5). As time progressed from 8 to 24 to 48 hours, the TGF-alpha concentration in the media reservoir increased linearly (see top two curves in Fig. 4.5). These linear curves were then used to calculate a shedding rate for TGF-alpha.

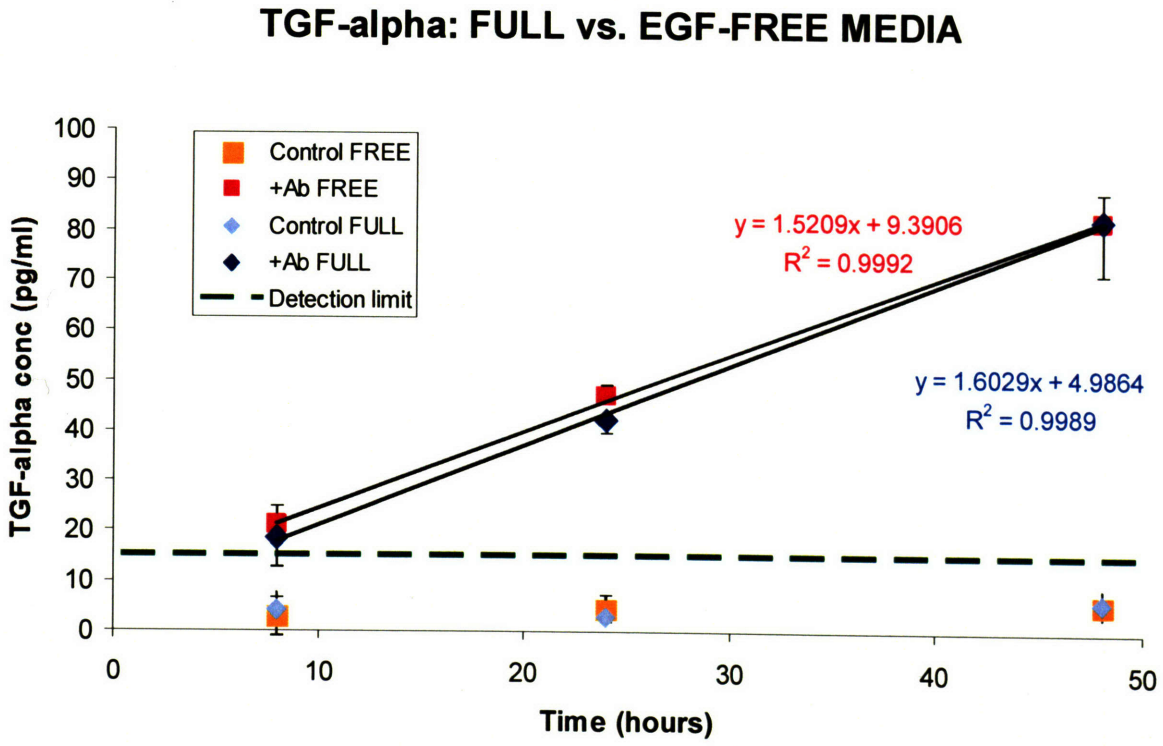

Figure 4.5 TGF-alpha accumulation in the media for Full (diamonds) and EGF-free media (squares). The detection limit of the ELISA is indicated by the dashed green line. The controls for both Full (light blue diamonds, labeled Control FULL) & EGF-free media (yellow squares, labeled Control FREE) were below the detection limit. With the presence of 20μg/ml of the 225 EGFR-blocking antibody, the accumulation of TGF-alpha followed almost an identical linear trend (see fitted lines) for both Full (dark blue diamonds, labeled +Ab FULL) & EGF-free media (red squares, labeled +Ab FREE). Error bars indicate the standard deviation of the means for three identical experiments.

The analysis for the EGF ligand was analogous to TGF-alpha. Using the same media from the same experiments a commercial EGF ELISA was performed for all of the conditions stated above: Full and EGF-free media; and with and without the presence of 20μg/ml of 225 EGFR-blocking antibody. The standard curve for the EGF ELISA is shown in Fig. 4.6.

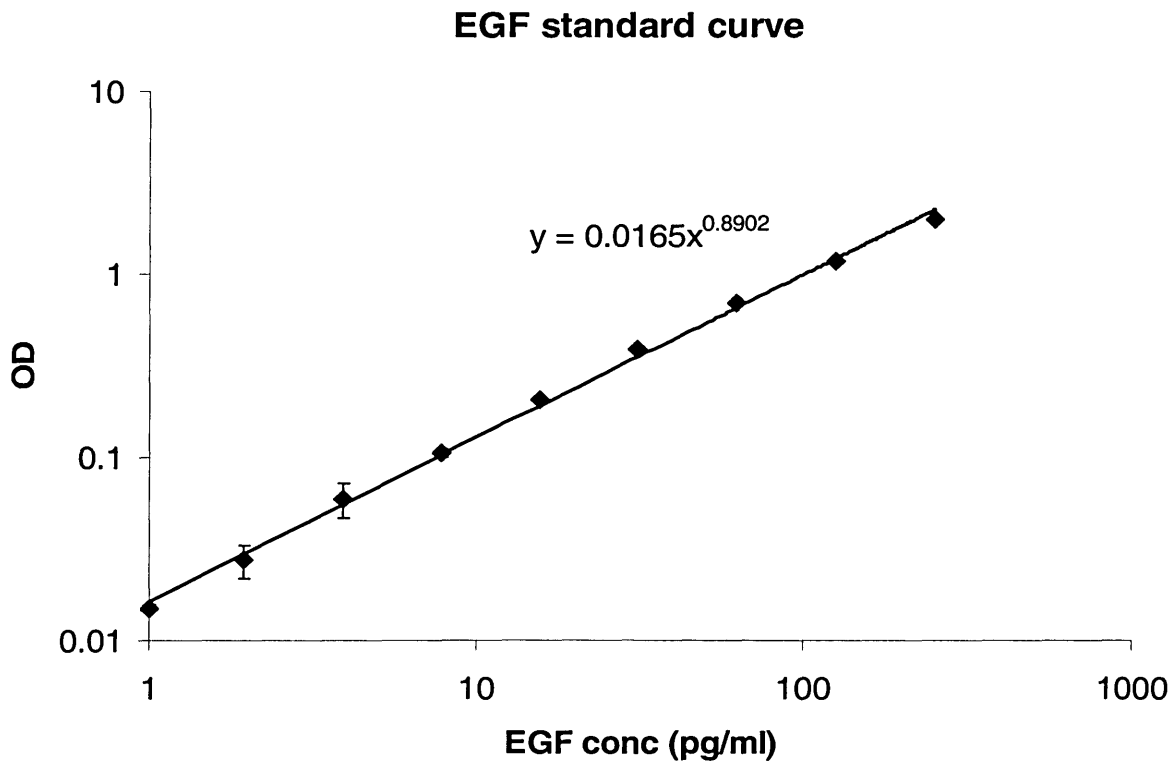

Figure 4.6 Standard curve for the EGF ELISA. Optical density (OD) was recorded by the plate reader and related to concentration by the power-law fit. The lowest concentration (1pg/ml) represented the detection limit of the ELISA.

The results for the EGF-free media experiments are presented in Fig. 4.7. They indicate that although the accumulation was linear (as in the case for TGF-alpha, see Fig. 4.5) most of the values were close to or below the detection limit of the ELISA.

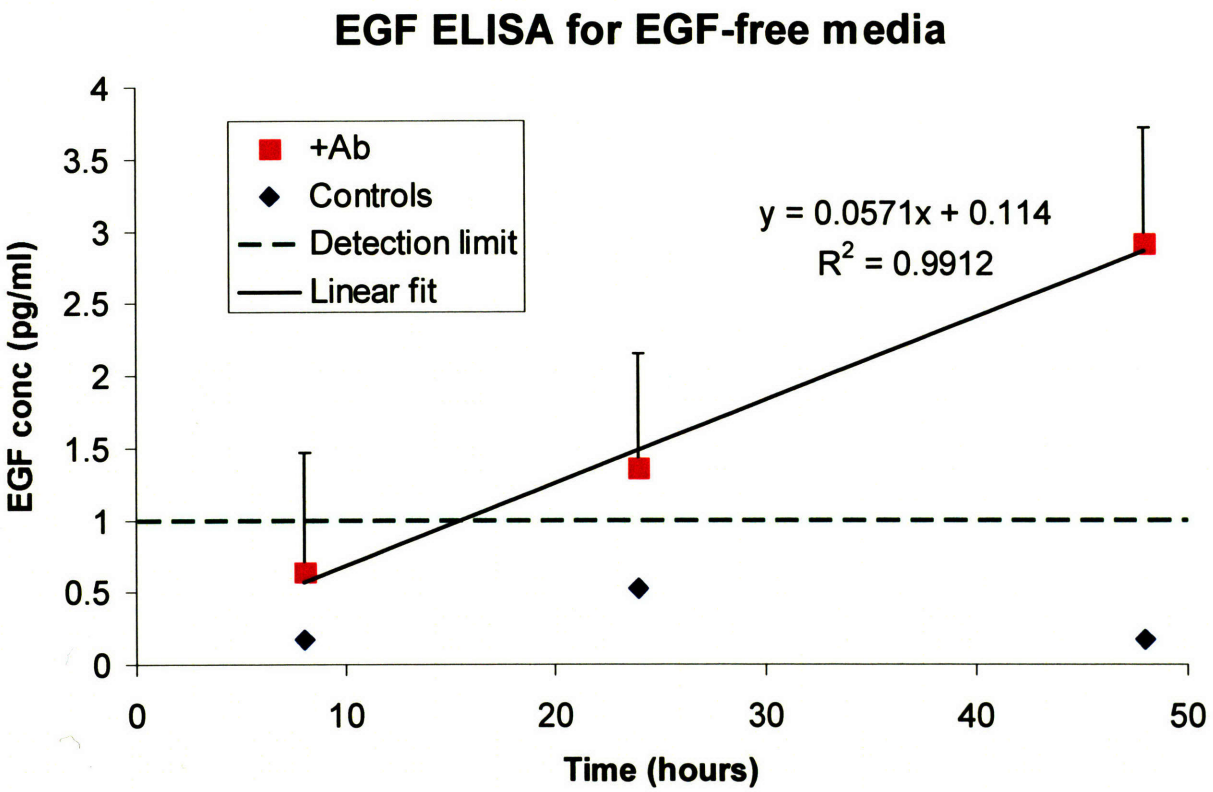

Figure 4.7 EGF accumulation in the media for EGF-free media, with the presence of 20µg/ml of the 225 EGFR-blocking antibody (red squares, labeled +Ab) and without the antibody (blue diamonds, labeled Controls,). The detection limit of the ELISA is indicated by the dashed green line. All of the controls, as well as the 8hr time-point were below the detection limit. With the presence of the antibody there was a linear trend of accumulation (linear fit), however the large error bars (standard deviation of the means for the three experiment) and the proximity of the values to the detection limit suggest that only a small amount of EGF enters the underlying reservoir.

The large error bars, which represent the standard deviation of the means for three identical experiments, coupled with the proximity of all of the values to the ELISA detection limit (with the 8hr+Ab time-point being below the limit) indicate that only a

small amount of EGF appears in the underlying media reservoir. Thus, there is a much smaller rate of accumulation of EGF compared to TGF-alpha (see Fig. 4.5).

For the case when Full media was used (i.e. media containing EGF), the cells were in essence given a bolus of EGF, since the concentration of EGF in the Full media was 135 pg/ml, orders of magnitude higher that what the cells normally produce (see Fig. 4.7). Thus, we expect the cells to remove the EGF from the Full media over time. This effect is shown in Fig. 4.8, where the controls represent the basal EGF removal, and with the presence of antibody, the rate of consumption is decreased due to the decreased amount of binding sites on the receptors. The results indicate that the removal rate of the control cells (where no antibody is added, blue diamonds in Fig. 4.8) is such that at 48 hours >75% of the initial EGF present is taken up by the cells. The presence of the 225 EGFR-blocking antibody caused a decreased rate of removal so that at 48h only 40% of the initial EGF was consumed by the cells. One potential reason why the EGFR antibody does not decrease the consumption rate to zero, as would be expected if all of the binding sites on all of the receptors were occupied by the antibody, is the presence of other receptors from the EGFR family that could take up the EGF from the Full media (Harris et al., 2003; Raab and Klagsbrun, 1997; Yarden and Sliwkowski, 2001). Since the 225 antibody is specific only to erbB-1 (usually termed EGFR, and the only one we have focused on so far), other members of the erbB family, e.g. erbB-2,3,4 all have the potential to bind EGF (Harris et al., 2003; Raab and Klagsbrun, 1997; Yarden and Sliwkowski, 2001) and thus account for the inability to completely block all of the binding sites. The results (see Fig. 4.8) also suggest that erb-1, or EGFR, is the dominant receptor for EGF binding in our NHBE cells.

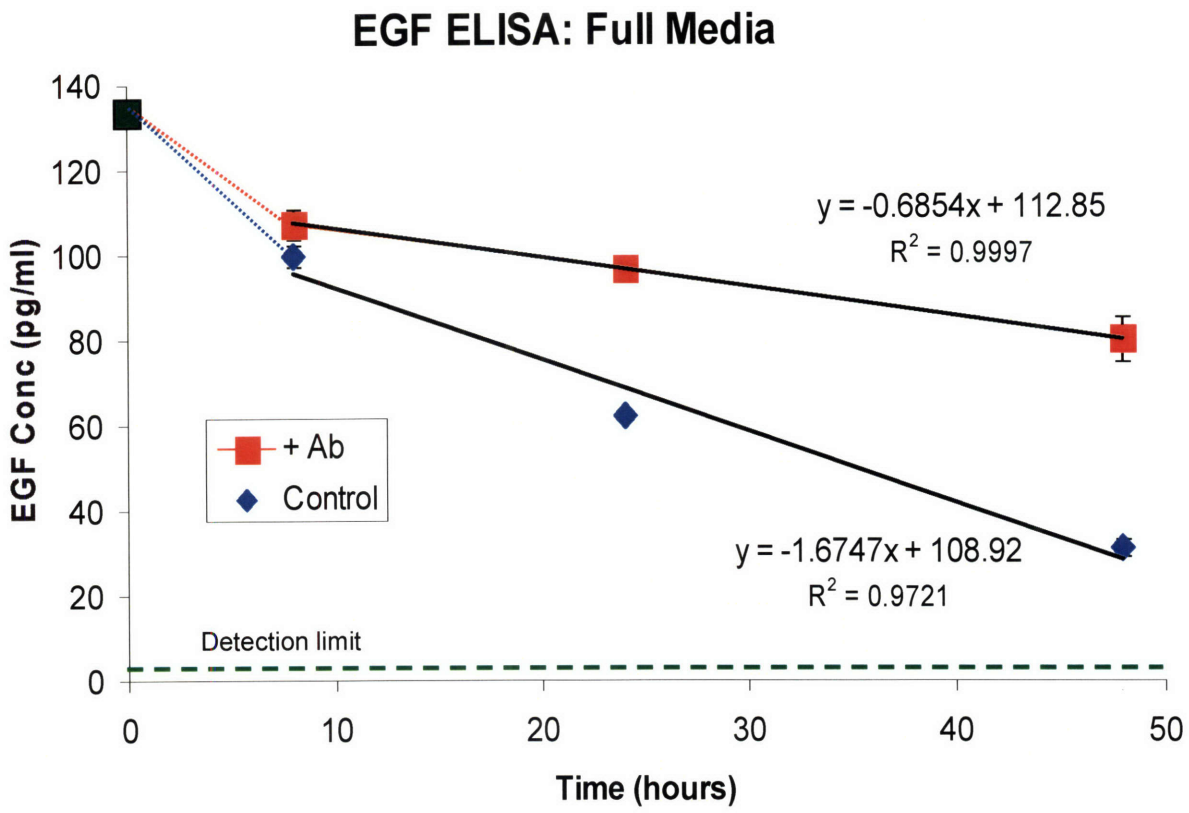

Figure 4.8 EGF uptake from the Full media. At t=0 the amount of EGF in the Full media is 135 pg/ml. Over 48 hrs the controls (blue diamonds) uptake > 75% of the EGF initially present. With the presence of 20µg/ml of the 225 EGFR-blocking antibody (red squares, labeled +Ab), the uptake rate decreases, and after 48 hr the cells have consumed only about 40% of the initial EGF. The error bars represent standard deviations of the means for three identical experiments, and the detection limit of the ELISA is shown as the dashed green line.

The last of the three EGFR ligands examined was HB-EGF. In order to analyze this ligand, an in-house ELISA was developed since there are no commercially available HB-EGF ELISA kits (unlike TGF-alpha and EGF, for which commercial kits were used).

The procedure adopted was based on the sandwich ELISA protocol of Vinante et al. (Vinante et al., 1999). The resulting standard curves for the above experiments are shown in Fig. 4.9.

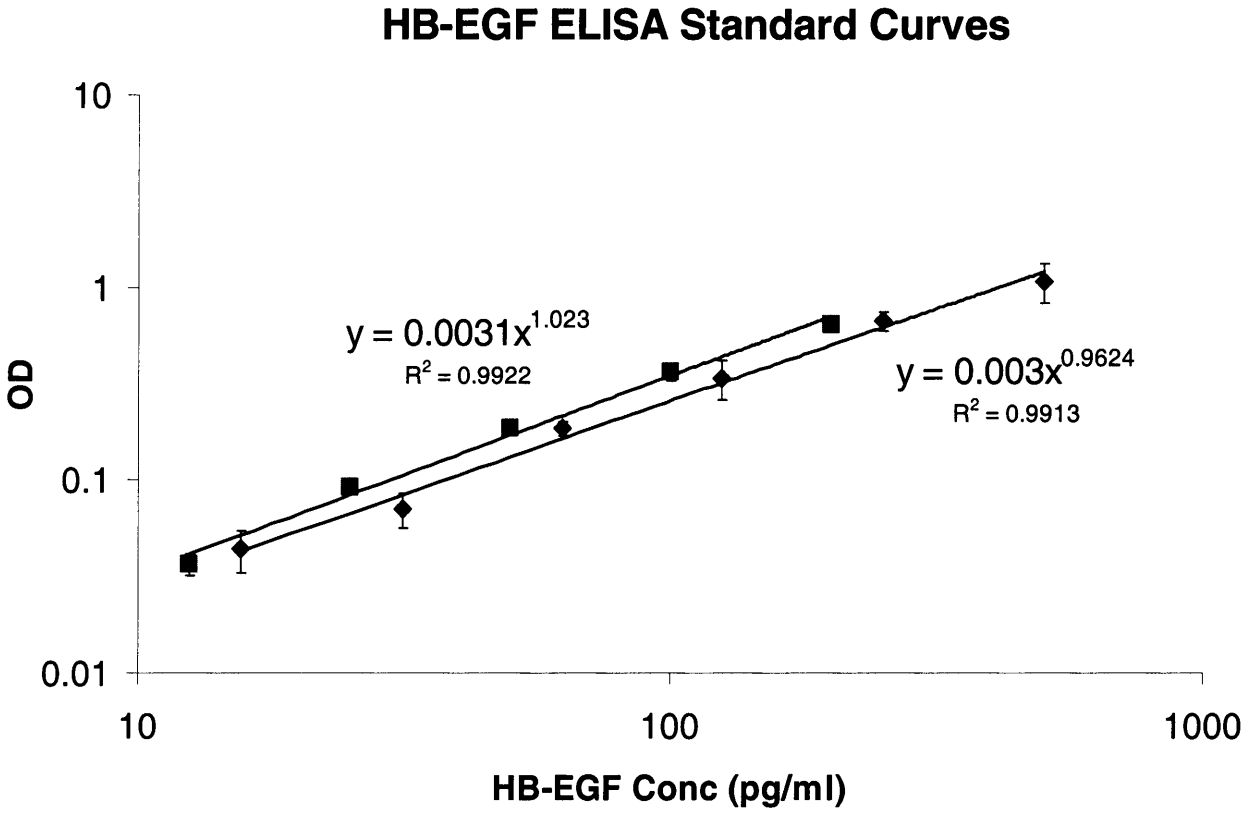

Figure 4.9 HB-EGF standard curves. The detection limit of our in-house ELISA was about 15pg/ml, near the detection limit of the commercial TGF-alpha ELISA (Fig. 4.4).

All of the samples tested from the experiments described above were below the detection limit of our HB-EGF ELISA. The detection limit of our in-house ELISA was around 15 pg/ml (approximately equal to the detection limit of the TGF-alpha commercial ELISA kit). The inability to detect HB-EGF in the concentration ranges similar to those of TGF-alpha implies that the autocrine loops of HB-EGF could be

functioning at much lower absolute concentrations than TGF-alpha. Another explanation could be the considerably higher molecular weight (about four times that of EGF or TGF-alpha) which would significantly hinder HB-EGF diffusion through the LIS (see Chapter 3) (Kovbasnjuk et al., 2000; Xia et al., 1998). In addition, HB-EGF is heavily charged and the interactions with the LIS glycocalyx could also contribute to HB-EGF being "trapped" in the LIS (Kovbasnjuk et al., 2000). Comparing TGF-alpha with EGF (see Figs. 4.5 & 4.7) we see that the EGF accumulation rate is more than an order-of-magnitude lower than TGF-alpha. This inference was based on having a very sensitive commercial ELISA kit for EGF (detection limit was 1 pg/ml). If such a sensitive ELISA was available for HB-EGF, then it may be possible to determine in what concentration range the accumulation of HB-EGF occurs.

The accumulation of ligands in the underlying media (see Fig. 4.5 & 4.7) can be used to calculate a shedding rate for the individual EGFR ligands (TGF-alpha and EGF) (DeWitt et al., 2001; Dong et al., 1999; Dong and Wiley, 2000; Lauffenburger et al., 1998; Oehrtman et al., 1998). Our basic assumption is that most of the ligand binding sites on the receptors are blocked by the 225 EGFR antibody. Then the ligand shed into the LIS should equal the ligand appearing in the underlying media reservoir. The accumulation curves give the concentration of ligand in the underlying media as a function of time (i.e. the 8, 24, and 48 hour time-points). To get a sense of how much ligand is being shed by an individual cell we must convert the ligand concentration per time into a shedding rate of molecules/cell/min (Oehrtman et al., 1998). To obtain the shedding rate in terms of molecules shed by each cell per minute, the following procedure is employed:

1. Find the slope of the fitted linear accumulation curve with the presence of antibody (e.g. top curves in Fig. 4.5 & 4.7). The slope is in pg/ml/hr.
2. Take the slope value found in 1 and convert it to molecules/cell/hr by multiplying by the

   Conversion Factor = $(g/10^{-12}pg)(mol/5500g)(6.02*10^{23}/mol)(1/avg\ cells)*(\#\ mls)$

This conversion factor transforms the total amount of ligand (picograms) into number of ligand molecules, and then divides that by the total cell number in a well to obtain a per cell average (Oehrtman et al., 1998). The total amount of ligand is obtained by multiplying the concentration (pg/ml) by the volume of the media reservoir (in our experiments this volume was 1ml). Determining the number of molecules from picograms involves dividing by the molecular weight of the ligand (for both EGF and TGF-alpha MW=5500 g/mol) and multiplying the result by Avogadro's number ($6.02*10^{23}$ molecules/mol) (Oehrtman et al., 1998).

In accordance with step 1. the TGF-alpha and EGF slopes for the EGF-free media + Ab curves were 1.5209 and 0.0571 pg/ml/hr, respectively (upper curves, Figs. 4.5 & 4.7). The conversion factor in 2. for both ligands (having approximately equal molecular weights) is thus:

$$\text{Conversion Factor} = (10^{-12})*(1/5500)*(6.02*10^{23})*(1/700000)*1 \qquad (1)$$

$$= 15.64\ (\text{molecules/cell})*(\text{ml/pg})$$

Here the total number of cells per well was estimated (based on previous measurements) as 700,000 and the volume of the media reservoir was 1ml. Multiplying the conversion factor by the slope of the accumulation curves yields:

TGF-alpha shedding rate = 15.64 (molecules/cell)*(ml/pg) * 1.5209 (pg/ml/hr) (2)

= 24 molecules/cell/hour

EGF shedding rate = 15.64 (molecules/cell)*(ml/pg) * 0.0571 (pg/ml/hr) (3)

= 1 molecule/cell/hour

For the cases when Full media was used, the TGF-alpha shedding rate was approximately equal to the 24 molecules/cell/hour obtained in equation (2) (see Fig. 4.5). However, when analyzing EGF ligand the EGF in the Full media was taken up by the cells (see Fig. 4.8). In analogous fashion to the shedding rate (i.e. taking the slope of the control curve in Fig. 4.8), we calculated the normal basal uptake rate of EGF to be:

EGF uptake rate (controls) = 15.64 (molecules/cell)*(ml/pg) * 1.6747 (pg/ml/hr)

= 26 molecule/cell/hour (4)

The effect of the EGFR antibody was to decrease the uptake rate (by occupying the binding sites on the receptors). Calculating the EGF uptake rate with the presence of 20μg/ml of the 225 EGFR-blocking antibody (top curve of Fig. 4.8) yielded:

EGF uptake rate (with Ab) = 15.64 (molecules/cell)*(ml/pg) * 0.6854 (pg/ml/hr)

= 11 molecule/cell/hour (5)

Thus, the presence of the EGFR antibody decreased the uptake rate by nearly 60%.

4.3 The effect of pressure on the shedding rate

Previously (see above and Chapter 1) we have stated that autocrine loops may exist in the LIS of NHBE cells that regulate the response to mechanical loading (Tschumperlin et al., 2004). An integral part of the loop was shedding of ligand into the LIS (see Fig. 4.1). In prior experiments we observed an increase in gene expression for both HB-EGF and EGF,

and detected no increase in TGF-alpha gene expression when pressure was applied continuously for 8 hours (Chu et al., 2005; Tschumperlin et al., 2004). Having established the basal shedding rates for both TGF-alpha and EGF, we wanted to probe the effect of pressure on the shedding rate.

The experimental protocol was similar to the one used for the determination of the basal shedding rates, except that now pressure was introduced (with and without the presence of the EGFR-antibody). Also, two (instead of the previous three) identical experiments were performed. The same 225 EGFR-blocking antibody concentration of 20μg/ml was used. A transcellular pressure gradient of 30cmH_2O was applied continuously for 8hrs. The 8 hour time-point was collected immediately after the pressure was turned off. Thus, the cells in the 24 hour well experienced 8 hours of pressure followed by 16 hours of no pressure, and similarly for the 48 hour time-point (8hrs of pressure followed by 40hrs of no pressure). The ligand accumulation curves for TGF-alpha for all four conditions (control, antibody only, pressure only, and pressure+antibody) are shown in Figure 4.10. The standard curve (omitted here for clarity) had a detection limit of 7.5 pg/ml. The same analysis as for the basal shedding case (see equation (1)) was performed to convert accumulation rates to shedding rates of molecules/cell/min. For the case when no pressure was applied the measured shedding rate was 22 molecules/cell/hour, very close to the value of 24 molecules/cell/hour previously obtained for the identical experiment (see Fig. 4.5 and equation (3)). The effect of pressure was to increase the shedding rate to 31 molecules/cell/hour (see Fig. 4.10). This increase in TGF-alpha shedding rate of almost 50% occurs after more than 8 hours (no difference between pressure and no-pressure at 8h, see Fig. 4.10) indicating

that mechano-induction of TGF-alpha shedding is a slow process unlikely to contribute to proximal mechano-responses.

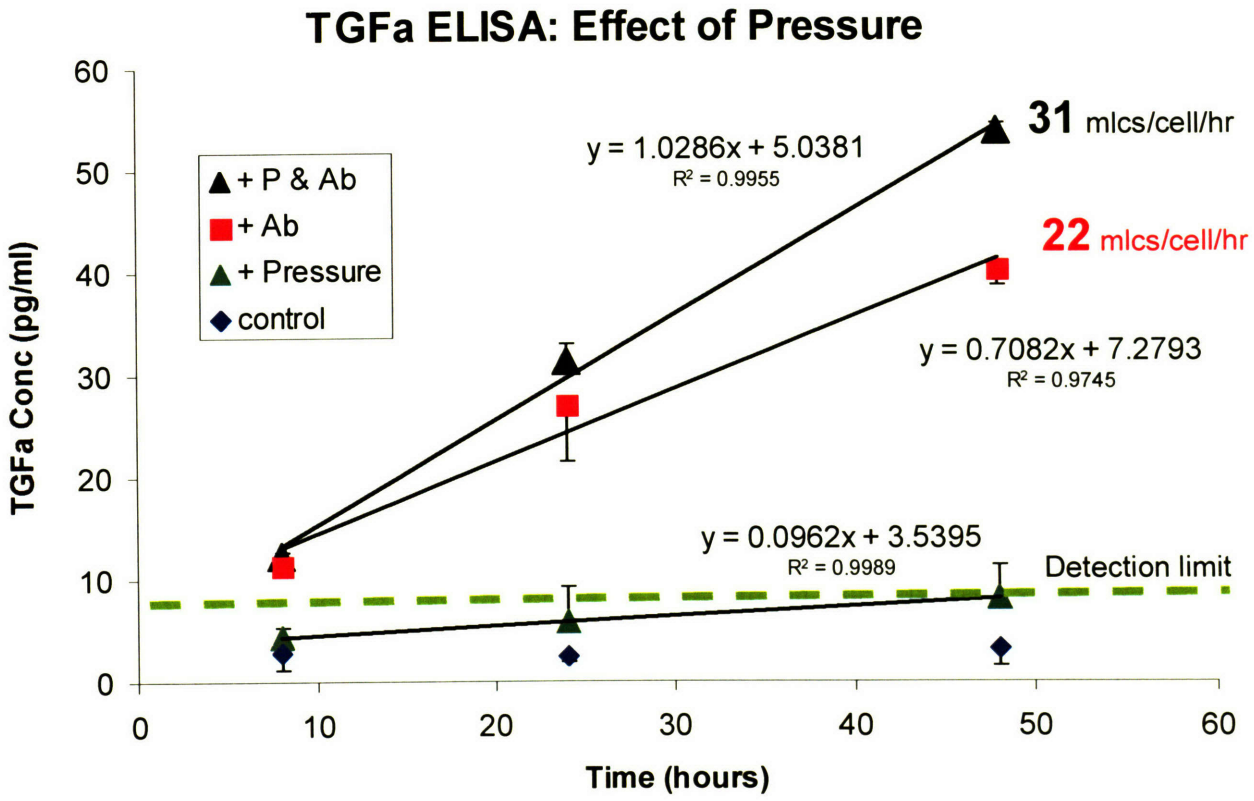

Figure 4.10 TGF-alpha accumulation in the underlying media reservoir for 4 cases: controls (blue diamonds, labeled control), 8hrs of continuous pressure, where t=8h was collected immediately after the pressure was turned off (dark green triangles, labeled +pressure), presence of 20μg/ml of the 225 EGFR-blocking antibody (red squares, labeled +Ab), and pressure+20μg/ml of 225 antibody (black triangles, top curve, labeled +P & Ab). The shedding rates for the antibody and pressure+antibody case are drawn next to the corresponding curves. The detection limit of the TGF-alpha ELISA was 7.5

pg/ml (dashed green line). Error bars indicate standard deviations of the means for two identical experiments.

In this chapter we presented measurements of shedding rates for three EGFR ligands (TGF-alpha, EGF, and HB-EGF) first under basal and then after application of a 30cmH_2O transcellular pressure gradient for 8 hours. For TGF-alpha the shedding rate under basal conditions was about 22 molecules/cell/hour, while for other two ligands the shedding rates were either close to detection limit (EGF rate of about 1 molecule/cell/hour) or below the ELISA detection limit (HB-EGF). After application of 8 hours of pressure, the only detectable shedding rate was for TGF-alpha, being 31 molecules/cell/hour (an almost 50% increase from the basal rate).

Next, we further explore the effect of pressure on our cultured NHBE cells, focusing on capturing real-time images of the collapse in LIS geometry. In subsequent chapters we relate these results to our mechanotransduction model described in Chapter 3.

5. Real-time measurement of pressure-induced LIS collapse

5.1 Introduction

In previous chapters (see Chapter 3) we examined the parameter space of the diffusion-convection equation, and identified the rate of LIS collapse as one of the crucial factors affecting LIS ligand dynamics. Our numerical model enabled us to examine how in a rapidly collapsing LIS the ligand concentration changes were substantially different than in a LIS that collapsed over a longer period of time. The resulting concentration profiles were different in both shape and character, thus prompting further investigation of the exact LIS collapse dynamics. In the preceding chapters the amount of LIS collapse was based on the prior experiments using a two-photon imaging microscope that allowed a temporal resolution on the order of several minutes (Tschumperlin et al., 2004). Therefore, the images obtained could not capture the essential LIS collapse dynamics which likely occurred on a shorter time scale (on the order of a minute or less). The previous two-photon setup did give valuable information about the final, post-collapse LIS geometry, but fell short of capturing of how fast this final state was reached. Since the dynamics of the LIS collapse can have profound effects on the LIS ligand concentration (and the entire mechanotransduction process) we set out to measure, with better time resolution, how the LIS geometry changes during (and after) a pressure-induced collapse. In this chapter, we present how the LIS collapse was measured and in the following chapter we explain the image postprocessing algorithm that enabled the quantification of LIS collapse. The experimental and quantitative results (see next chapter) based on the techniques described this chapter were used as direct input into numerical models presented in the last chapter.

5.2 The high-speed two-photon microscope (HSTPM)

To image the dynamics of the LIS collapse in real-time a modality with three-dimensional imaging capability and high speed was necessary. For this purpose, in collaboration with Dr. Euiheon Chung from the MIT lab of Prof. Peter So, a custom-built high-speed two-photon microscope (HSTPM) (Kim et al., 1999) was used (see Fig. 5.1). Here we present a brief technical description of the HSTPM used in all of the subsequent imaging experiments.

The HSTPM was originally developed for deep tissue imaging (Kim et al., 1999). The imaging speed was enhanced by increasing the scanning speed using a polygonal mirror scanner that was significantly faster than the conventional, galvanometer-driven scanner by about 40 times. The specimen was raster scanned with a single excitation focus and photons were collected using non-spatially resolved detectors, such as photomultiplier tubes (PMT) (see Fig. 5.1).

The excitation light source used was a femtosecond Ti:Sapphire laser (Mira 900, Coherent, Palo Alto, CA) which induced two-photon fluorescence. The microscope system was optimized for the excitation wavelength in the range between 700 and 900 nm. To excite fluorescein isothiocyanate (FITC) dextran, the excitation wavelength of 780 nm was used.

The laser beam was rapidly raster scanned across a sample plane by means of two different scanners. A fast rotating polygonal mirror (Lincoln Laser, Phoenix, AZ) accomplishes high-speed line scanning along x-axis and a slower galvanometer-driven scanner with 500 Hz bandwidth (Cambridge Technology, Cambridge, MA) correspondingly deflects the line-scanning beam along the sample's y-axis. The spinning

disc of the polygonal mirror was composed of 50 aluminum-coated facets arranged contiguously around the perimeter of the disc. The facets repetitively deflect the laser beam over a specific angular range and correspondingly scan a line 50 times per revolution. To achieve imaging speeds of 10 frames per second, a rotation speed of 3750 rpm was selected and this corresponds to the line scan speed of 320μs/line. An independent laser diode (1mW at 632 nm, Thorlabs, Newton, NJ) along with a photodiode detector (Thorlabs) was used to encode the polygonal mirror position and to generate a reference signal. This signal was then used by a high-speed data acquisition circuit (see the data acquisition part below) to synchronize the xy-scanners, the objective translator, and PMT detection circuitry.

The optical setup was designed so that the laser beam was coupled into an upright microscope (Axioscope, Zeiss, Thornwood, NY) by means of a modified epiluminescence light path. The beam was reflected by the dichroic mirror toward the objective and was focused on the specimen. To perform 3D volume scans, the objective was mounted on a computer-controlled piezoelectric objective translator (P-722.00, Physik Instrumente, Waldbronn, Germany). In the z-axis (perpendicular to the plane of imaging), the maximum travel range was 200μm. The axial translation of the objective along the z-axis yielded z-stacks of xy-plane images. The induced fluorescence signal was collected by the same objective and passed through the dichroic mirror. Residual scattered light was removed by an additional barrier filter (SP700, Chroma Technology, Brattleboro, VT). The fluorescence was recorded by a high-sensitivity PMT (R3896, Hamamatsu, Bridgewater, NJ).

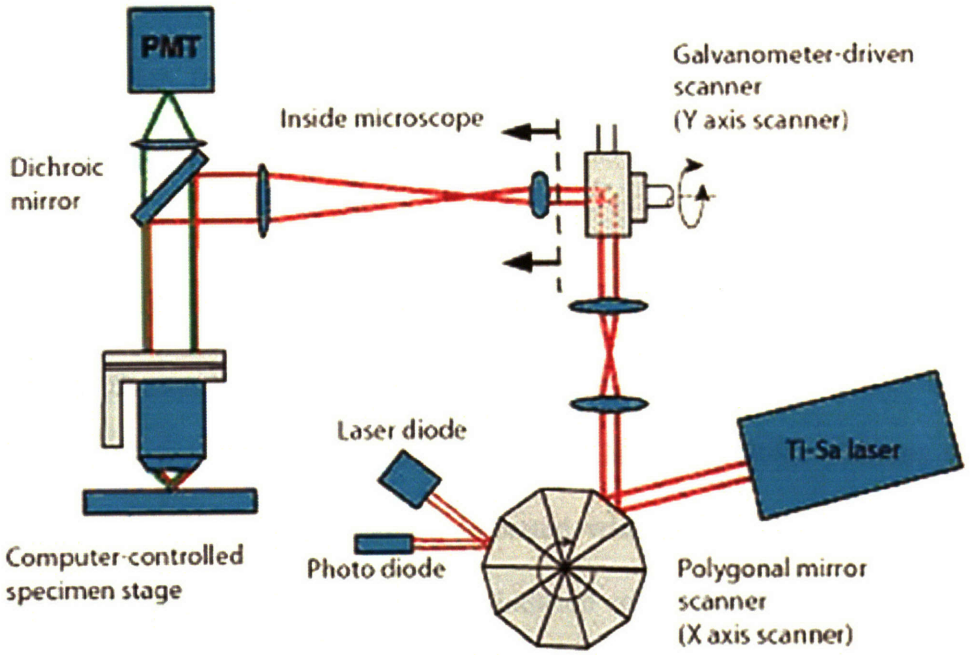

Figure 5.1 Schematic of the high-speed two-photon microscope (HSTPM) used for real-time imaging of live cultured normal human bronchial epithelial cells (Kim et al., 1999).

To image the LIS in real-time an image transfer rate of 10 frames per second was used. For a given time-point, a typical z-stack involved about 30-40 individual images, meaning that the total acquisition time for one time-point was about 3-4 seconds. The current signal from the PMT was converted to a voltage signal using a transimpedance circuit with an impedance of 323 Ohms and was further stabilized by using common mode which tended to eliminate the common electric noise to both the signal and ground line. The voltage signal was measured using a 16-bit AD converter (NI 6251, National Instruments Corp., Austin, TX) which has a speed of up to 1.25 mega samples per second. The signal was then transferred to the computer memory through the PCI bus. Images were generated by integrating the signal synchronized with the raster-scanning pattern. The field of view was approximately 300 x 400 pixels (initially we used 256x256 pixels),

which for our 63X objective (Achroplan, 63X/0.9W, Zeiss) translated into about 80 μm X 95μm (75x75 μm for 256x256 pixels) Typically, to avoid excitation saturation of chromophores, the average laser power incident upon the specimen was below 250mW.

5.3 High speed two-photon imaging of the LIS collapse

To observe the dynamics of the LIS collapse, we employed a custom-built high-speed two-photon microscope (HSTPM) described above (Kim et al., 1999). Working with Dr. Euiheon Chung, a custom stage was incorporated with the HSTPM that enabled the viewing of live NHBE cells during a pressure-induced collapse of extracellular geometry. The stage was setup so that the upright microscope objective would be immersed in the basal media reservoir. This meant that the cells had to be inverted (basal side on top, apical side on bottom) in order to have the objective within the working distance (see Fig 5.2). The modified imaging setup (see Fig. 5.2) also included a pressure source, similar to our initial *in vitro* pressure device (see Chapter 1). The pressure source was connected via a tube going through the plug to the apical side of the cells. All of the experiments were performed at room temperature, and the pressure source supplied compressed air containing 5% CO_2. To mark the extracellular space, a fluorescent FITC-dextran marker was used. The size of the FITC-dextran, either 70 or 150kDa, was chosen in order to minimize cellular uptake and degradation, which was seen to occur with lower molecular weights (e.g. 10 or 20kDa). The use of a high molecular weight dextran meant that the diffusion of a 70 or 150kDa molecule from the basal media reservoir into the LIS was not instantaneous. In fact, we observed that several minutes were required for the high

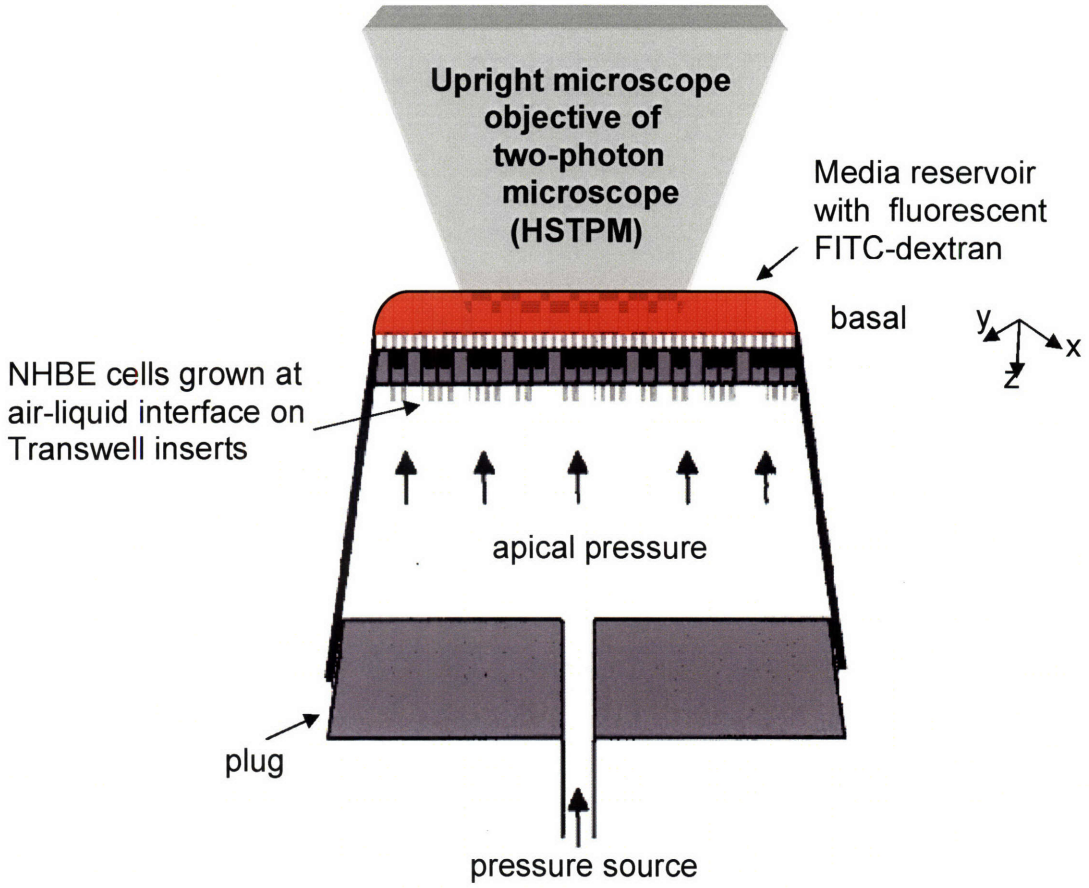

Figure 5.2 Schematic of the specimen setup for high-speed imaging of live, cultured human bronchial epithelial cells. Since the HSTPM uses an upright objective, the transwell with the cells had to be inverted. The pressure source provided pneumatic pressure via a tube going through the plug on the apical side of the cells. Typically, $30mH_2O$ of pressure was used. The area of the bottom of the transwell was about $0.33cm^2$. To cover this area around 100μL of media containing fluorescent FITC-dextran (labeled with orange color) was used. The fluorescent dextran diffused from the media reservoir into the LIS of the cells (bounded by tight junctions apically). For convenience, we here define the z-axis as the baso-apical depth axis, and the x and y axes as the corresponding planar axes.

molecular weight dextran to diffuse into the LIS and equilibrate with the concentration in the underlying media reservoir. This diffusion time can also be approximated by examining the characteristic time for a dextran molecule to traverse the entire length of the LIS:

$$t_{diffusion} \propto \frac{h_{LIS}^2}{D_{dextran}} = \frac{(15\mu m)^2}{10\frac{\mu m^2}{s}} = 25s \qquad (1)$$

Here we have assumed a LIS height h of 15 microns and a diffusion coefficient D for a high molecular weight dextran to be $10\mu m^2/s$ (Kovbasnjuk et al., 2000) (see Chapter 3). Thus, the observed equilibration time on the order of a minute (i.e. several characteristic diffusion times) was as expected, based on the simple analysis of equation (1). To ensure a sufficiently long equilibration time, we waited for about 5 minutes after applying the FITC-dextran dye.

The first set of experiments involved placing $100\mu L$ of 70kDa FITC-dextran at a concentration of 8mg/mL ($114\mu M$) on the basal side of the transwell (see Fig. 5.2). The conversion from mass to molar concentration was done based on the following formula:

1 mM = (Molecular weight in kDa) mg/mL (2)

In our case, substituting 70 kDa and 8mg/mL, the molar concentration was determined to be:

C_{molar} = (8/70) mM = 0.114mM = $114\mu M$ (3)

After the LIS equilibrated at this concentration with the underlying media reservoir images were taken using the HSTPM (see Fig. 5.3). A single planar image shown in Fig. 5.3 reveals that the area of the extracellular (LIS) space was small compared to the area occupied by the cells. Furthermore, the entire picture was not

uniform, i.e. some areas were more out of focus and less bright (these issues were addressed with postprocessing techniques, discussed in more detail in the next chapter).

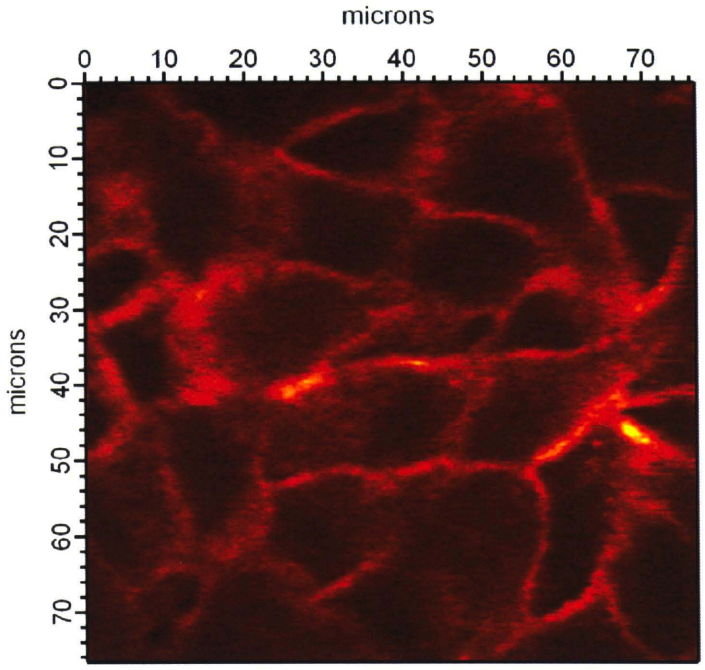

Figure 5.3 A planar (x-y) image, captured from the HSTPM, of live normal human bronchial epithelial (NHBE) cells with fluorescent FITC-dextran (orange) in the LIS. No pressure was applied.

The image of Fig. 5.3 was chosen as representative from a larger stack of about 30 planar images that were 1 micron apart in the z-direction (see Fig. 5.4). The acquisition speed of the HSTPM was 10 frames per second (i.e. the planar x-y image in Fig. 5.3 was obtained in 0.1s), which meant that the entire stack was collected in 3 seconds. This fast speed (on the order of a second) justified what we termed as real-time imaging of live NHBE cells.

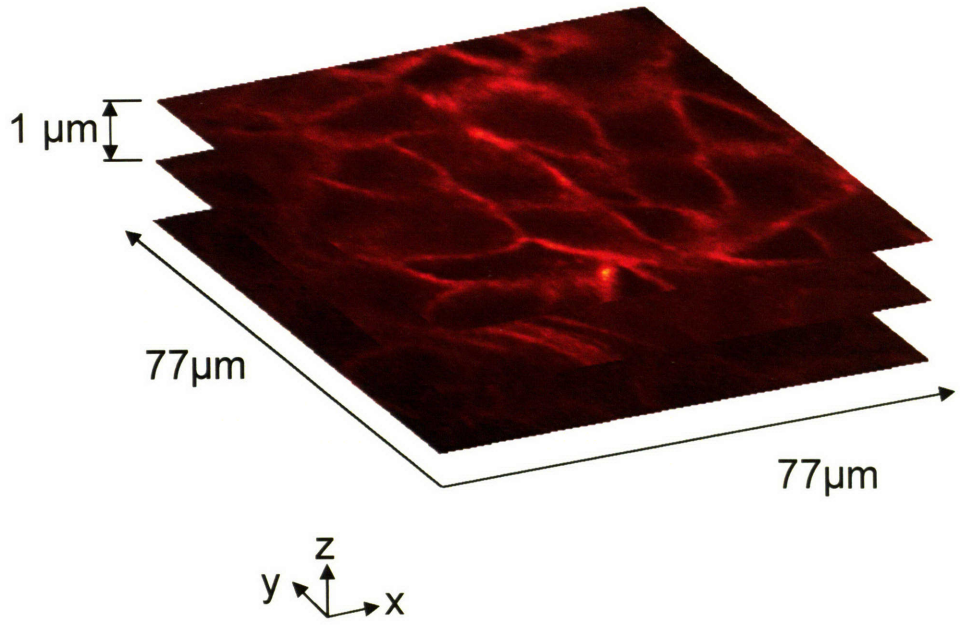

Figure 5.4 A stack of 3 representative planar (x-y) images. The individual planar images were spaced 1 micron apart along the z-axis. A complete stack contained about 30 planar images to ensure the entire LIS space was sampled. The top layer in the stack is the planar image shown in Fig. 5.3.

The above stack of images was processed to obtain a 3-D reconstruction of the LIS (see Fig. 5.5). In the reconstructed 3-D image, the top layer was the media reservoir with the fluorescent dextran, which meant that the cells were inverted (see setup in Fig. 5.2). A piece of the 3-D image was cut out to reveal the geometrical structure of the LIS (see vertical bright lines in Fig. 5.5). The 3-D render was composed based on a stack of 30 planar images, and thus the total height was 30 microns.

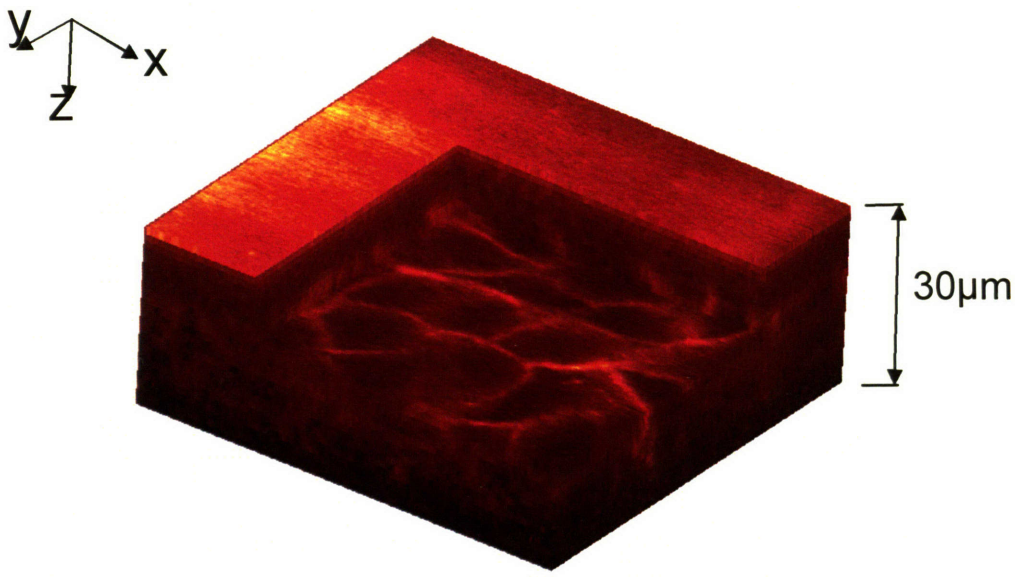

Figure 5.5 3-D reconstruction based on 30 planar images. To reveal the architecture in the z-direction (vertical orange lines) a section of the image was cut out. The media reservoir with the FITC-dextran is the top surface. The exposed planar section is the planar image of Fig. 5.1. The total height in the z-direction was 30 microns.

For further insight into the LIS architecture, we reconstructed the planar stack of Figs. 5.4&5.5 to obtain a view in the y-z plane (see Fig. 5.6). This y-z plane is perpendicular to the imaging plane (x-y, see Figs 5.3-5). In our previous models of mechanotransduction in the LIS (see Chapters 2&3), we assumed that 1-D diffusion and convection occurred in this plane. The white line in Fig. 5.6 indicates the plane where the image of Fig. 5.3 was taken.

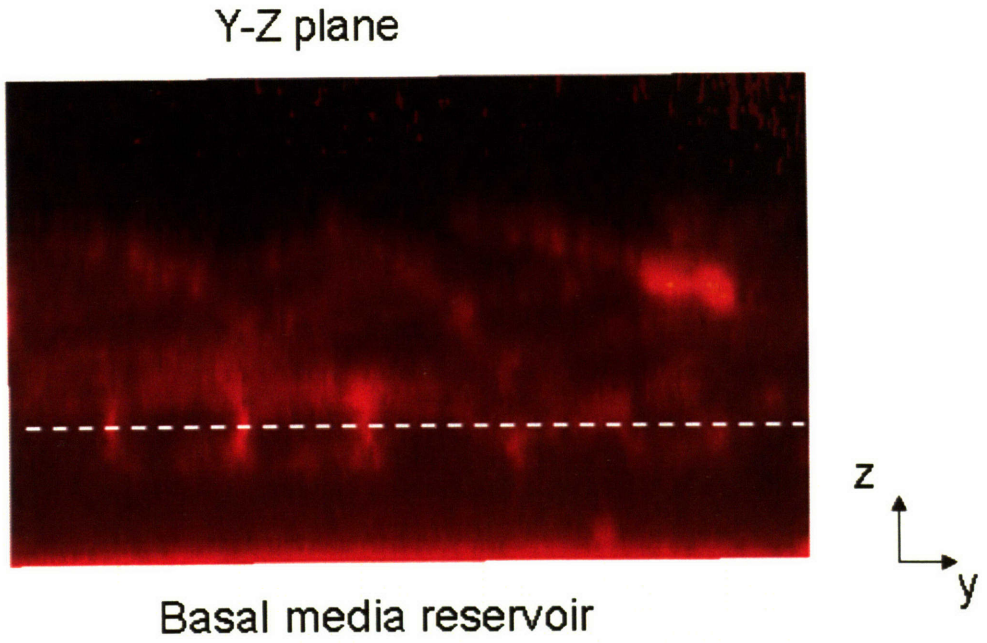

Figure 5.6 Reconstructed image in the y-z plane for the stack shown in Fig. 5.5. The dashed white line represents the plane of the image of Fig. 5.3. This, y-z plane image was rotated so that the basal media reservoir was on the bottom. The individual LIS regions are labeled in orange. The unlabeled space between the media reservoir and the appearance of the cells represents the thickness of the Transwell porous membrane upon which the cells are cultured (the measured membrane thickness was about 8 microns, in accordance with the manufacturer's specification of 4-8 microns).

In order to see if labeling the extracellular space with dextran (as was done in all of the images above) gave an appropriate representation of the LIS, we performed a double-staining experiment, where the inside of the cell was labeled with one tracer, while the outside (extracellular) space was labeled with another tracer that had different fluorescence excitation and emission characteristics. For the intracellular tracer we used CellTracker Green (Molecular Probes Invitrogen, Eugene, OR), while for the

extracellular LIS space a 70kDa TexasRed dextran (Molecular Probes Invitrogen, Eugene, OR) was employed. Therefore, the inside of the cell gave a green signal, while the outside gave a red signal (see Fig. 5.7)

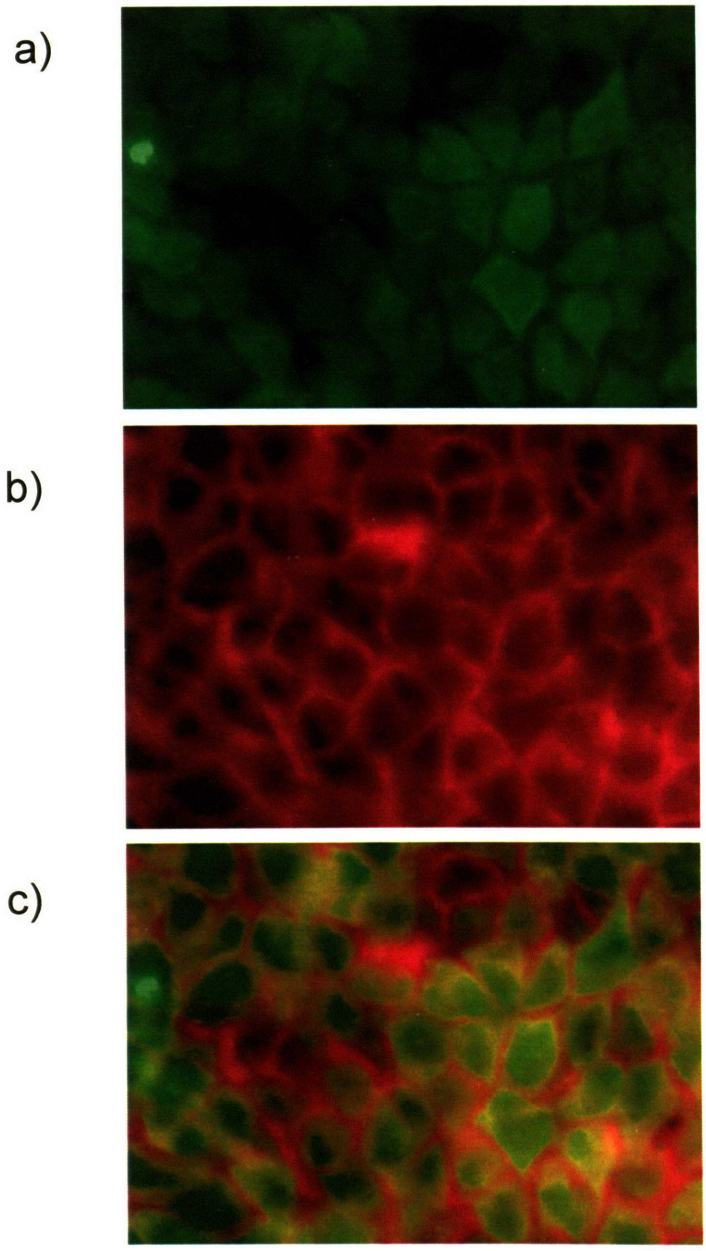

Figure 5.7 **a)** Intracellular space marked with CellTracker Green. **b)** Extracellular LIS space labeled with 70kDa TexasRed dextran. **c)** Combined image of a) & b).

As indicated by Fig. 5.7c, the extracellular marker roughly corresponds to the space outlined by the edge of the cell. However, there are some minor differences that could be due to incomplete labeling of the intracellular tracer (see Fig. 5.7a) and cellular uptake of some of the extracellular tracer (see Fig. 5.7b).

With all of the imaging methodology and hardware in place for normal, basal conditions, we then proceeded to imaging of the collapse of the LIS during the application of 30cmH_2O of pressure. The initial pre-pressure time-point, i.e. t=0, is shown in Fig. 5.3. Immediately after t=0, a transcellular pressure gradient of 30cmH_2O was established and maintained for 10min. During this period, stacks of images were acquired at: t = 20, 120, 300, and 600s (see Fig. 5.8). For clarity, we show in Fig. 5.8 three planar images (t = 20,120, and 600s) corresponding to the initial, t=0 image. From the figure, looking at the thickness of an individual LIS, it is apparent that the LIS width decreases (i.e. the labeled orange lines on the image become thinner as time increases). Another important observation is that most of the collapse seems to be occurring in the first few minutes. These conclusions were based on simple inspection of the images, and to obtain actual quantitative results of how the LIS collapses over time, an automated image processing algorithm was needed. In the next chapter we present such an algorithm that analyzes the images of Fig. 5.8 and automatically determines the corresponding LIS collapse curve.

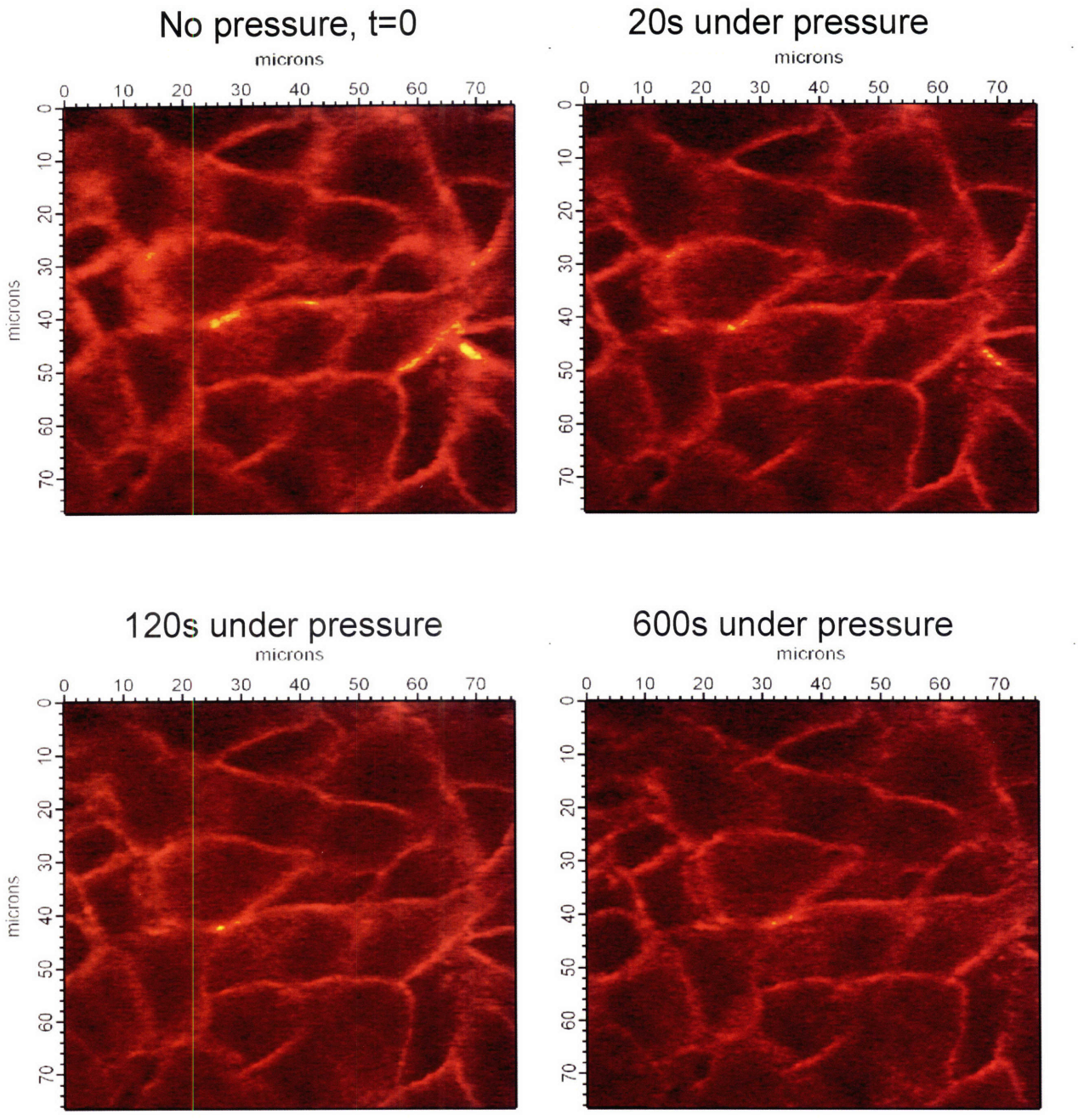

Figure 5.8 A planar image taken at t=0 (upper left corner, see also Fig. 5.3) was followed during pressure application. The cells were exposed to pressure for 10 minutes (600s). Three representative time-points are shown, t=20,120, and 600s after the onset of pressure.

The utilization of a custom-built high-speed two-photon microscope (HSTPM, described above) (Kim et al., 1999) enabled the real-time imaging of the lateral intercellular space (LIS) during a pressure-induced collapse. By taking a stack of planar images (with the imaging plane being perpendicular to the apico-basal axis) the 3-D LIS architecture could be reconstructed. The high-speed data acquisition capabilities (up to 10 frames per seconds) enabled us to obtain 30 planar images in 3 seconds. The spacing between two neighboring images in a stack was 1 micron, which meant that we could span a region of 30 microns along the apico-basal axis in a few seconds. Thus, during a pressure-induced collapse a discrete time-point was acquired in about 3 seconds. Comparing multiple time-points obtained during a 600s pressure experiment, it was apparent that individual LIS widths decreased over time. However, these conclusions were based on qualitative reasoning by simply viewing by eye the images in Fig. 5.8.

For appropriate characterization and quantification of how much the LIS collapsed we developed an image analysis algorithm specifically designed for processing of images obtained by the two-photon microscope. Since many more pressure experiments were done, under different conditions, and with finer temporal resolution, automation of the image processing tools became an essential task. The next chapter deals with the development of the image analysis algorithm and also presents results (i.e. LIS collapse curves) for various pressure experiments. These results were then used as direct inputs for our numerical models.

6. Image processing and quantification of the LIS collapse

6.1 Introduction

The procedure for obtaining real-time images of live normal human bronchial epithelial (NHBE) cells was described in the previous chapter (see Chapter 5) (Kim et al., 1999). These images were taken both before and during the application of a transcellular pressure gradient. The compliant lateral intercellular space (LIS) collapsed due to the compressive stress (see Fig. 5.8 in Chapter 5) (Tschumperlin et al., 2004). Images were taken at a number of time-points to obtain data on the dynamics of LIS collapse. Inspecting these images by eye, it was apparent that the area occupied by the LIS decreased as time under pressure progressed. However, for our modeling purposes (see Chapter 3) (Kojic et al., 2006) we need to have a precise LIS collapse curve. This means that quantification of the change in LIS area (and volume) in a defined and consistent way becomes essential. Equally important was the ability to efficiently examine many time points within a single experiment as well as to compare LIS collapse across numerous experiments. These needs required us to develop an automated algorithm that could quickly process large quantities of data. In this chapter we present the development, in collaboration with Austin Huang from MIT, of an algorithm that processes multiple stacks within a single experiment and outputs the corresponding collapse curve of the LIS, normalized to initial, t=0, pre-pressure time-point.

6.2 Image segmentation based on a flat threshold: LIS vs. intracellular space

In collaboration with Austin Huang of MIT, an image analysis protocol was designed for automating the task of measurement of the LIS volume from images. To do this, image pixels must be dichotomously labeled as either LIS or intracellular space. This is an example of a more general problem in image analysis called segmentation, which is the process of reducing the representation of an image in such a way that the reduced representation retains the image properties of interest for a particular application (Forsyth and Ponce, 2003).

An assumption was made that fluorescence intensity was correlated with concentration of the FITC-dextran marker we used for the LIS. Since marker was only present in the LIS, high intensity regions were labeled as LIS while low intensity regions were deemed background. The input to the segmentation algorithm in this case was a 2D image and the output of the segmentation algorithm was a 2D image with the same dimensions of the input, but with pixels intensities replaced by either 1, if the pixel belonged to a LIS, or 0, if the pixel was not LIS (and hence part of the intracellular space). The segmentation was applied to all images in a given experimental time series. The total LIS volume for each time point was estimated by integrating the segmented image. There are several ways to obtain a segmented image, the simplest being by using a thresholding algorithm, which labels all pixels with an intensity higher than a chosen constant - known as the threshold value - as 1 (LIS), and all pixels with an intensity lower than the threshold value as 0 (background or in our case intracellular space).

However, confounding the segmentation was the uneven illumination by the illumination source – creating intensity variations throughout the image. Thus, if we

examine a planar image (see Fig. 6.1) obtained by the high-speed two photon microscope (HSTPM, described in detail in Chapter 5) it becomes apparent that the brightness (or intensity) is non-uniform. We then wanted to evaluate just how confounding was the uneven illumination for the simple case of segmentation based on a flat threshold.

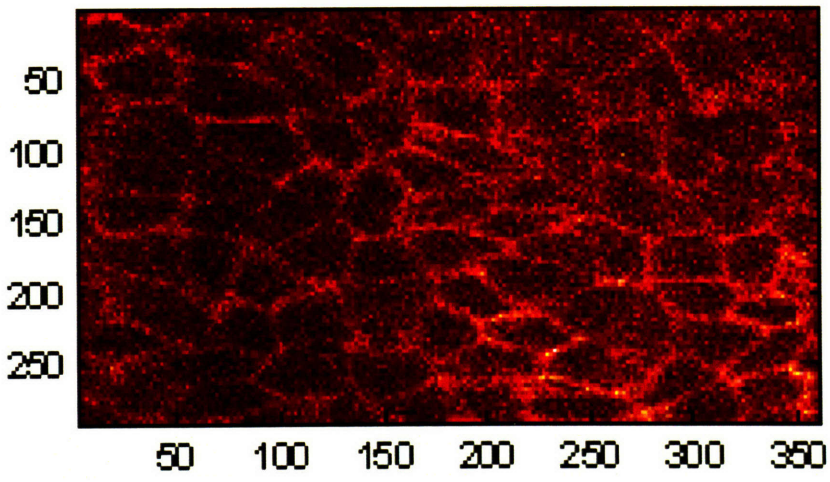

Figure 6.1 A typical planar (raw) image obtained from the high-speed two photon microscope (HSTPM, (Kim et al., 1999) see Chapter 5 for more details). The non-uniform brightness of the image was apparent going from left to right. The axis divisions indicate number of pixels.

To explore the threshold effect in detail we analyzed the image in Fig. 6.1 by choosing a range of single, flat thresholds (see Fig. 6.2) (Chow and Kaneko, 1972; Gonzalez and Woods, 2002). Since each pixel of Fig. 6.1 (same image as lower right corner of Fig. 6.2) has an associated intensity value, we decided to pick thresholds based on the mean (average) intensity value of all the pixels and the corresponding standard deviation (stdev) of the mean (see Fig. 6.2). Thus, we chose to explore the range from:

$$\textbf{threshold}_{\textbf{LOW}} = \textbf{mean} - 0.5 \times (\textbf{stdev}) \quad \rightarrow \quad \textbf{threshold}_{\textbf{HIGH}} = \textbf{mean} + 0.5 \times (\textbf{stdev}) \qquad (1)$$

going in intervals of 0.1x(stdev). In total, 11 different flat thresholds were used (see Fig. 6.2). For a given threshold a pixel was labeled LIS if its intensity was greater than the threshold value and conversely if the intensity was less than the threshold the pixel was deemed as intracellular space.

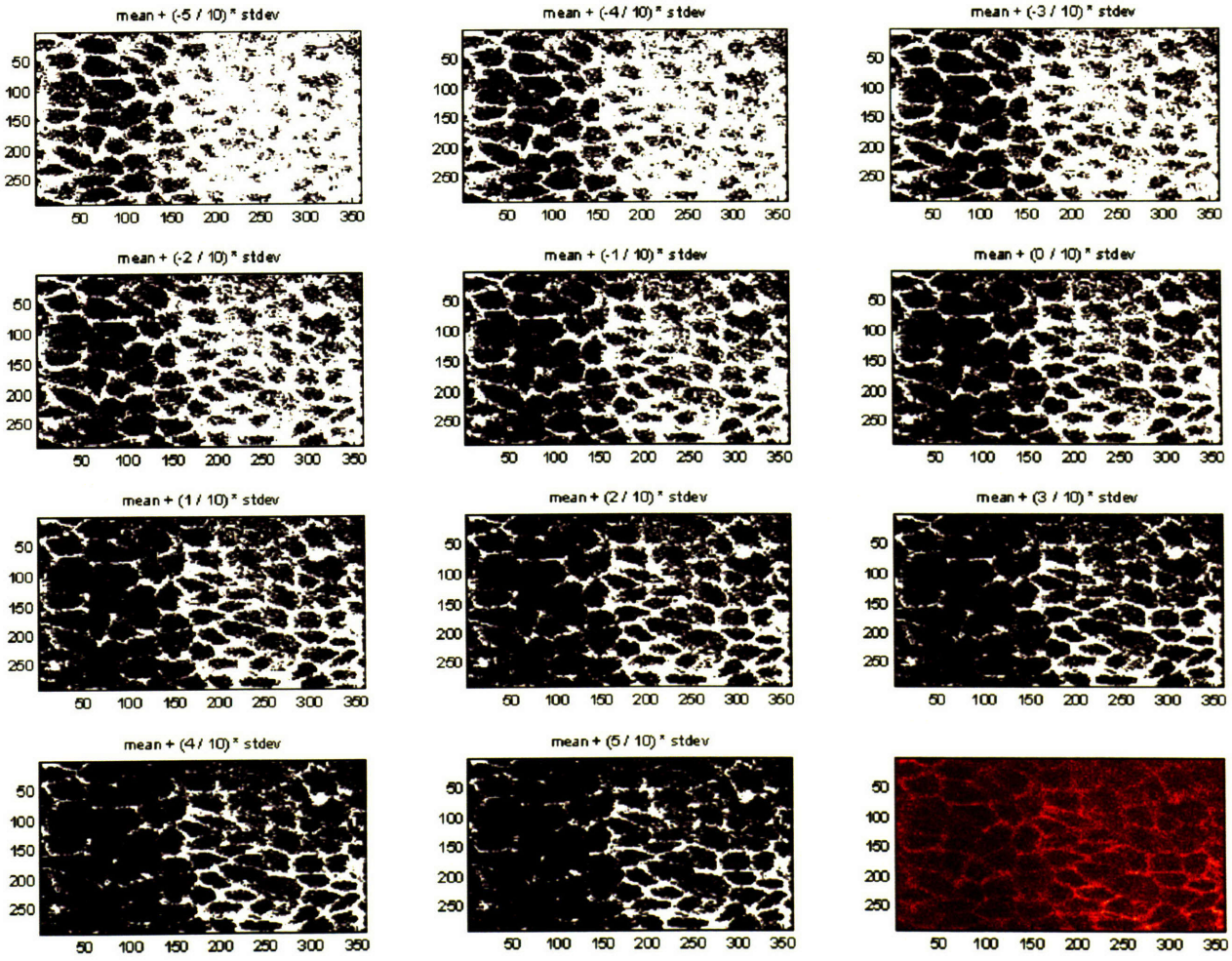

Figure 6.2 Analysis of the raw image in Fig. 6.1 (lower right corner) for a range of flat (single) thresholds. The different thresholds were chosen based on the mean (average) intensity value of the raw image and the corresponding standard deviation of the mean.

Upper left corner: threshold = mean intensity value – 0.5*(standard deviation of the mean). Second row, third column: threshold = mean intensity value of the raw image. Black and white images: white is LIS and black is intracellular space.

As Fig. 6.2 indicates, applying a low threshold (upper left corner of Fig. 6.2) resulted in correct segmentation of the low illumination region but failed to properly segment the high illumination areas. Similarly inadequate is a high threshold (bottom row of Fig. 6.2), which appropriately segments only the high illumination regions, missing almost all of the low illumination areas. An intermediate threshold also does not work, as it incorrectly segments both the high and low illumination regions. Thus, by comparing all of the images analyzed with a flat-threshold approach, we concluded that none of the analyzed images capture sufficiently well the true LIS architecture of the raw image. This meant that a different type of segmentation technique should be employed and hence, we chose an adaptive-threshold image analysis method (Gonzalez and Woods, 2002; Lee and Hayes, 2001; Ohya et al., 1994), presented next.

6.3 Image segmentation based on an adaptive threshold

Since segmentation based on a flat threshold was inadequate for capturing the LIS architecture, we developed a new algorithm that relied not on a global (one flat threshold for the entire image) but rather a local (adaptive) threshold (Gonzalez and Woods, 2002; Lee and Hayes, 2001; Ohya et al., 1994). The image processing algorithm also had several other components including a median filter and removal of small, leftover segments (Gonzalez and Woods, 2002). We first start with a raw image (see Fig. 6.3),

that was different than the image shown in Fig. 6.1 (note that we changed colors in the new raw image of Fig. 6.3 to indicate that the colors of the LIS and background are pseudocolors based on pixel intensity; we will return to the adaptive-threshold analysis of the image in Fig. 6.1 later in this chapter).

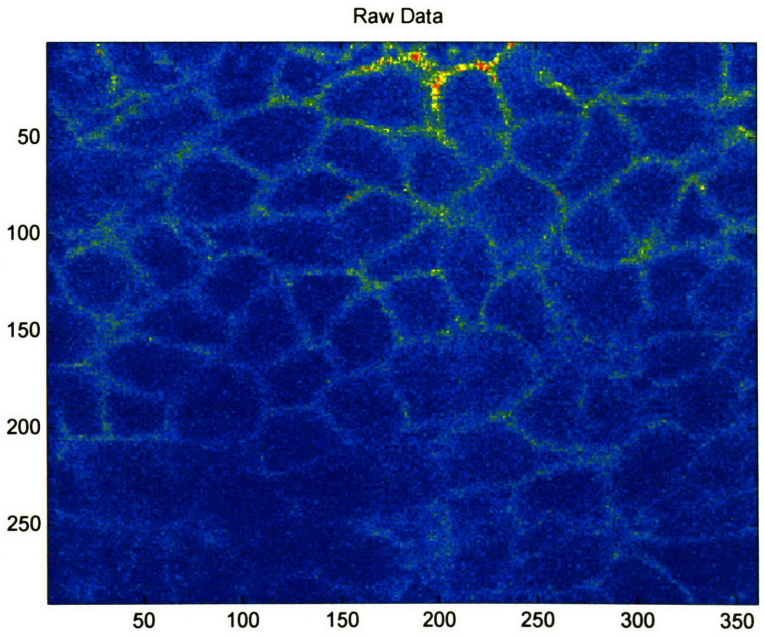

Figure 6.3 Raw, planar image used for the adaptive thresholding algorithm. Yellow and green indicates the fluorescent FITC-dextran in the LIS. The image was taken in identical fashion as the image of Fig. 6.1.; the colors were changed to indicate that both images use pseudocolors based on pixel intensity. The divisions represent the number of pixels.

The procedural steps used in the image processing algorithm were as follows:

1) Initial raw image was median filtered to remove shot (mostly single-pixel) noise.
2) Position-weighted averaging procedure (adaptive threshold) was employed to obtain a local average. A pixel was deemed LIS if its intensity was greater than

the local average by some offset value (chosen as a multiple of the standard deviation of the mean for all of the pixels of the initial, raw image).The adaptive thresholding procedure was then repeated in four directions to ensure that there was no directional bias in determining LIS pixels.

3) The four binary images (one for each direction) obtained in step 2) were merged into one image and the resulting; combined image was median filtered to remove shot noise leftover from the segmentation.

4) Isolated islands of LIS regions smaller than a prescribed size were removed.

These steps are reviewed in detail below.

Step 1). Examining the image in Fig. 6.3 it is apparent that there were a lot of small, bright specs in the background that contributed to the granulated appearance. These specs (usually corresponding to a single pixel) were termed shot noise. To remove this shot noise we used a simple median filter whose output is determined by evaluating the median value of three neighboring pixels (see Fig. 6.4). Specifically, for a given pixel, the filter looks at the two neighboring pixels (one on each side of the pixel of interest) and then assigns the median value of all three to the pixel of interest. In the simple example of Fig. 6.4, we demonstrate this procedure on two different pixels (labeled 2 and 5). For pixel 2, the median (M2) was assigned as the new intensity, where M2=median(1,2,3). In this case, the new intensity of pixel 2 (i.e. M2) was equal to the previous, raw intensity and hence there was no change. However, for pixel 5 the new assigned value of M5=median(4,5,6) was lower than the initial, raw intensity and thus the net effect was to remove this single pixel jump in intensity, representing the shot noise seen in Fig. 6.3.

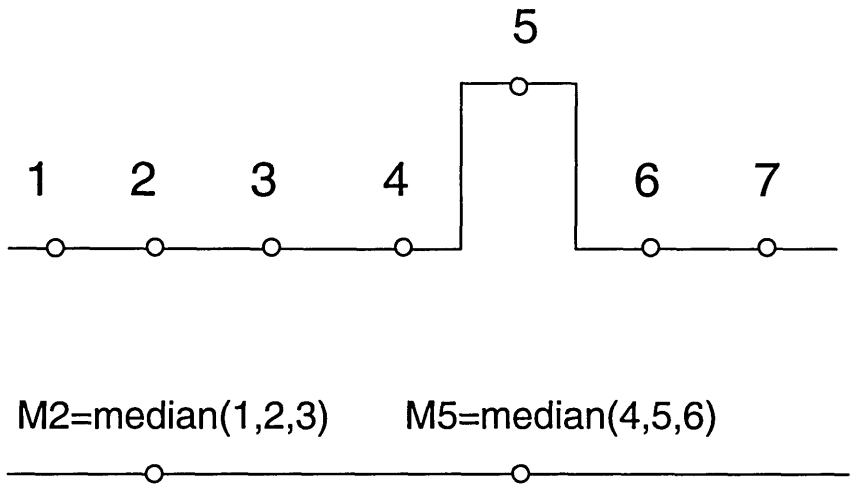

Figure 6.4 Schematic of the three-point median filter used in step 1). There are seven points corresponding to seven pixels, i.e. seven intensity values. For each pixel the median of itself and the two neighboring pixel (one on each side) was assigned as the new intensity. For pixel 2, this new intensity was the median of the first three pixel intensities: M2=median(1,2,3). In this case there was no change. However, for pixel 5 the new intensity was the median M5 of pixels 4,5,6 which meant that point 5 was now changed and given a new intensity value equal to that of points 4 and 6.

When the three-point median filter of step 1) was applied to the entire image, a new median-filtered image was obtained (see Fig. 6.5). This processed image had much less shot noise when compared to initial raw image. The new image thus appeared much less granulated and as such was suitable input for the next, key step in the image processing algorithm: adaptive thresholding (Chow and Kaneko, 1972; Gonzalez and Woods, 2002; Lee and Hayes, 2001; Ohya et al., 1994).

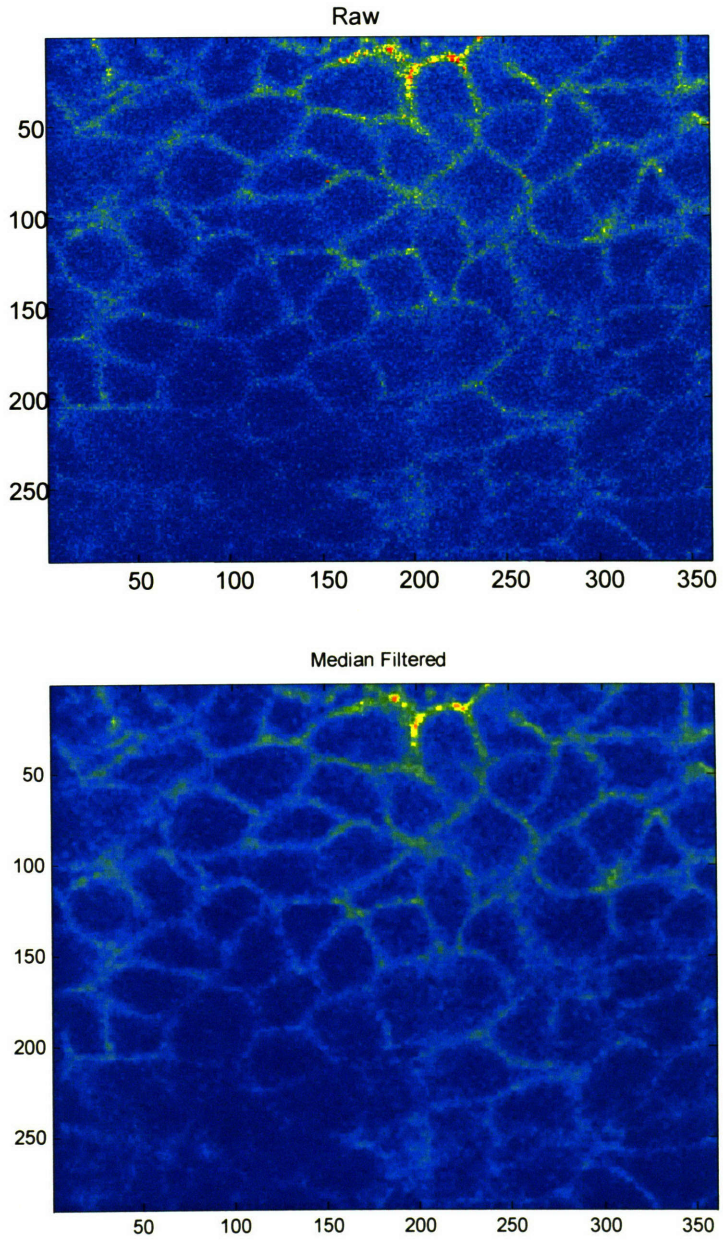

Figure 6.5 The raw image (top) was processed based on the median filtering technique of step 1) (see Fig. 6.4). The analyzed, median-filtered image (bottom) had much less shot noise than the raw image. The divisions on the axes represent the number of pixels.

Step 2) of the image analysis procedure involved determining whether a given pixel belongs to the LIS or the intracellular space. To ascertain the proper identity of a pixel, we used an adaptive thresholding approach that relied on direction-weighted averaging filters. The essential principal of the adaptive thresholding algorithm is to apply a threshold to the difference between the intensity of a pixel and an average local intensity of the surrounding pixels, rather than to the pixel intensity itself. The local average intensity for each pixel was calculated using a Gaussian weighted average of the neighboring pixels. The size of the Gaussian averaging window (in our case 30x30 pixels), was chosen to capture the characteristic size needed to detect changes in background intensities - too large an averaging window will oversmooth the changes in background intensity (i.e. the result will be similar to that of flat thresholding), while using too small an averaging window will not include sufficient background pixels to estimate the background intensity.

To illustrate how adaptive thresholding works we first examine a given pixel of interest for which we want to determine if it is LIS or not. In Fig. 6.6a, this pixel is labeled with a red X, and its position happens to be 16 (note that there are 15 pixels to the left and 15 to the right of our pixel of interest, since our averaging window was 30x30 pixels). Figure 6.6a shows the initial intensities for all of the pixels. The algorithm then multiplies these intensities with a Gaussian direction-weighted function (see Fig. 6.6b). Our pixel of interest corresponds to the highest, middle point of this function (i.e. at x=0 offset in Fig. 6.6b). The Gaussian weighting distribution is symmetrical and stretches 15 pixels to the left and right of our pixel of interest. The sum of all the 31 values of the function in Fig. 6.6b equals to 1 (hence, it is referred to as a Gaussian distribution).

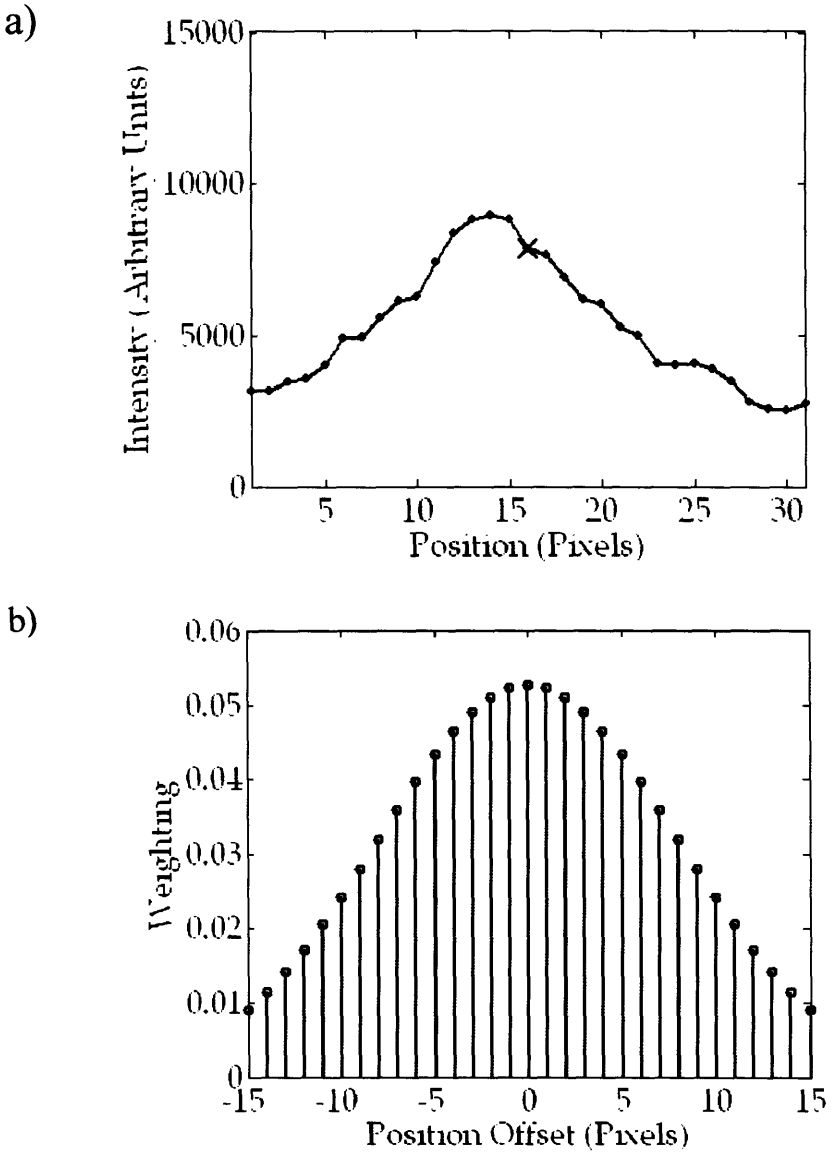

Figure 6.6 a) Initial intensities for 15 pixels to the left and 15 pixels to the right of the pixel of interest (labeled with red X, at position 16). These intensities were multiplied by the Gaussian weighted function shown in b). The pixel of interest corresponds to offset 0, and each of the 15 pixels to the left and 15 to the right of the pixel of interest had weighting values assigned to it. For each pixel, the intensity of a) was multiplied by the corresponding weighting value of b). The new, weighted intensities are shown in Fig. 6.7.

Multiplying the intensity by the corresponding weighting value yielded a new, weighted intensity for each pixel (see Fig. 6.7). As the figure indicates, these new intensities were all smaller than the initial intensities of Fig. 6.6a, since all the weighting coefficients in Fig. 6.6b were less than 1.

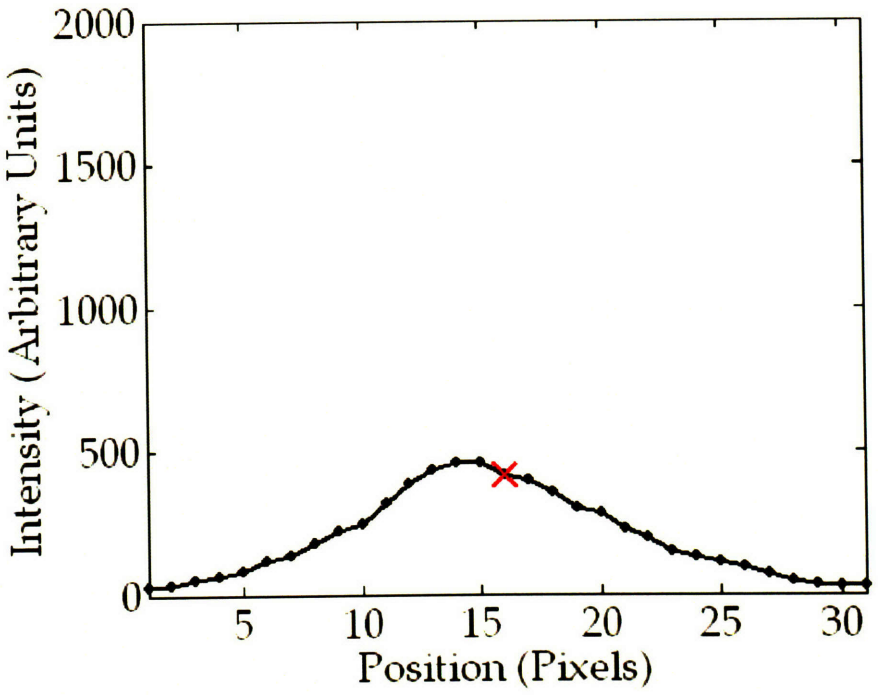

Figure 6.7 Direction-weighted intensities obtained from multiplying the intensities of Fig. 6.6a with the corresponding Gaussian weighting coefficients shown in Fig. 6.6b. The pixel of interest is labeled with a red X.

The next step in adaptive thresholding involved summing up all 31 direction-weighted intensities shown in Fig. 6.7 (each of the 31 pixels had an associated direction-weighted intensity). This yielded what we termed the local average (or local mean) for our pixel of interest. In mathematical form:

$$\textbf{local average} = \sum_{i=1}^{31} \textbf{weighted\_intensity}(i) \qquad (2)$$

Figure 6.8 displays the value of the local average for our pixel of interest (corresponding to position 16) as well as the local averages for all of the other 30 points (see blue curve), which were obtained by employing the same procedure described above.

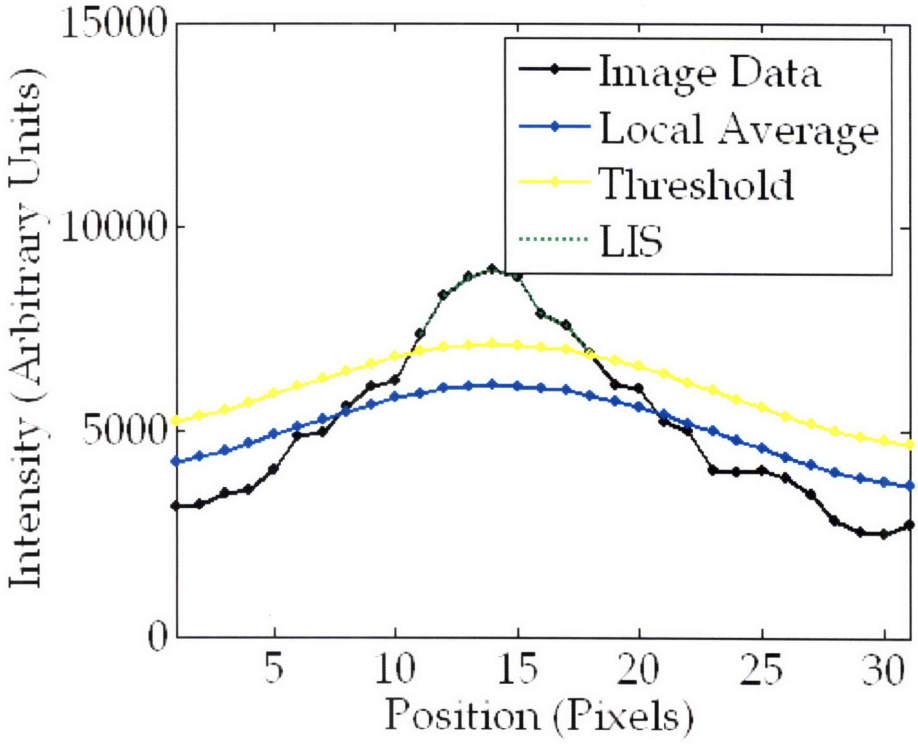

Figure 6.8 The determination of which pixels were LIS, based on the adaptive thresholding algorithm. Blue curve: local average obtained for each of the 31 pixels using equation 2 and the procedure described in Figs. 6.6 & 6.7. Yellow curve: threshold = local average + 0.3*(standard deviation of the mean for all of the pixels of the initial, raw image). Black curve: initial intensities of Fig. 6.6a that were below the threshold. Green: initial intensities of Fig. 6.6a that were higher than the threshold, and thus deemed LIS.

The threshold for LIS determination was calculated by adding to the local average the value of 0.3*(standard deviation of the mean for all of the pixels of the initial, raw image) (see yellow curve in Fig. 6.8). The standard deviation was identical to the one used in the flat threshold approach (see Section 6.2) and the effect of varying the multiple of the standard deviation (in this case 0.3) will be discussed later in this chapter. The initial intensities of Fig. 6.6a were then compared to the corresponding threshold values. If the intensity was greater than the threshold value then the pixel was deemed as LIS (see green line in Fig. 6.8), and conversely if the intensity was less than the threshold the pixel was labeled as intracellular space (see black line in Fig. 6.8).

After establishing the adaptive thresholding methodology for determining if a pixel was LIS or not, we performed the procedure on a 30x30 pixel window using Gaussian direction-weighted functions in four directions: horizontal, vertical, and two diagonal (see Fig. 6.9). In the example presented above (see Figs. 6.6-8) the neighboring 30 cells (15 to the left and 15 to the right of the pixel of interest) lied on a horizontal line. The other three directions (see Fig. 6.9) represent three more neighborhoods of pixels (around the pixel of interest, which was at the center) that were examined in order to improve segmentation of corner regions where LIS spaces intersect. For each direction a binary image was obtained (see Fig. 6.9) where each pixel was either LIS (black) or intracellular space (white).

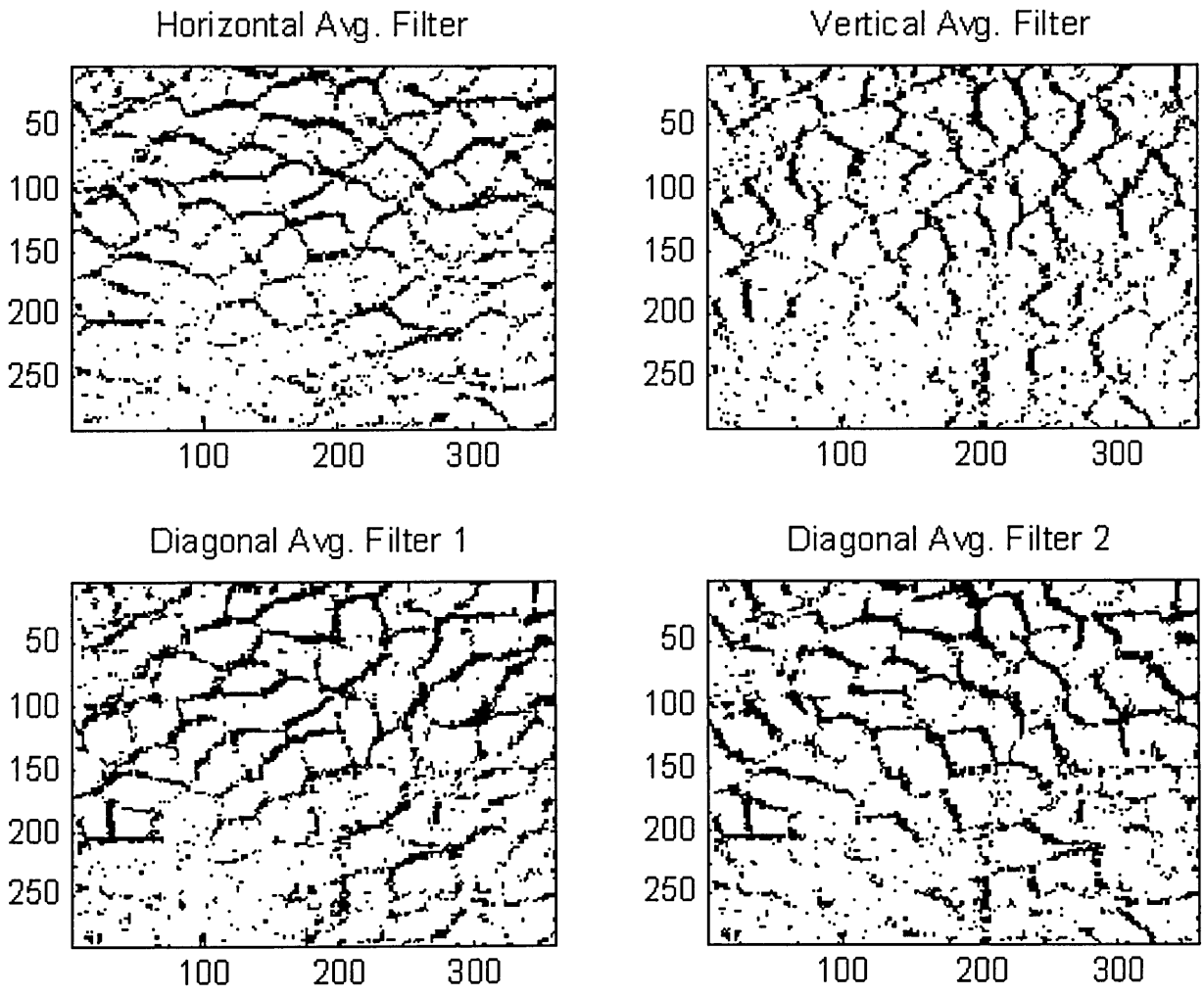

Figure 6.9 Processing the raw image of Fig. 6.3 by the adaptive threshold method, which used the direction averaging filters, yielded a binary image for each of the four directional filters (horizontal, vertical and two diagonal). Here black is LIS and white is intracellular space.

Step 3) involved combining the resulting segmentations of Fig. 6.9. A pixel was deemed as LIS if any of the four directional filters labeled it as LIS. The combined binary image was then median filtered to remove shot noise following the procedure outlined in step 1). The combined, median-filtered image is shown in Fig. 6.10.

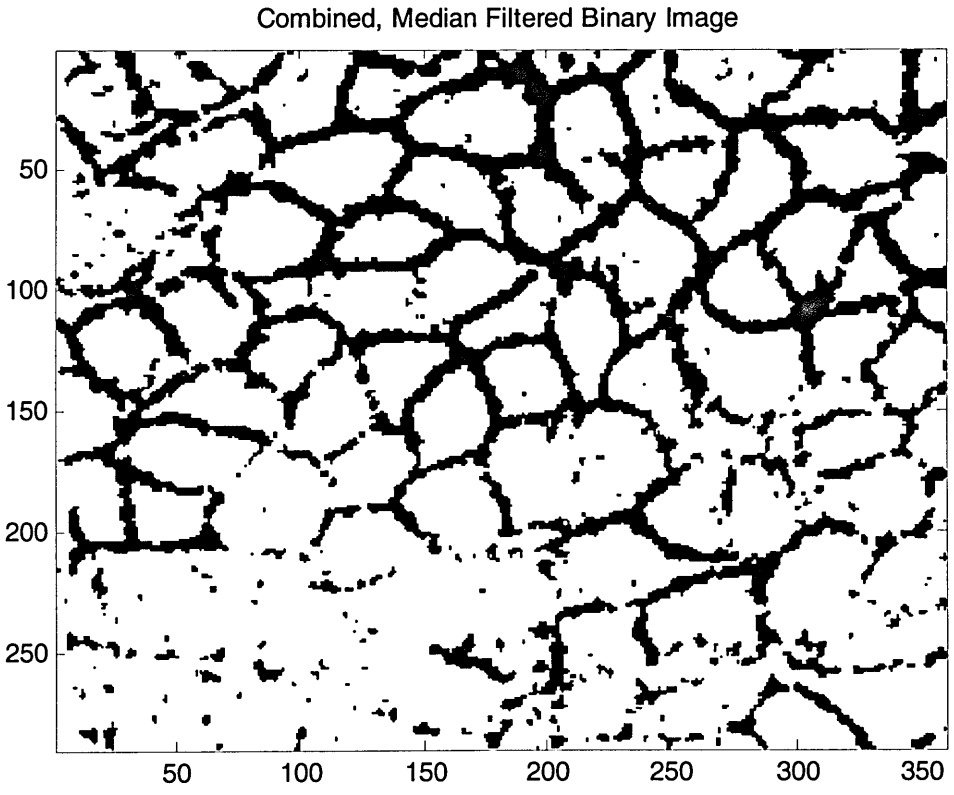

Figure 6.10 The combined, median filtered image obtained by merging all of the four directional filter images of Fig. 6.9 and then passing the result through the median filter of step 1). If a pixel was labeled as LIS in any of the four images of Fig. 6.9 then it was deemed as LIS in the combined image. Black: LIS, white: intracellular space.

In step 4) we removed the numerous small islands of LIS apparent in Fig. 6.10. Since the LIS should be a continuous structure, we removed islands of the LIS whose area was smaller than a prescribed value (in this case the cutoff area was 40 square pixels). The

final analyzed image and the initial raw image are shown below in Figure 6.11.

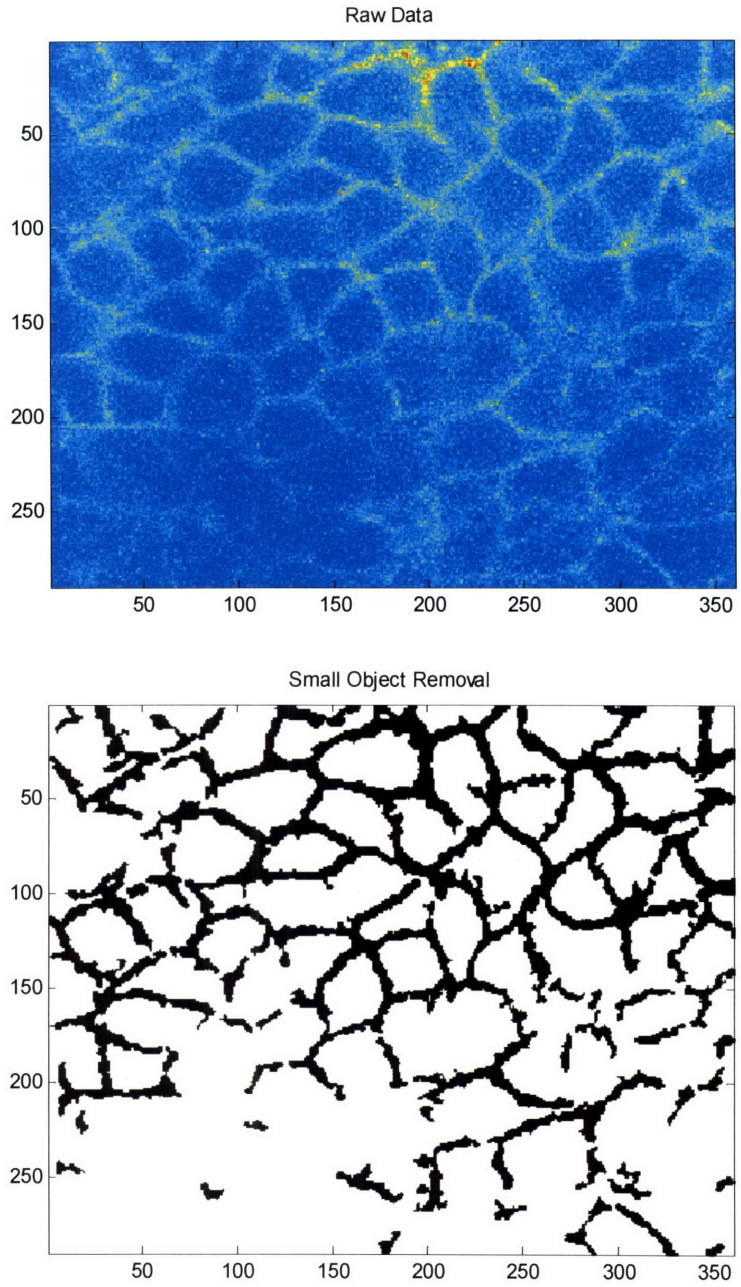

Figure 6.11 The initial raw image (top) and the final analyzed image following the 4-step image processing algorithm outlined above.

Prior to proceeding to analyze more images where the LIS was labeled with FITC-dextran dye (see Chapter 5), we first examined the double-stain case shown in Chapter 5, Fig. 5.7. Here the cells were marked with green fluorescent CellTracker, while the LIS was labeled with a red dextran (TexasRed) tracer. We employed our image analysis algorithm for both the TexasRed dextran and CellTracker image (the analyzed CellTracker image was inverted to give the same output as the TexasRed, see Fig. 6.12). The analyzed images of Fig. 6.12 display nearly identical LIS architectures, indicating that the obtained extracellular space was consistent between two complementary imaging markers. In future analyses we focus only on the dextran labeled LIS images.

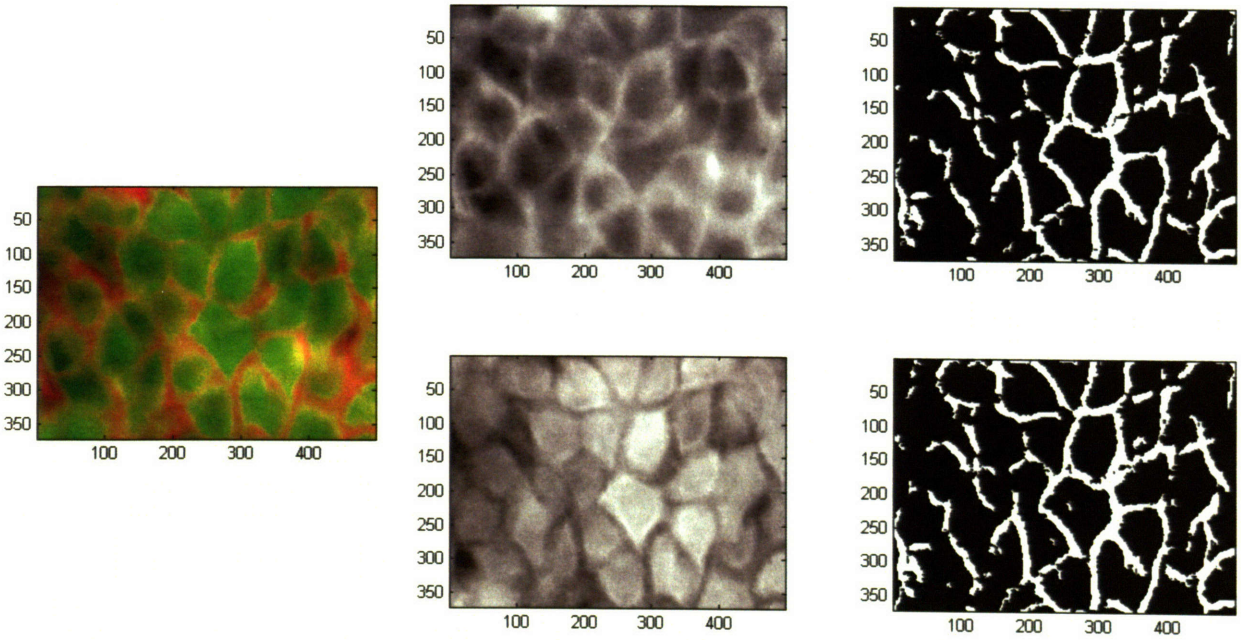

Figure 6.12 Image analysis of complimentary (cell and LIS) markers. Far left: a region of the combined image of Fig. 5.7 (green: cells labeled with CellTracker, orange: LIS labeled with TexasRed dextran). Middle column, top panel: grayscale TexasRed image; bottom panel: grayscale CellTracker image. Right column, top panel: analyzed TexasRed image; bottom panel: analyzed CellTracker image; white: LIS, black: cell.

Applying the above technique of adaptive thresholding to the image of Fig. 6.1 we again explored the threshold effect analogous to equation (1) and Fig. 6.2, only here we used the adaptive thresholds based on the local mean (see equation (2)).

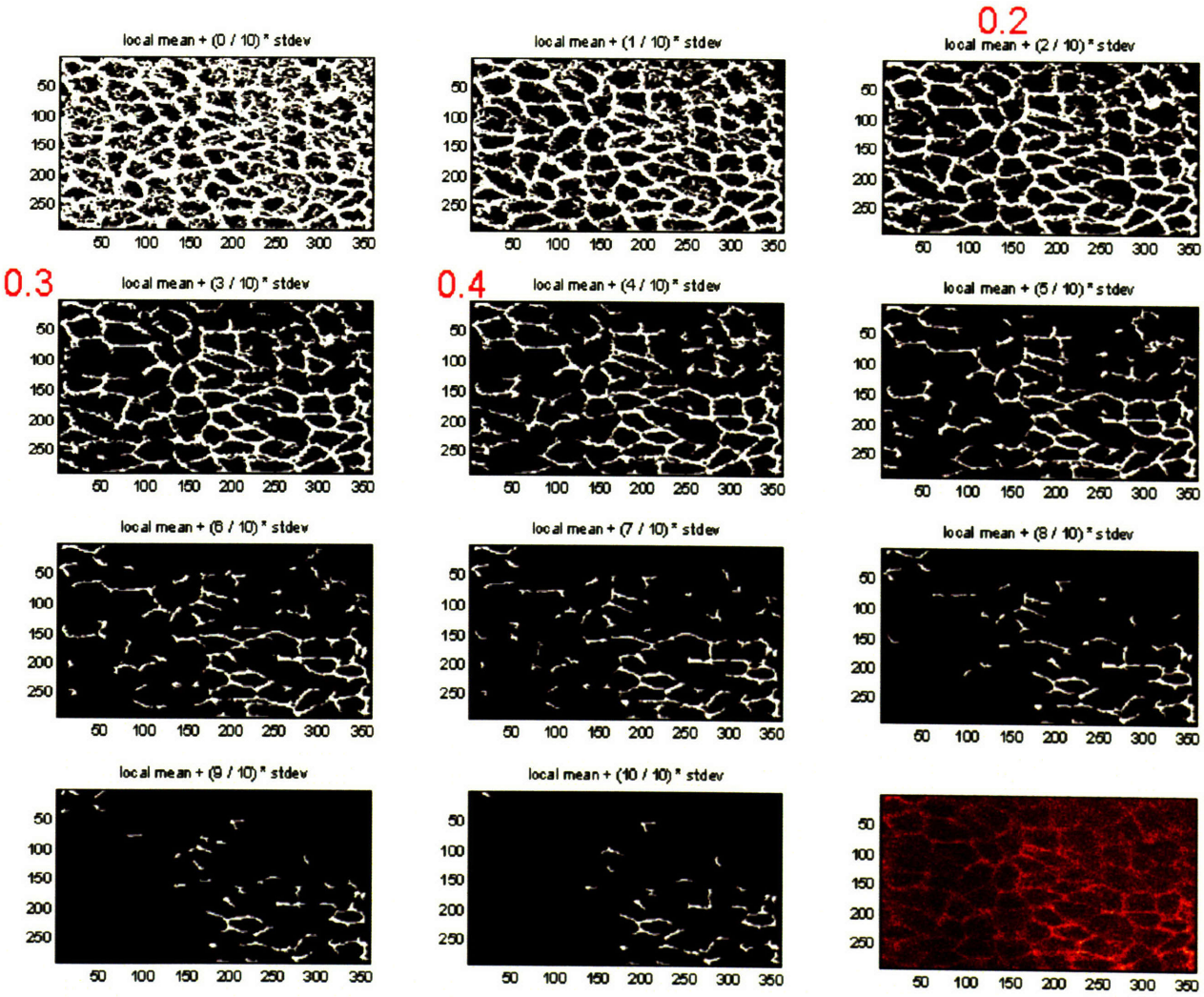

Figure 6.13 Analysis of the raw image in Fig. 6.1 (lower right corner) for a range of thresholds using the 4-step adaptive thresholding algorithm. The thresholds were based on the local mean (see equation (2)) plus a multiple of the standard deviation of the average intensity of all the pixels in raw image. In red are three values (0.2, 0.3, 0.4), multiples of the standard deviation that gave the best results. Black and white images: LIS is white, intracellular space is black.

Comparing Fig. 6.13 with Fig. 6.2, it is clear that the adaptive thresholding algorithm outperforms the flat threshold approach. The three red values (0.2, 0.3, 0.4) next to the images in Fig. 6.13 represent the multiples of the standard deviation that gave the best results by visual inspection. To see the difference between these three values for the threshold a pressure time-course experiment was analyzed with each of the values. We present these findings along with the analysis and quantification of other time-course experiments in the next section.

6.4 Quantifying the pressure induced LIS collapse: results

Having established the 4-step adaptive thesholding algorithm we proceeded to the analyze stacks of images corresponding to time-points during which the LIS was collapsing due to the imposed transcellular pressure gradient (see Chapter 5).

All of the previous analyses were based on a single, planar image, however, as presented in Chapter 5, stacks of planar images were collected to capture the entire height of the LIS. The total number of pixels was counted in each plane and summing the results for a given stack yielded the total LIS volume for a given time-point. Normalizing all of the time-points to the initial, pre-collapse, t=0 time-point allowed us to examine by what percentage the LIS volume decreased over time due to the imposed pressure.

As a representative example, we first show the results of the analysis for the time-series used in Chapter 5, where a pressure gradient of $30cmH_2O$ was applied for 600s. The data is presented in three rows (see Fig. 6.14). The first row displays binary images obtained from the adaptive threshold algorithm, the second row consists of raw images, and the third row shows the overlay of the raw image and the inverse analyzed image.

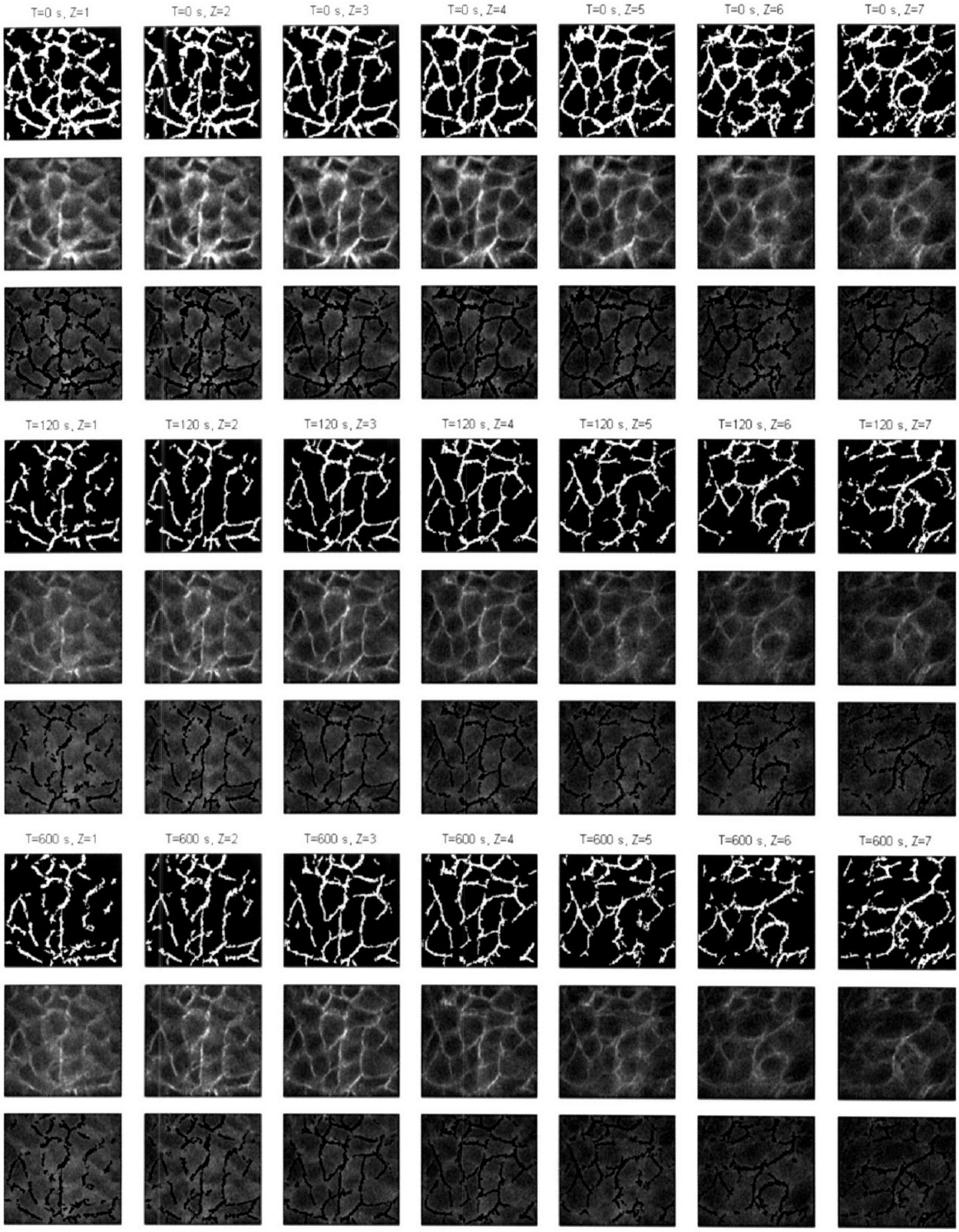

Figure 6.14 Three time-points (0, 120, 600s) in a pressure time-course lasting a total of 600s, corresponding to cells shown previously in Chapter 5. Three rows for each time

point, top row: analyzed image (LIS white, cell black); middle row: raw data; bottom row: overlay of inverted analyzed image (LIS black) and the raw image. Seven columns per time point, each representing a slice in the z-stack (see Chapter 5), where z =1 is the most basal and z =7 the apical slice.

The seven columns per time point indicate the seven slices along the z-direction comprising the stack of images collected for that time point (see Chapter 5 for more images of the cells shown in Fig. 6.14). The distance between z=1 (most basal) and the more apical z=2 slice was 1 micron, meaning that the total LIS height was 7 microns.

Counting all of the white (LIS) pixels in the first row of Fig. 6.14 gave the total LIS volume at t=0. Repeating the same summing procedure for the other time points, and then dividing the volume of each time point to the t=0 LIS volume, yielded the LIS collapse curve for the above experiment (see Fig. 6.15). It should be noted that Fig. 6.15 includes two additional time-points (20 and 300s) that were previously omitted in Fig. 6.14 for clarity (both of these two time points t=20&300s were analyzed using the same image analysis procedure as for t=0, 120, and 600). The obtained LIS collapse curve has several key features: 1) the magnitude of the total LIS collapse is about 40%, 2) almost all of the collapse occurs in the first 120s, and 3) the LIS does not collapse much after 120s and remains at the same volume. Another important point is that the collapse curve seems exponential, which is somewhat to be expected for a compliant biological material like the cellular membrane. In other words, the compressive stress causes the complaint intercellular space to gradually collapse to a state where the applied load is balanced by the cells. A careful examination of the images in Fig. 6.14 reveals that the LIS height

decreased by about 1 micron after 600s under pressure. Since the cells are incompressible, this decrease in height was balanced by a corresponding increase in cell width that in turn caused a decrease in the intercellular space (LIS).

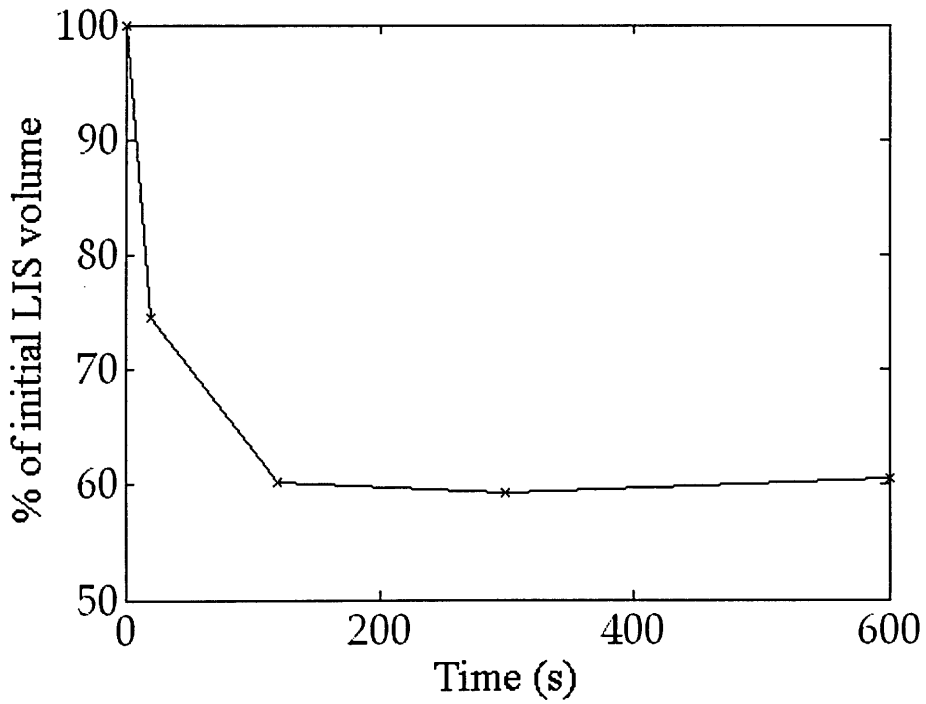

Figure 6.15 LIS collapse curve based on the images of Fig. 6.14 (and two additional time points 20 and 300s omitted in Fig. 6.14 for clarity). The initial LIS volume was taken as 100% and all of the later time-points were normalized to this value, yielding the LIS collapse curve in terms of the percentage of initial LIS volume. For time-point t=20s the LIS volume was about 75% of the initial volume, meaning that the LIS volume decreased by 25% after 20s of pressure.

Applying the same type of analysis and quantification we investigated the effect of varying the threshold over a range of multiples of the standard deviation of the mean

(see Figs. 6.2&6.13). This range included the three values mentioned previously (see Fig. 6.13): 0.2, 0.3, and 0.4. The three corresponding collapse curves (one for each threshold value) are shown in Fig. 6.16. As the figure indicates, the only difference between the three curves was in the magnitude of the LIS collapse (roughly equal to 10% between the 0.2 and 0.4 curves), while the character and shape of the curves remained the same. Based on this analysis we chose the threshold for future experiments to be:

threshold = local mean + 0.3*(standard deviation).

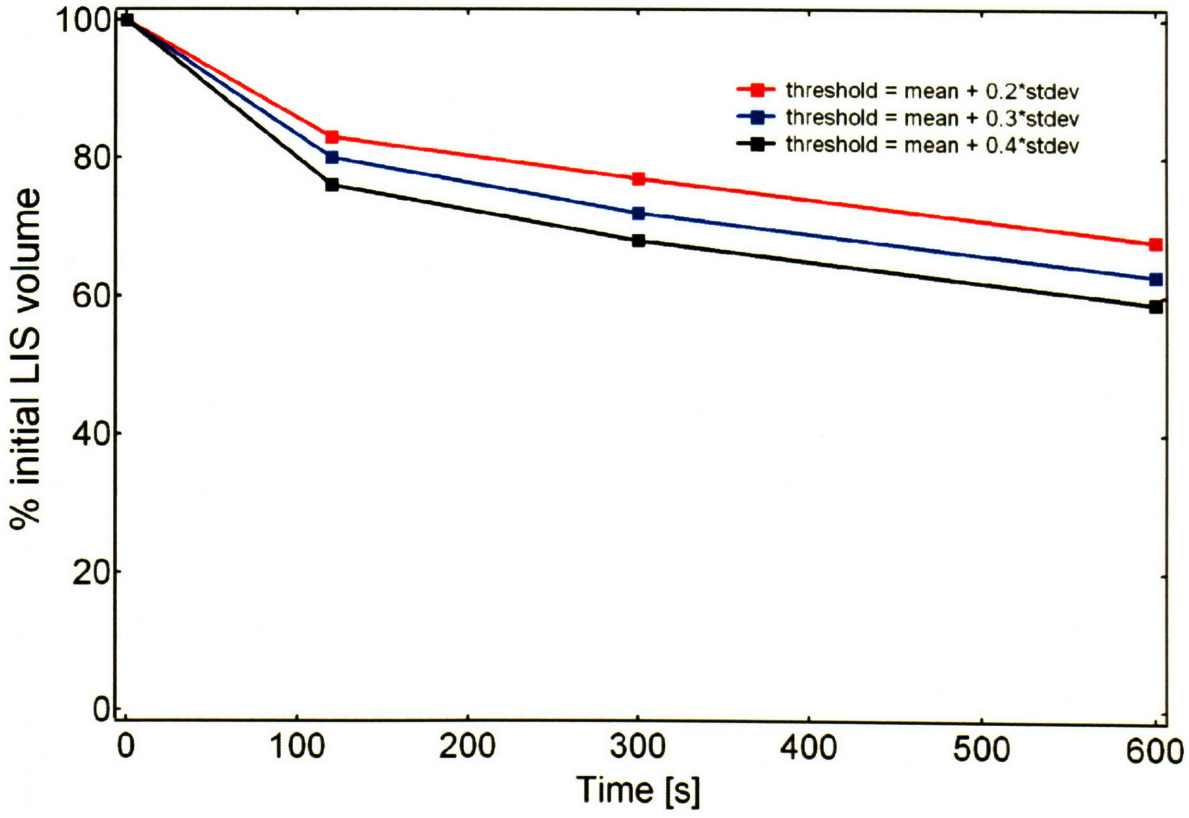

Figure 6.16 The effect of varying the threshold by three different multiples (0.2, 0.3, 0.4) of the standard deviation (see Fig. 6.13). These three values were chosen based on previous image analysis (see Fig. 6.13). The resulting curves differed only in magnitude (roughly 10% difference between 0.2 and 0.4 case), but not in character and shape.

Having established an appropriate algorithm for the determination of the LIS collapse curve, we proceeded to examine the following four questions related to the collapse:

1) How reproducible were the results for a given cell donor?
2) What was the variability across cell donors?
3) How did the magnitude of the applied pressure affect the collapse curves, within and across cell donors?
4) What happened after the pressure was turned off (i.e. after being applied for 600 seconds)?

To answer questions 1) & 2), we performed multiple experiments on three different cell donors (see Fig. 6.17). As in all the previous experiments, the applied pressure gradient was $30cmH_2O$. The three cell donors (labeled 10, 11, and 12) corresponded to three people who differed in age, sex and ethnicity. The identical pressure experiment was performed thrice per donor, meaning that a total of 9 wells were tested yielding 9 collapse curves (see Fig. 6.17). For a given donor, the results were reproducible: the collapse curves were similar in magnitude and followed the same general trend (see Fig. 6.17). Across donors there seemed to be much more variability, with the 10 and 12 donors having collapse curves that tended to be higher in magnitude than donor 11 (see Fig. 6.17). The implication was that cells from donor 11 were more compliant (or less stiff) than the other two donors.

This implication was further tested by focusing on two of the donors: 10 and 11. The two donors were chosen based on the experiments that involved the application of a pressure gradient equal to $30cmH_2O$ (see Fig. 6.17), which begged the question: would

applying a higher pressure cause a greater, more obvious, difference between the donors? Being directly related to question 3), we address this, along with question 4) next.

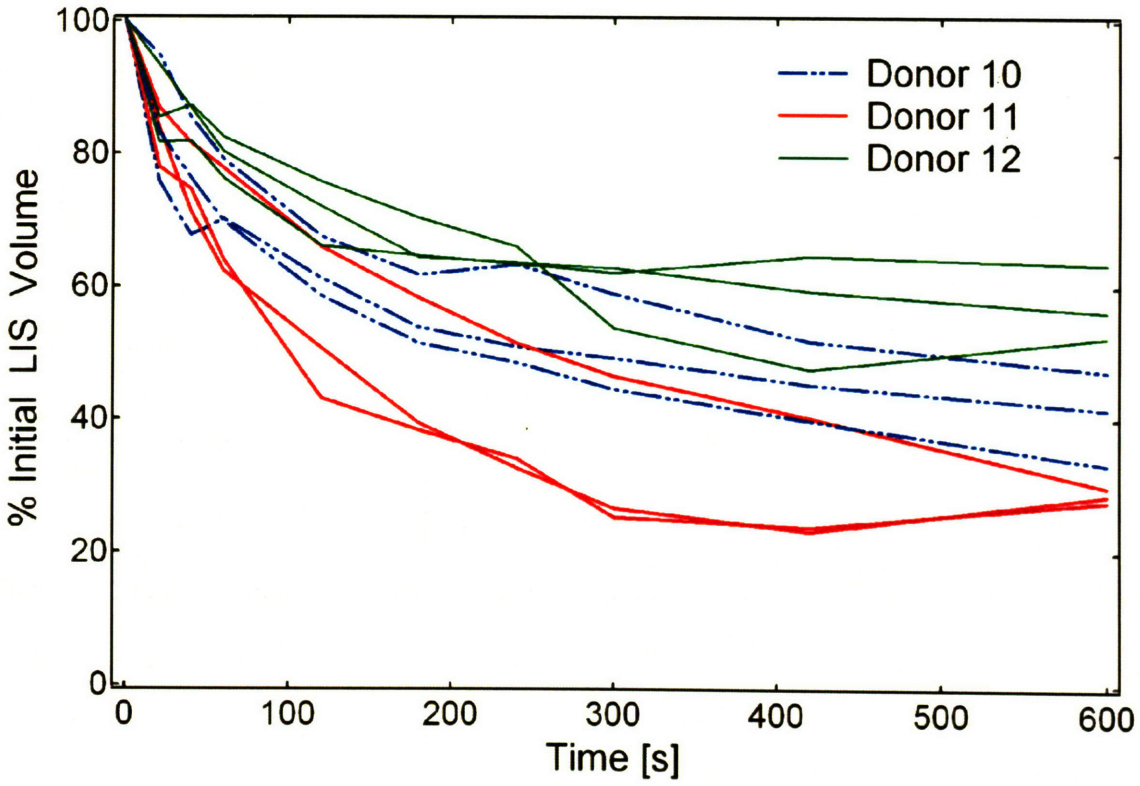

Figure 6.17 LIS collapse curves for three different donors (labeled 10, 11, and 12) under the same conditions: a transcellular pressure gradient of 30cmH_2O applied for 600 seconds. Three identical experiments were performed per donor to address reproducibility (question 1), and three different donors were used to test variability across donors (question 2). The top three green curves correspond to donor 12, the middle three dashed blue curves were obtained from donor 10, while the bottom three red curves were from donor 11.

All of the pressure experiments presented above were performed at a single transcellular pressure gradient of 30cmH_2O. In order to test the effect of the magnitude of the applied pressure, we performed experiments with pressures equal to either 10 or 50cmH_2O. Also, to answer question 4) we expanded our experimental protocol to include an equal period of time after the pressure was turned off, and we called this interval the uncollapse period. Hence, the new protocol was: 600s of pressure (LIS collapse) followed by 600s of no pressure (uncollapse). This protocol was then applied to the two donors (10 & 11) chosen above (see Fig. 6.17). The results are shown below in Fig. 6.18. For a given donor and pressure, the experiment was repeated three times. Since we used two donors (dashed blue curves: donor 10, solid red curves: donor 11, see Fig. 6.18) and two pressures (10 & 50cmH_2O, labeled on each curve), the experiments yielded four curves. The four curves each correspond to the average of three identical experiments, and the error bars represent the standard deviation of the means (see Fig. 6.18).

The results clearly indicated that donor 11 collapsed more than donor 10 and this was true at any magnitude of pressure (for 30cmH_2O see Fig. 6.15; for 10 and 50cmH_2O see Fig. 6.18). Likewise, the relative amount of collapse between 10 and 50cmH_2O was also greater for donor 11. Further support for our hypothesis that donor 11 was more compliant came from the uncollapse data. As Fig. 6.18 suggests, during the uncollapse period (between 600 and 1200s) the cells of donor 11 returned relatively closer to their initial, pre-collapse value. In other words, when the pressure was suddenly turned off the cells from donor 11 cells showed a greater tendency to return to their original geometry than those of donor 10, relative to the point where the cells were at the onset of

uncollapse. The general trends of a decrease in LIS volume during collapse followed by an increase during uncollapse were observed for both of the donors 10 and 11.

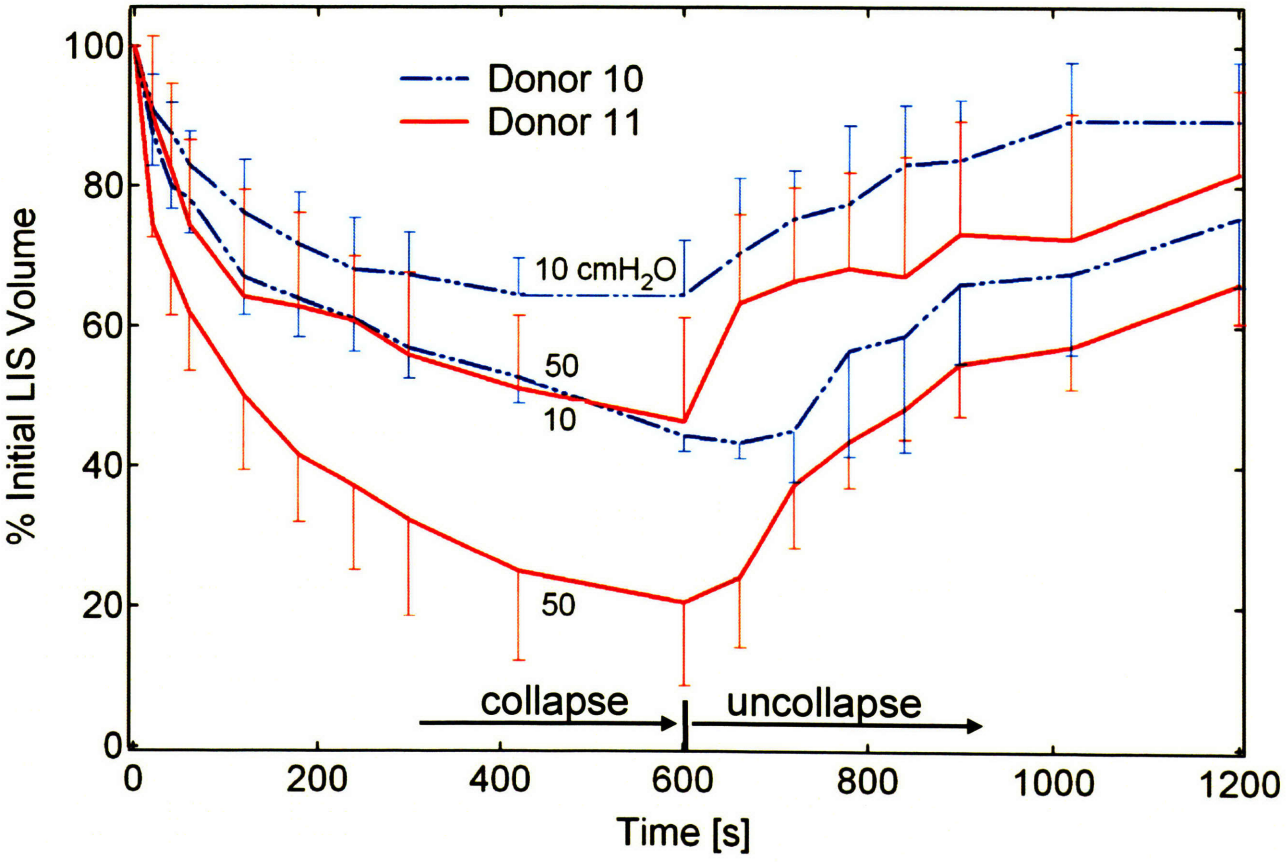

Figure 6.18 LIS collapse curves for two different donors (blue dashed lines: donor 10, red solid lines: donor 11) under two different pressure gradients (10 or 50cmH_2O, labeled on each curve). During the first 600s the cells were subjected to a transcellular pressure gradient (the collapse period), followed immediately by an equal period of no pressure (uncollapse, lasting from 600 to 1200s). Each of the four curves represents the average of three identical experiments; error bars indicate the standard deviation of the means.

The measured collapse curves also provide insight into the coupled mechanical behavior of the LIS and NHBE cells. The exponential character of the collapse due to the application of a constant pressure gradient agrees with the observed deformation for both a biological (Fung, 1981; Haslach, 2005; Koay et al., 2003) and a non-biological material (Kojic and Bathe, 2005) undergoing creep. The rate of collapse and maximal volume change both increase with increasing pressure (see Fig. 6.18), meaning that the deformation and deformation rates (i.e. collapse) are proportional to the mechanical load applied, as expected for a viscoelastic material (Fung, 1981).

The uncollapse results indicate that our cells display some plasticity (Fung, 1981), since they do not recover to the initial, pre-collapse state. Pressure-induced cytoskeletal rearrangements (Koay et al., 2003; Stamenovic et al., 1996), could be a potential explanation as to why there is not full recovery after pressure cessation (i.e. there is viscous loss during the collapse phase).

In this chapter we described the development of a 4-step image analysis algorithm based on adaptive thresholding. The algorithm was designed to process stacks of images acquired from the high-speed two-photon microscope (HSTPM, see Chapter 5 for details). The outputs of the algorithm were analyzed binary images (LIS=1 and intracellular space=0) as well as quantification of the total LIS volume (i.e. total number of pixels labeled as LIS) for each stack of raw images. During a pressure-induced collapse, the calculated LIS volume for each time-point (i.e. each stack of images from the HSTPM) was normalized to the initial LIS volume yielding a LIS collapse curve (normalized LIS volume vs. time). We then probed the effects of donor variability and pressure magnitude,

and concluded that cells from one donor (e.g. donor 11) collapsed more than cell from another donor (e.g. donor 10), while for a given donor the results were reproducible.

The obtained collapse curves could now be used as input into our numerical model (see Chapter 3), in order to compute the corresponding changes in LIS ligand concentration, ultimately providing more insight into how cells transduce externally imposed geometrical alterations of their extracellular space. These numerical results, along with a novel, 3-D model that takes into account inhomogeneities in the LIS collapse, are presented in the next chapter.

7. Numerical results: 2-D and 3-D model

7.1 Introduction

Through the use of image analysis techniques (see Chapter 6) we were able to quantify how the LIS geometry changed during a pressure-induced collapse. We obtained collapse data on cells from three different donors (labeled as 10, 11, and 12) and three different pressure magnitudes: 10, 30, and 50cmH_2O. For donor 12 we only performed the 30cmH_2O experiment, and then chose to focus on the 10 and 11 donor cells, since they appeared to have different collapse dynamics. In this chapter we use the experimental collapse curves as direct input for our numerical models (see Chapter 3) (Kojic et al., 2006).

For the 30cmH_2O case, predicted ligand concentration dynamics were compared to biochemical assays of EGF receptor (EGFR) phosphorylation dynamics. This comparison showed (see below) that in the first few minutes after the application of pressure, there was a reasonable direct correlation between the predicted increase in ligand concentration and EGFR phosphorylation. However, after 3 minutes EGFR phosphorylation decreased (whereas predicted ligand concentration kept increasing) suggesting that compensatory, dephosphorylation mechanisms were active. Nonetheless, the correspondence between predicted ligand dynamics and receptor phosphorylation in the first few minutes implies that pressure could lead to the initiation of a transduction signal that then gets amplified intracellularly and ultimately leads to the observed increase in ERK-phosphorylation (see Chapter 1).

In addition to the results based on the 2-D model of Chapter 3 (Kojic et al., 2006) using actual LIS collapse measures as input, we also present some preliminary data using

a novel 3-D numerical model, where the input was not the quantified collapse curve, but rather analyzed planar images (see Chapters 5 & 6). As such, the 3-D model represents a more intimate bridge between experimental imaging and numerical modeling. Furthermore, the 3-D model takes into account local LIS heterogeneities and the 3-D results suggest that cellular signaling can be highly localized, with small hot-spots of increased ligand concentration appearing in different regions of the LIS.

7.2 Results of the 2-D numerical model

Based on the 2-D model presented in Chapter 3, for a given LIS collapse curve (input) we were able to predict ligand concentration dynamics (output). Here, we first examine the case for the two different donors (10 and 11) and two applied pressure magnitudes (10 and 50 cmH_2O). Since we were interested in understanding how the LIS collapse initiates cellular signaling, we focused only on the time during which the cells experience a transcellular pressure gradient (i.e. the first 600 seconds of the collapse curves). Therefore, the previous collapse curves (see Fig. 6.18 in Chapter 6) were plotted again only for the first 600 seconds (see Fig. 7.1). In the figure, each marker (square for 10 cmH_2O, and diamond for 50cmH_2O) represents the average value for the individual time-point (since all of the imaging data was collected at discrete time points, see Chapter 6). Then, each data set was fitted with an analytical curve, and in all cases the fitted curve was a double exponential, as this seemed to provide the best fit (see Fig. 7.1). For the two cases (donor 10 @ 50cmH_2O and donor 11 @ 10cmH_2O) only one curve was fitted through the data, since the collapse curves were very similar to each other (see Fig. 6.18 of Chapter 6 and Fig. 7.1).

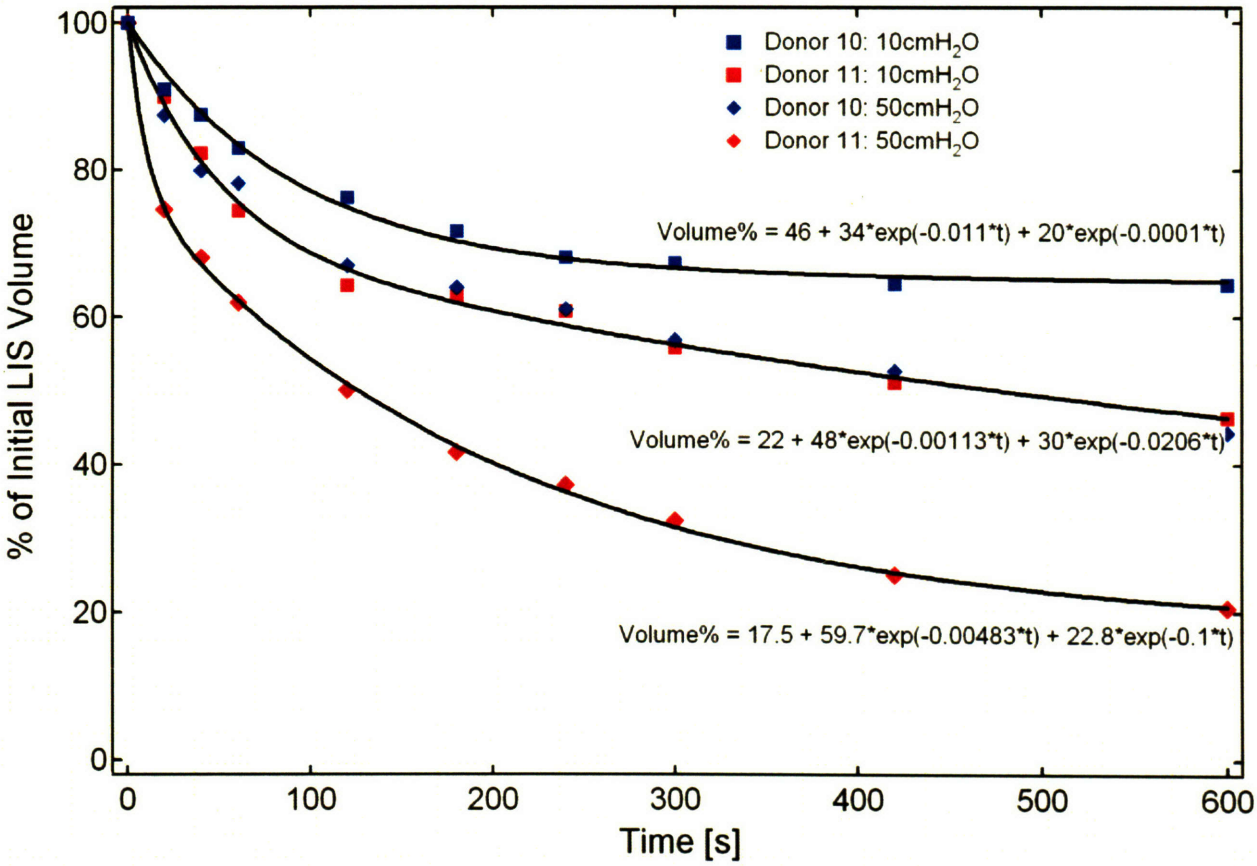

Figure 7.1 LIS collapse curves for donors 10 (blue markers) and 11(red markers), redrawn from Fig. 6.18 in Chapter 6. Squares indicate that the cells were exposed to a transcellular pressure gradient of 10cmH_2O, whereas diamonds represent a pressure of 50cmH_2O. Solid black lines correspond to fitted curves (equation shown next to each curve). One curve was fitted through the donor 10@50cmH_2O and donor 11@10cmH_2O datasets since both had similar values.

The fitted curves (see solid lines in Fig. 7.1) were then used as input into the 2-D model (see Chapter 3 for details about the 2-D model (Kojic et al., 2006)). For consistency, we kept the same parameters as presented in Chapter 3, i.e. D_{LIS}=1.8 $\mu m^2/s$

and D_{out}=75 $\mu m^2/s$, LIS height h=15μm. The results are shown in Fig. 7.2, where on the same graph we plot both the collapse curves and the corresponding normalized mean concentrations.

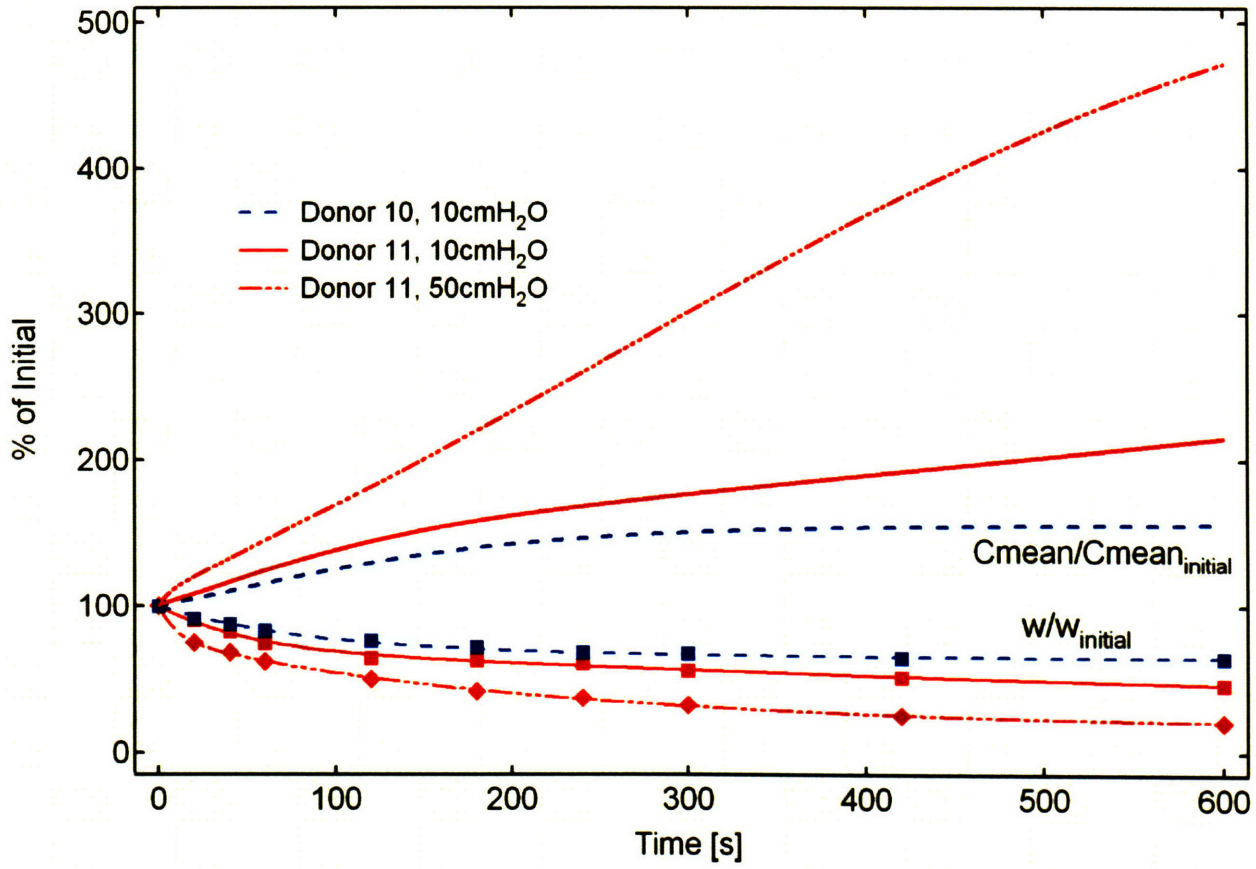

Figure 7.2 Model output showing computed percentage increase in ligand concentration (above 100) and LIS collapse curves (below 100). Dashed blue lines: donor 10@10cmH_2O; solid red lines: donor 11@10cmH_2O; red dashed line: 11@50cmH_2O.

The 2-D model focuses on one characteristic LIS surrounding two neighboring airway epithelial cells and thus deals with changes in LIS width (see Chapters 1 &3). To use the volume collapse curves as input into this model, we assumed that the quantified

volume change (see Fig. 7.1) corresponds exactly to the change in LIS width. Hence, the volume collapse curves were labeled as LIS-width collapse curves (see Fig. 7.2). Implicit in our assumption is that the collapse of a group of cells can be represented by a collapse of an individual, characteristic LIS. Thus, we have neglected heterogeneities that can occur in a population of cells (these heterogeneities will be addressed with the 3-D model, presented later in this chapter). However, even with the above assumption we can still evaluate the effect of collapse dynamics on ligand concentrations in the LIS.

As Fig. 7.2 indicates, there were large differences in ligand dynamics based on the inputted width collapse. The two curves representing $10cmH_2O$ (blue dashed and solid red, see Fig. 7.2) had ligand concentrations that relatively mirrored the LIS collapse curves. However, for the $50cmH_2O$ case (donor 11, dashed red curve in Fig. 7.2) the concentration curve seems not to mirror the LIS collapse. The main reason for this deviation was the rapid and relatively large change in LIS width. Hence, during the 600s, there was insufficient time for the concentration to equilibrate and reach a plateau (i.e. new steady-state) as was the case for the other two, slower collapsing cases ($10cmH_2O$). This effect was described in more detail in Chapter 3, where a slower collapsing LIS reached a new steady-state more quickly than a rapidly collapsing LIS (e.g. see Fig. 3.5 in Chapter 3). We then postulate that, based on the differences in concentration dynamics (see Fig. 7.2), there could be corresponding differences in receptor activation and intracellular signaling.

To further investigate how the predicted changes in ligand concentration relate to cell signaling, we first examined the $30cmH_2O$ case, for which we had previously performed assays of EGF receptor (EGFR) phosphorylation. The EGFR was chosen since

its activation is rapid and it represents the most proximal signaling event during LIS collapse. The receptor, being on the cell membrane (Yarden and Sliwkowski, 2001), provides the key connection between intracellular and extracellular space, acting as a conduit for mechanotransduction (Freeman and Gurdon, 2002; Tschumperlin et al., 2004). Thus, the original signal to the cell (that the local microenvironment has changed) occurs at the receptor level and then this signal gets amplified inside the cell through other phosphorylation pathways (Tschumperlin et al., 2004).

EGFR phosphorylation was measured using a commercial pEGFR kit (Biosource; Camarillo, CA) for the following time-points: t=0 (just prior to pressure), followed by t = 60, 120, 180, 240, 300, 450, 600s under pressure (see Fig. 7.3). The experiment was repeated four times and the applied transcellular pressure gradient was always $30cmH_2O$. The points in Fig. 7.3 represent the average of the four experiments while the error bars indicate the standard deviation of the means. The measured pEGFR was normalized to the initial pEGFR at t=0, and we report the percent ratio of $pEGFR/pEGFR_{initial}$. The obtained normalized pEGFR curve increases in the first 180s followed by a decrease close to baseline at 450s after the onset of pressure. The final, i.e. 600s, time-point showed the greatest variability and was therefore difficult to interpret. The Gaussian-like character of the curve of Fig. 7.3 suggests that there are compensatory mechanisms that are involved in dephosphorylation of the EGFR leading to a gradual decrease to baseline receptor signaling.

To compare how the measured pEGFR compares to the predictions of our model we re-examined the $30cmH_2O$ pressure experiment where the LIS collapse curves were determined for several donors (see Fig. 6.17 in Chapter 6).

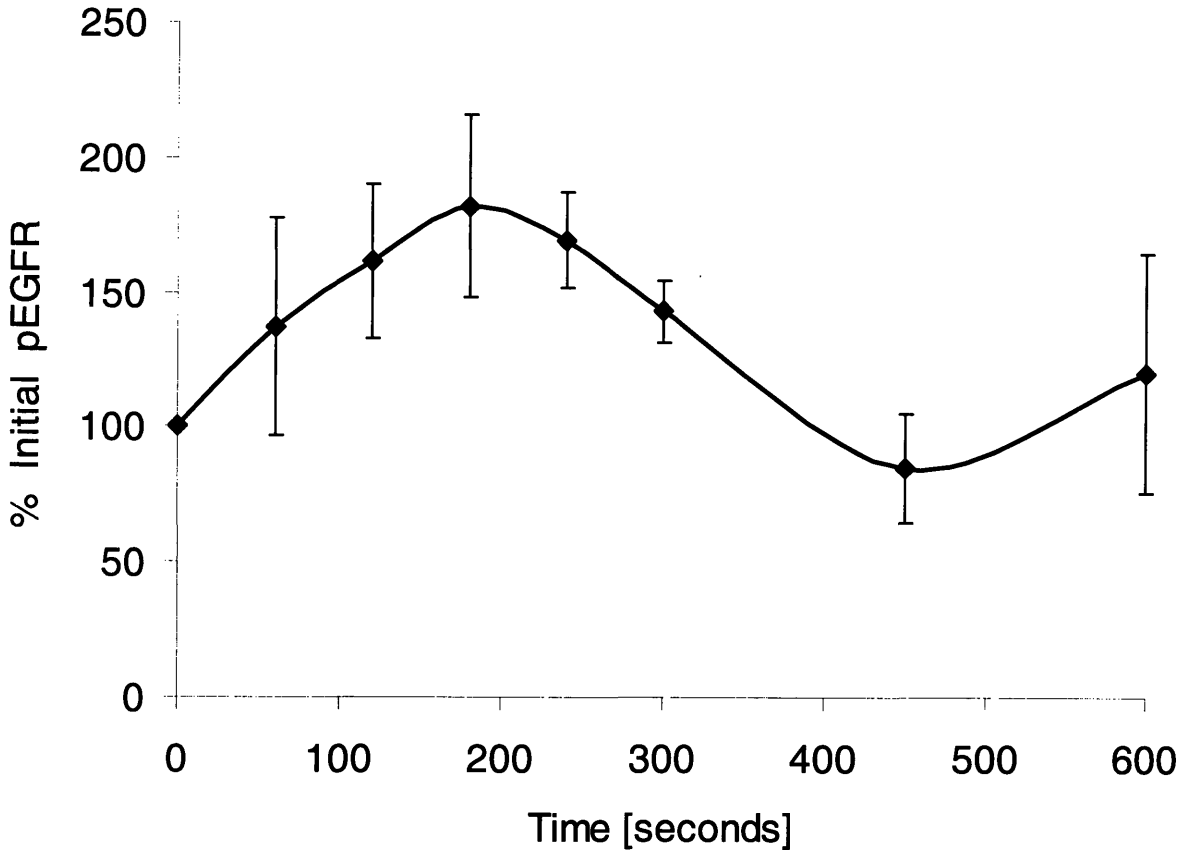

Figure 7.3 Normalized pEGFR (in terms of percent of initial pEGFR at t=0) for an applied transcellular pressure gradient of 30cmH_2O. Time t=0 signifies the baseline signaling just prior to pressure application, whereas time t>0 corresponds to time under pressure (peak of 180% at t=180s). The markers at time point represent the average of four identical experiments and the error bars indicate the standard deviation of the means.

Since the pEGFR curve was obtained in cells that were from a different donor than all of the donors previously used to measure LIS collapse, we averaged all of the collapse curves for the 30cmH_2O experiment (see Fig. 7.4). To get a sense of the dynamic range we examined curves corresponding to the largest and smallest collapse (see Figs.

7.4 & 7.5). In Fig. 7.4 we plot the nine collapse curves of Fig. 6.17 (Chapter 6) again, along with the average collapse curve, standard deviation and fitted exponential curve.

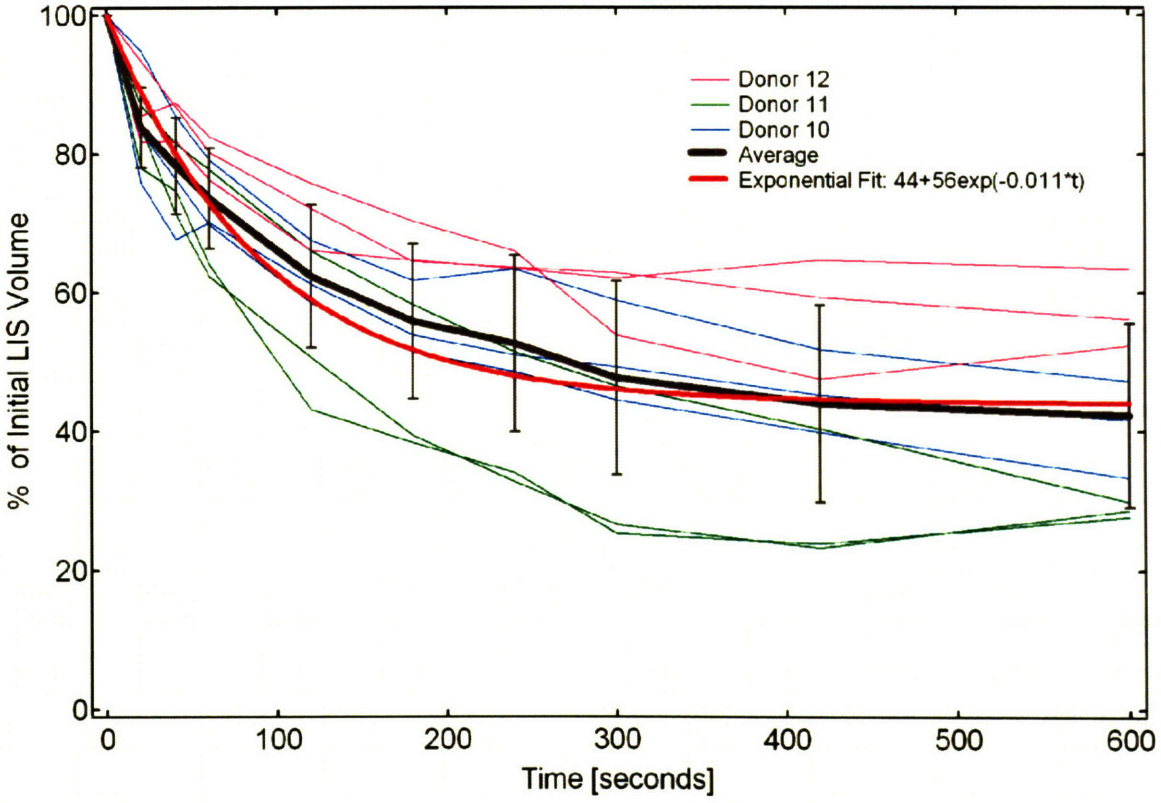

Figure 7.4 The collapse curves of Fig. 6.17, Chapter 6 for the 30cmH_2O experiment. Three identical experiments were performed for each of the three donors (blue: 10, green: 11, purple: 12) for a total of nine collapse curves. Black curve: average of the nine collapse curves, error bars: standard deviation. Red curve: exponential fit used as input into the numerical model.

The fitted exponential curve of Fig. 7.4, along with exponential fits to the top purple and bottom green curve of Fig. 7.4 (see Fig. 7.5) were then directly inputted into the 2-D numerical model. The resulting normalized mean ligand concentration curves

(see Fig. 7.5) span the probable range for the case of 30cmH_2O of pressure. We display these curves, along with the normalized pEGFR values from Fig. 7.3, in Fig. 7.5 below.

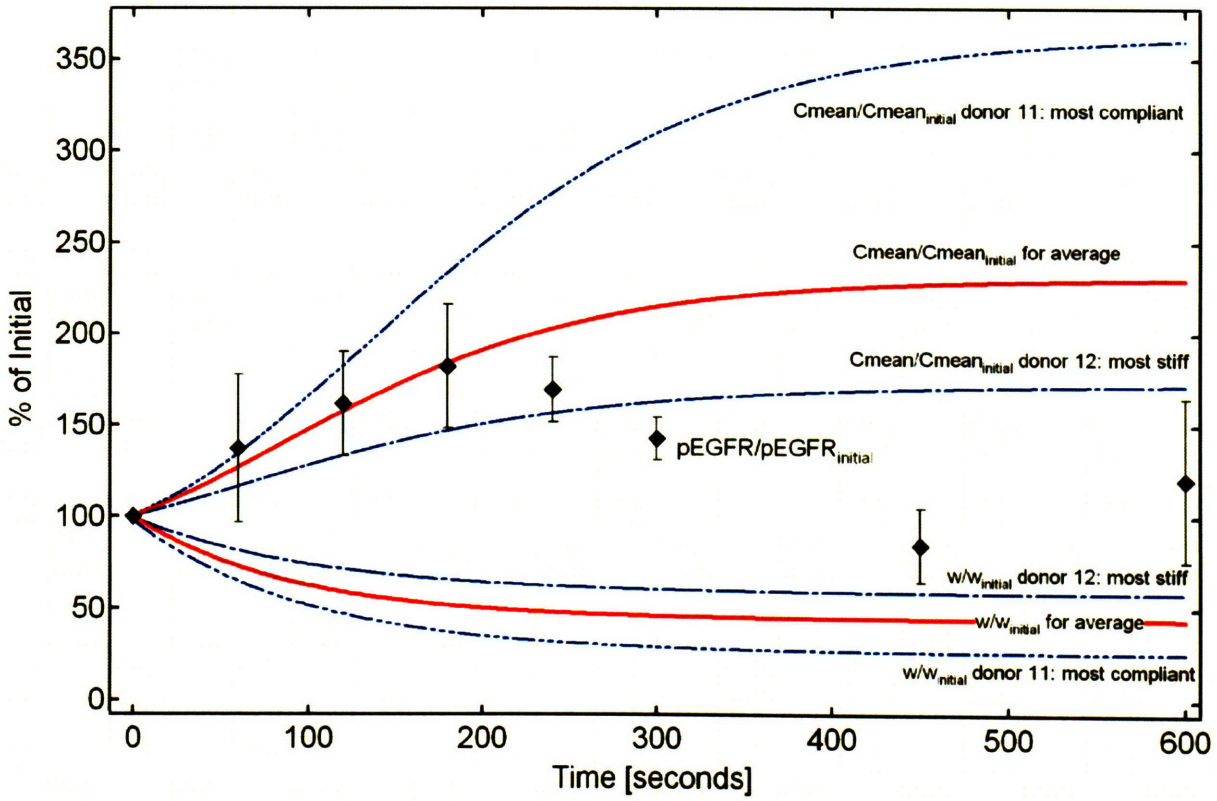

Figure 7.5 Changes in mean measured LIS width (lower curves), ligand concentration (upper curves), and normalized pEGFR from Fig. 7.3 (diamond markers) presented as a percentage of the initial values. Lower curves: middle red curve was the exponential fit curve of Fig. 7.4 (average of all data); the two blue dashed curves were exponential fits of the most stiff (top purple curve of Fig. 7.4, donor 12) and most compliant (bottom green curve of Fig 7.4, donor 11) cells. Upper curves: normalized mean ligand concentration in the LIS (output of the model) for the corresponding collapse curve (input to the model, lower curves). Error bars represent standard deviation of the pEGFR means (see Fig. 7.3)

The predicted ligand concentration at 600s ranged from 170% for the most stiff to about 360% for the most compliant cells (see top curves in Fig. 7.5) and we expect that the cells used to measure pEGFR (markers in Fig. 7.5) fall somewhere in this range. Most of the concentration increase occurred in the early stages of the collapse, when the width decreased most rapidly. At t=180s the normalized mean ligand concentration was 150, 185, and 235% of initial, for the stiff, average, and compliant case, respectively. This meant that for all three cases >65% of the total increase in concentration (for stiff: 88%, average: 80%, and compliant: 65%) occurred in the first 180s. We chose the t=180s time-point since that was when normalized pEGFR peaked. The good correlation between the dynamics of pEGFR and ligand concentration in the first 180s suggests that an early increase in ligand concentration causes rapid phosphorylation of the EGFR. Then, in our case after 180s, dephosphorylation mechanisms decrease receptor activation back to baseline. However, the initial increase in receptor activity could be sufficient to induce a signaling cascade that ultimately results in observed ERK phosphorylation (see Chapter 1, (Tschumperlin et al., 2004)). The compensatory dephosphorylation mechanisms also prevent unwanted, persistent cell activation. The cell thus responds dynamically to a change in extracellular geometry and transiently transduces the mechanical stimulus (pressure application) via the EGFR-ERK signaling pathway (Tschumperlin et al., 2004).

Our model results predict that ligand concentration should keep increasing until t plateau value is reached (see Fig. 7.5), but this is not the observed behavior. We speculate that the main reason why the concentration does not follow the same trend as the pEGFR curve is due to the lack of EGFR kinetics in the model (i.e. there are no receptors in the model).

7.3 The 3-D numerical model

The results presented so far are from the 2-D diffusion-convection model (see Chapter 3, (Kojic et al., 2006)) which used as input the measured LIS collapse curves (i.e. LIS width as a function of time) in order to examine ligand concentration changes in the LIS. To gain further insight into how local changes of the LIS could affect ligand dynamics a more general, 3-D model is needed. Here, we present the development of a 3-D numerical model that takes into account local heterogeneities, since the geometry of the model is based on an analyzed planar image for a given time-point. Before showing preliminary results, we first describe the geometry of the 3-D finite element model and then explore a collapse scenario.

The key step in the assemblage of the 3-D model was prescribing the finite element nodes, i.e. the geometry. For the pre-collapse geometry we chose the t=0, z=4 image of Fig. 6.14, Chapter 6 (same images were used in Chapter 5) and for the collapsed geometry (30cmH_2O of pressure) the corresponding t=20 image was analyzed (see Fig. 7.6). Then, a region containing the central cell and its six neighbors was selected for both time-points and within this region the LIS coordinates were obtained. Minor corrections were made to ensure a continuous LIS, and a set of boundaries was determined for each cell (see bottom row of Fig. 7.6). The smoothing was performed to remove some imaging artifacts that appeared in later time points (see Fig. 6.14 in Chapter 6) as well as to avoid extremely complex geometries that are biologically unlikely and can induce numerical problems. These problems arise due to the inherent mesh-dependence of the finite element method (Bathe, 1996), which requires that the position of each node is accounted for and tracked throughout the collapse process.

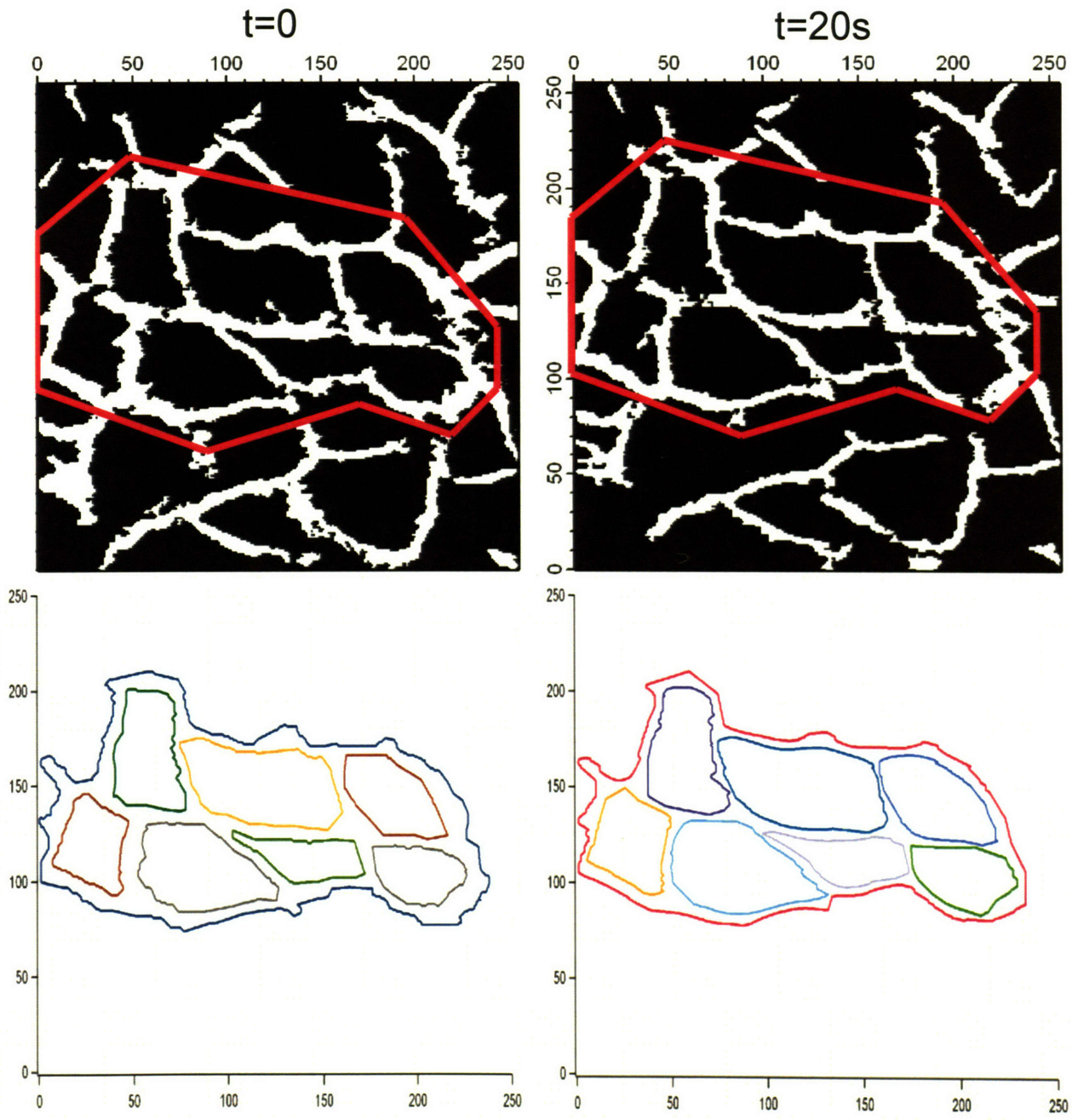

Figure 7.6 The analyzed images from Fig. 6.16 in Chapter 6 (top row, t=0 & 20s) were the basis for the geometry of the 3-D model. A region of seven cells (red line in top row) was chosen, and the coordinates of the LIS boundary within this region was determined. After manual smoothing and corrections to ensure a continuous LIS the processed LIS boundaries were obtained for both time points. The coordinates of the new boundaries

were used as the nodes for the finite elements in the 3-D model. Axis markers indicate number of pixels.

The analyzed boundaries of the LIS (bottom row of Fig. 7.6) were then converted into nodal coordinates for the finite elements by subdividing each boundary into a smaller number of line elements so that each coordinate of an individual contour for t=0 had a corresponding coordinate in the t=20s contour (see Fig. 7.7).

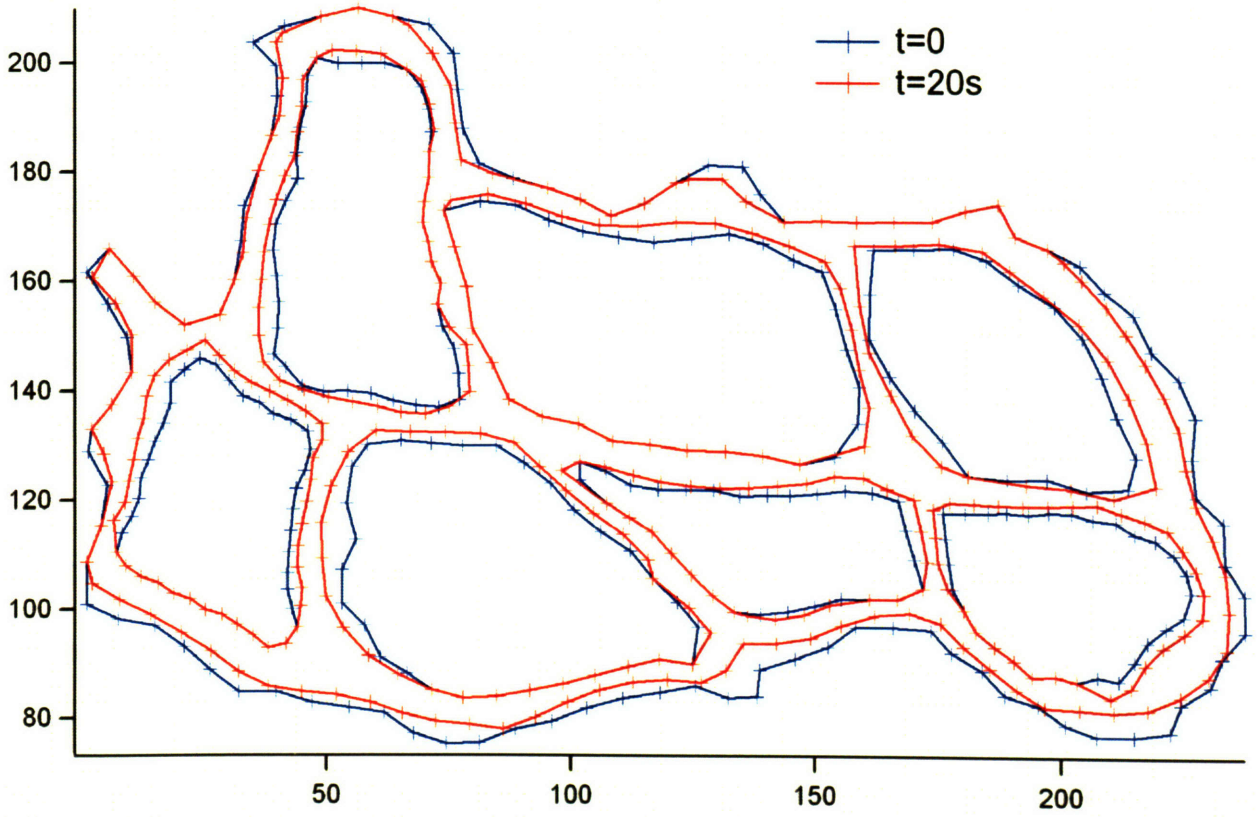

Figure 7.7 LIS boundaries from Fig. 7.6 (blue: t=0, red: t=20s) subdivided into equal number of line segments. Markers: nodes for finite elements in the 3-D model. Each marker in t=0 has a corresponding marker in t=20s. Axis labels: number of pixels.

The 3-D model was constructed based on the nodes shown in Fig. 7.7, with the assumption that the LIS geometry did not change along the apico-basal z-axis (perpendicular to the plane of Fig. 7.7). In other words, we took the boundaries of Fig. 7.7 and extended them in the perpendicular direction. Implicit in our assumption was the notion that the LIS wall moved uniformly along the apico-basal z-axis. This assertion was justified based on the analyzed stacks of images from various pressure experiments (see Chapter 6).

The 3-D representation of Fig. 7.7 included a total LIS height of 15 microns, and an underlying reservoir that extended to 15 microns below the LIS (see Fig. 7.8). The height of the LIS was the same as for the 2-D model (see Chapter 3), whereas the reservoir was expanded to 15 microns due to the 3-D structure of the model. The coordinates (i.e. markers) from Fig. 7.7 served as nodes for finite elements on the LIS boundaries, while the inside of the LIS was discretized using a PAK mesh-generation algorithm (see Fig. 7.8). The individual finite elements are represented with white lines (nodes at intersections).

The same general case as presented in Chapter 3 was examined, with the following boundary conditions: at the bottom of the reservoir the ligand concentration was zero, ligands were constitutively shed into the LIS from the cell surface at a rate q=10 molecules/cell/min, and the most apical LIS surface and the top layer of the reservoir were considered to be impermeable walls. We then first solved for the steady state concentration when D_{LIS}= 1.8 $\mu m^2/s$ and $D_{reservoir}=D_{out}$=75 $\mu m^2/s$, which assumes hindered diffusion of HB-EGF in the LIS and unhindered, free diffusion in the reservoir. The steady-state concentration result for the initial, pre-collapse geometry (see blue

contours in Fig. 7.7) is shown in Fig. 7.8, where the colors correspond to the scale-bar (units of ng/mL).

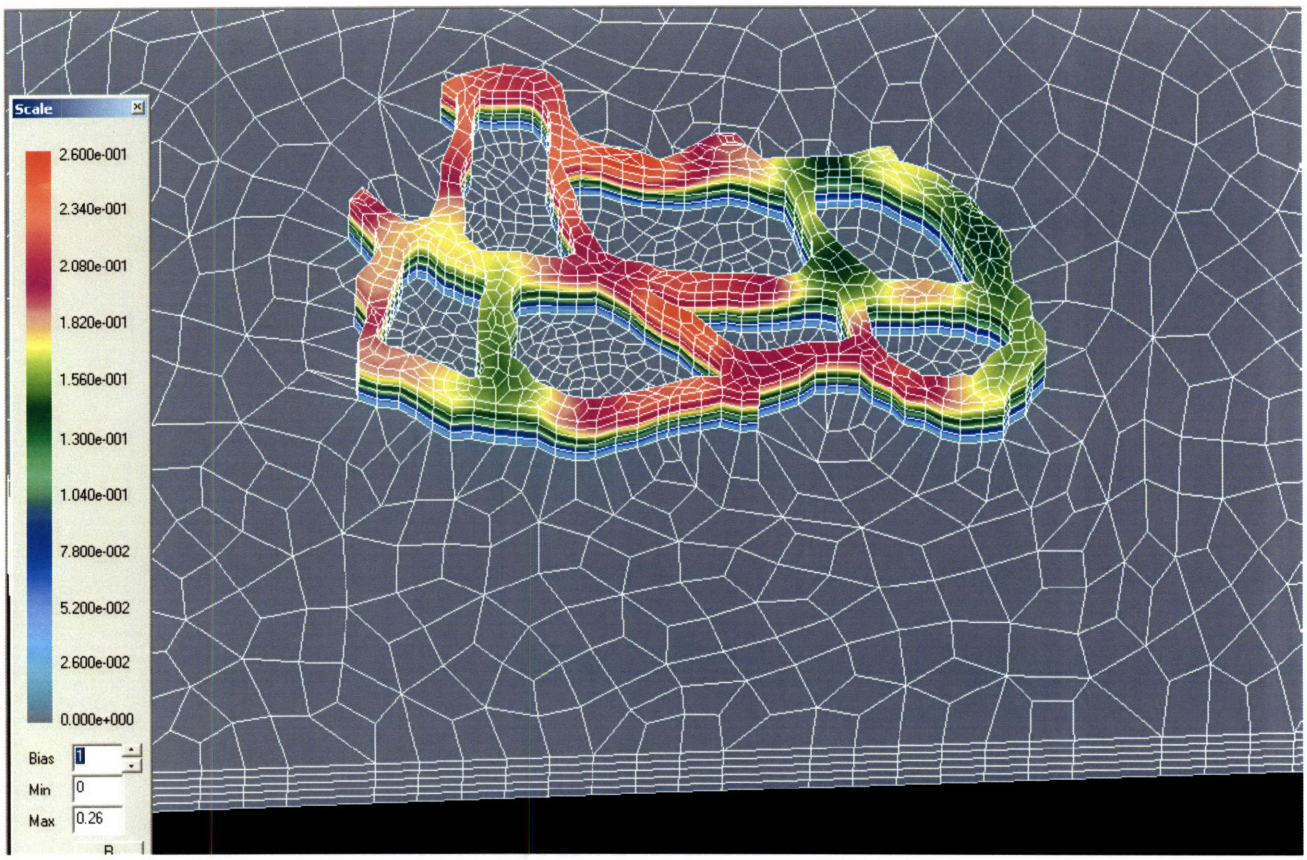

Figure 7.8 Steady-state HB-EGF concentration (colors correspond to scale-bar on the left, units ng/mL) for the initial, pre-collapse geometry (see blue contours in Fig. 7.7). White lines indicate finite element boundaries. LIS height and reservoir depth were both 15 microns. Parameters and boundary conditions: D_{LIS}=1.8 $\mu m^2/s$ and $D_{reservoir}$=D_{out}=75 $\mu m^2/s$; ligands constitutively shed into LIS from cell surface at a rate q=10 molecules/cell/min; ligand concentration was zero at the bottom of the reservoir; the most apical LIS surface and top layer of reservoir were impermeable walls.

To obtain concentration dynamics (as well as the steady-state case with zero velocities, Fig. 7.8), we solved the 3-D diffusion equation completely analogous to equations (3) and (5) of Chapter 3, only instead of using 1-D finite elements we employed 3-D finite elements (see white lines in Fig. 7.8). The governing 3-D transport equations (Bird et al., 2007; Deen, 1998) were

LIS: $$\frac{\partial C}{\partial t} = D_{LIS}\left(\frac{\partial^2 C}{\partial x^2}+\frac{\partial^2 C}{\partial y^2}+\frac{\partial^2 C}{\partial z^2}\right)-\left(V_x\frac{\partial C}{\partial x}+V_y\frac{\partial C}{\partial y}+V_z\frac{\partial C}{\partial z}\right)+q_v \quad (1a)$$

Reservoir: $$\frac{\partial C}{\partial t} = D_{out}\left(\frac{\partial^2 C}{\partial x^2}+\frac{\partial^2 C}{\partial y^2}+\frac{\partial^2 C}{\partial z^2}\right)-\left(V_x\frac{\partial C}{\partial x}+V_y\frac{\partial C}{\partial y}+V_z\frac{\partial C}{\partial z}\right) \quad (1b)$$

Here in equation (1a) the volumetric source term q_v=0, since the shedding of the ligand from the cell was expressed as a boundary condition, i.e. surface flux from the LIS boundary. As in the previous model (see Chapter 3) the diffusivity of the ligand in the LIS (hindered diffusion, D_{LIS}) could differ from the diffusivity in the reservoir (free diffusion, D_{out}). To solve equation (1), we first considered the 3-D velocity field (i.e. the velocities V_x, V_y, and V_z in equation (1)) based on the Navier-Stokes equations for water (a viscous, incompressible fluid) (Batchelor, 1967; Munson et al., 2002)

$$\rho\left(\frac{\partial V_i}{\partial t}+\frac{\partial V_i}{\partial x_k}V_k\right)=-\frac{\partial p}{\partial x_i}+\mu\frac{\partial^2 V_i}{\partial x_k \partial x_k} \qquad i=1,2,3;\ \text{sum on } k:\ k=1,2,3 \quad (2)$$

where ρ was water density, p fluid pressure, μ water viscosity, and the indices i and k each corresponded to the directions x, y, and z. To eliminate the fluid pressure p in equation (2), we employed the standard penalty method (Bathe, 1996; Filipovic et al., 2006) where we introduce a large parameter λ and approximate the continuity equation as

$$\frac{\partial V_i}{\partial x_i}+\frac{p}{\lambda}=0 \qquad \text{sum on } i:\ i=1,2,3 \quad (3)$$

Then, after substituting for the pressure p in equation (2) we obtain the modified Navier-Stokes equations (Filipovic et al., 2006)

$$\rho\left(\frac{\partial V_i}{\partial t}+\frac{\partial V_i}{\partial x_k}V_k\right)=\lambda\frac{\partial^2 V_k}{\partial x_i\partial x_k}+\mu\frac{\partial^2 V_i}{\partial x_k\partial x_k} \qquad i=1,2,3;\ \text{sum on } k:\ k=1,2,3 \tag{4}$$

After applying the standard Galerkin procedure (Huebner, 1975) to equation 4 we obtained the corresponding finite element equation (Filipovic et al., 2006):

$$\mathbf{M}\dot{\mathbf{V}}+\left(\mathbf{K}_{vv}+\mathbf{K}_{vv}^{\lambda}\right)\mathbf{V}=\mathbf{F}_{\lambda} \tag{5}$$

where

$$M_{KJ}=\int_V \rho N_K N_J dV \quad , \qquad \text{here } K,J=1,..,\text{number of nodes } N \tag{6}$$

$$\left[K_{KJ}\right]_{mn}=\left[\rho\int_V N_K N_{J,j}V_j dV\right]_{mm}+\rho\int_V N_K N_J V_{m,n}dV+\int_V \mu N_{K,j}N_{J,j}dV \quad , \tag{7}$$

$$\left(\mathbf{K}_{vv}^{\lambda}\right)_{KiJj}=\lambda\int_V N_{K,i}N_{J,j}dV \ , \tag{8}$$

$$\left(\mathbf{F}_{\lambda}\right)_{Ii}=\lambda\int_S N_I V_{j,j}n_i dS \tag{9}$$

In equations (6)-(9) N_K, N_J are the interpolation functions (see Chapters 2 & 3) and the notation $N_{J,j}$ indicates the spatial derivative of the interpolation functions in the j-direction, while the double index '*Ki*' means node '*K*' and component '*i*', and so on. The term n_i in equation 9 represents the unit normal in the i direction.

In parallel with solving the above equations for the fluid flow, we also solve governing finite element equations obtained from equation (1)

$$\hat{\mathbf{M}}\dot{\mathbf{C}}+\hat{\mathbf{K}}\mathbf{C}+\mathbf{K}_{Cv}\mathbf{V}=\mathbf{Q}^S \tag{10}$$

where

$$\hat{M}_{KJ} = \int_V N_K N_J \, dV \;,\; \hat{K}_{KJ} = \int_L D N_{K,i} N_{J,i} dV \;,\; Q_K^S = \int_S N_K q_S dS \tag{11}$$

and

$$\mathbf{K}_{Cv} = \left[(\mathbf{K}_{Cv})_1 (\mathbf{K}_{Cv})_2 (\mathbf{K}_{Cv})_3 \right] \;\;,\;\; (\mathbf{K}_{Cv})_{KJi} = \int_V \frac{\partial C}{\partial x_i} N_K N_J dV \tag{12}$$

The above equations were then solved incrementally and iteratively using the software package PAK-F (Kojic et al., 1998) for both the steady-state (zero velocity) case of Fig. 7.8 and during a collapse. In order to investigate how ligand concentrations (and the velocity field) vary during a collapse, we incorporated the geometry 20s after the application of a transcellular pressure gradient of 30cmH_2O (see red contours in Fig. 7.7). We assumed that between t=0 and 20s the position of each node (i.e. marker in Fig. 7.7) changed linearly with time, meaning that if the coordinates of a node were (x0,y0) at t=0 and (x20,y20) at t=20s then at t=10s the node was half-way in between at ((x20-x0)/2,(y20-y0)/2). This approach yielded LIS geometries for each time step and hence we could track each finite element node's position through time.

To solve for the velocity field of the fluid (equations 4-9) we assumed the following: 1) the velocity of the LIS wall was equal to the velocity of the fluid at the wall boundary, 2) the most apical LIS surface and the top of the reservoir were impermeable walls, and 3) all of the fluid that gets squeezed out the LIS appears in the reservoir. The solved velocity field at the end of the collapse (i.e. at t=20s, corresponding to a change in geometry from the blue to the red contours in Fig. 7.7) is shown in vector form in Fig. 7.9.

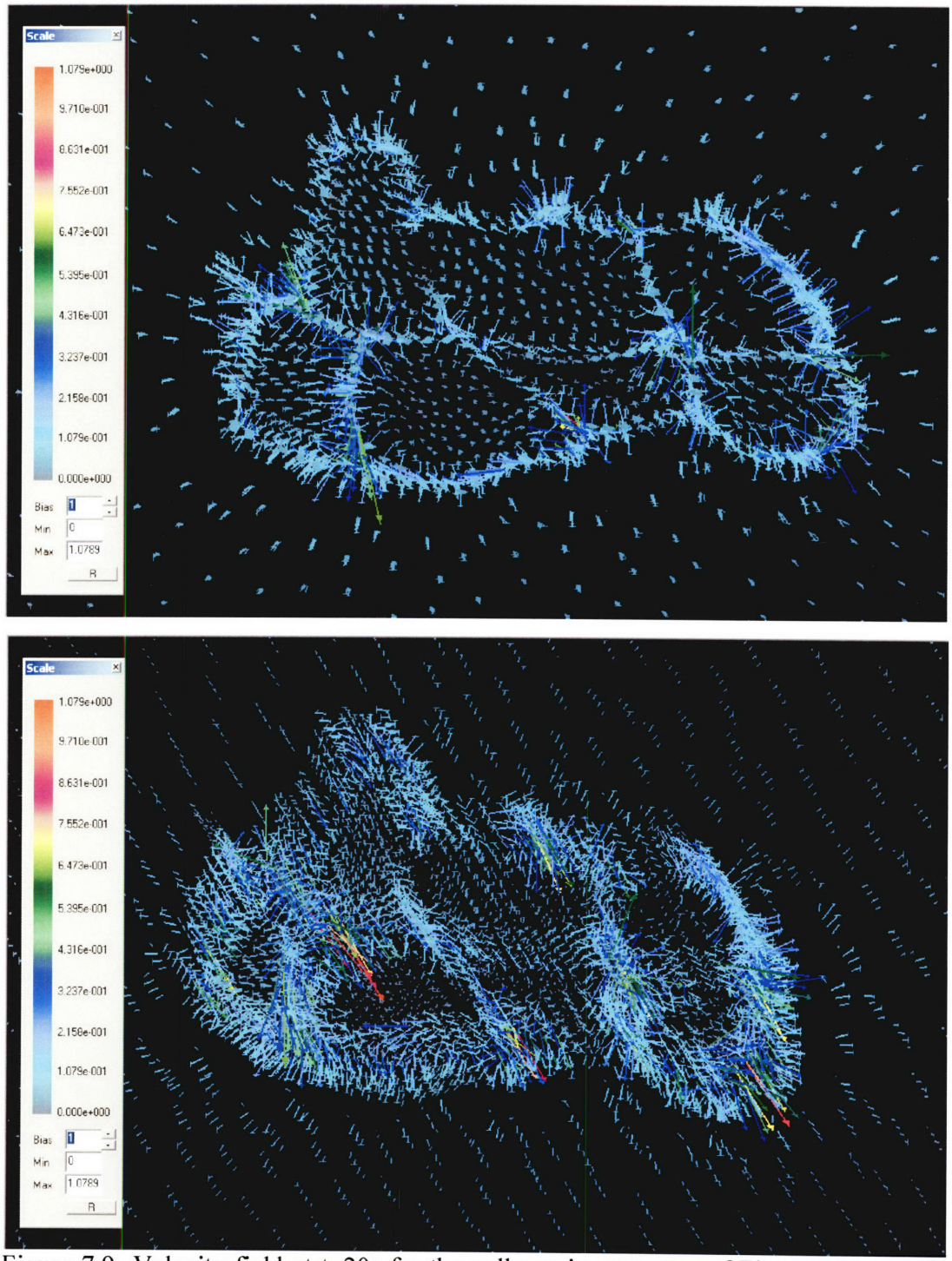

Figure 7.9 Velocity field at t=20s for the collapse in geometry of Fig. 7.7. Top: a top-down view along the apico-basal axis of the velocity vectors. Bottom: side view. Scale bar: velocity in microns/second.

In parallel we solved for the concentration field (equations (1), (10)-(12)) and show the results at the end of the collapse, i.e. t=20s, in Fig. 7.10.

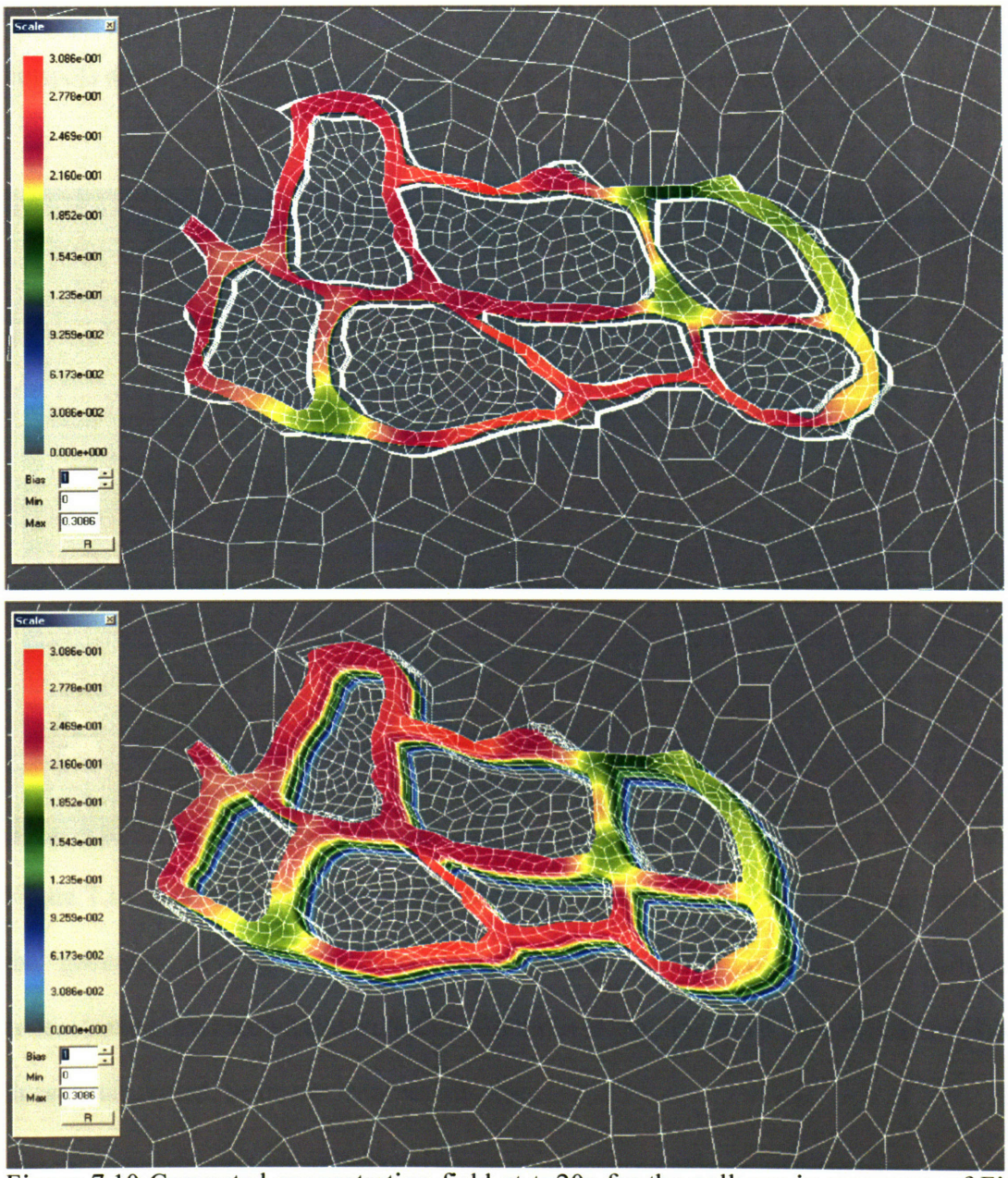

Figure 7.10 Computed concentration field at t=20s for the collapse in geometry of Fig. 7.7. Top: a top-down view along the apico-basal axis, white boundaries indicate the t=0 geometry (blue contours in Fig. 7.7), whereas color boundaries correspond to the t=20s geometry (red contours in Fig. 7.8). Bottom: side view. Scale bar: concentration (ng/mL).

The previous results were based on a 20s collapse in LIS geometry according to Fig. 7.7. We also examined what would be the effect on concentration of a faster 1s collapse, for the same geometry (see Fig. 7.11). Apparent in the figure are concentration hotspots due to the velocity field formed by the rapid collapse (see Fig. 7.12).

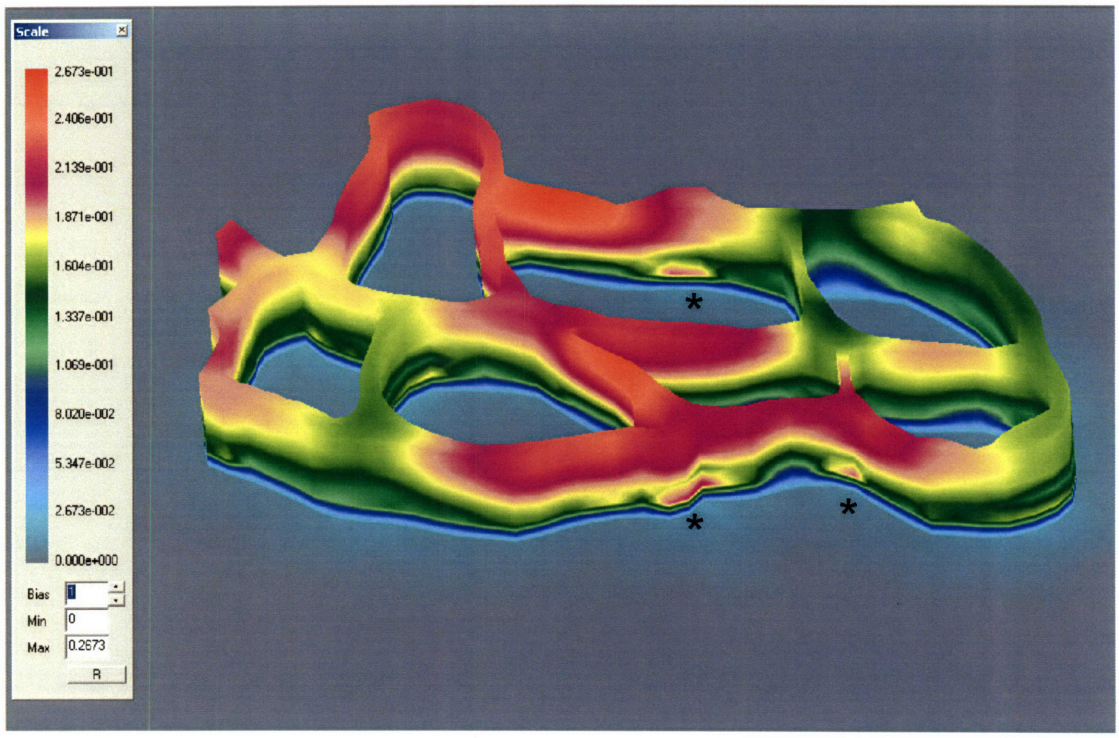

Figure 7.11 Side view of the calculated concentration field at the end of a 1s collapse for the geometry of Fig. 7.7. Stars indicate three hotspots (zones with increased concentration) that are visible from this view. For clarity, the finite element mesh (white lines) was omitted. Scale bar: concentration (ng/mL).

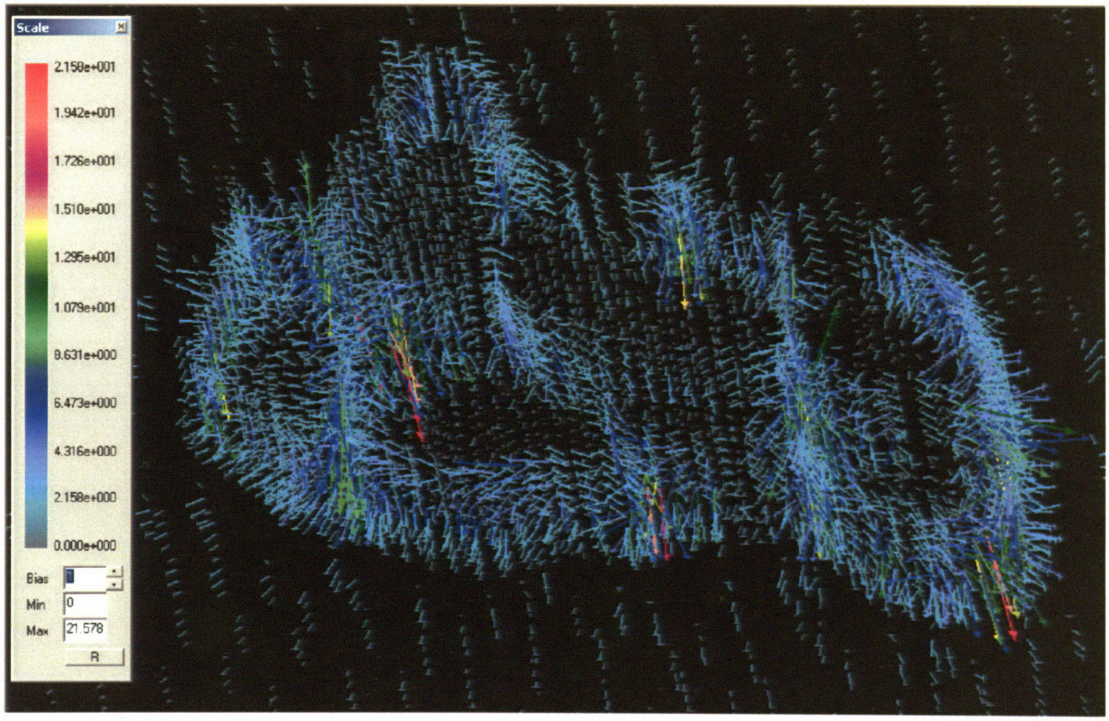

Figure 7.12 Side view of the velocity field at the end of a 1s collapse for the Fig. 7.7 geometry. Scale bar: velocity (μm/s).

The above Figures 7.8, 7.10-11 indicate only the ligand concentration at the LIS boundary, thus to examine in more detail the concentration within a LIS we graphically displayed the concentration field for a prescribed segment of Fig. 7.11. This meant that we cut with planes parallel to the apico-basal axis (see Fig. 7.13). As the top panel of Fig. 7.13 indicates, the cutting planes went along the boundaries of finite elements (hence the jagged-edge appearance). The bottom panel shows the segment in the apico-basal plane, from a viewpoint that runs through an imaginary line connecting the two stars in the top panel. The stars represent corresponding locations in the two views of Fig. 7.13, and the non-uniform zones (e.g. above the red star in bottom panel) indicate concentration hotspots where, largely due to convective effects, a local increase in concentration occurs.

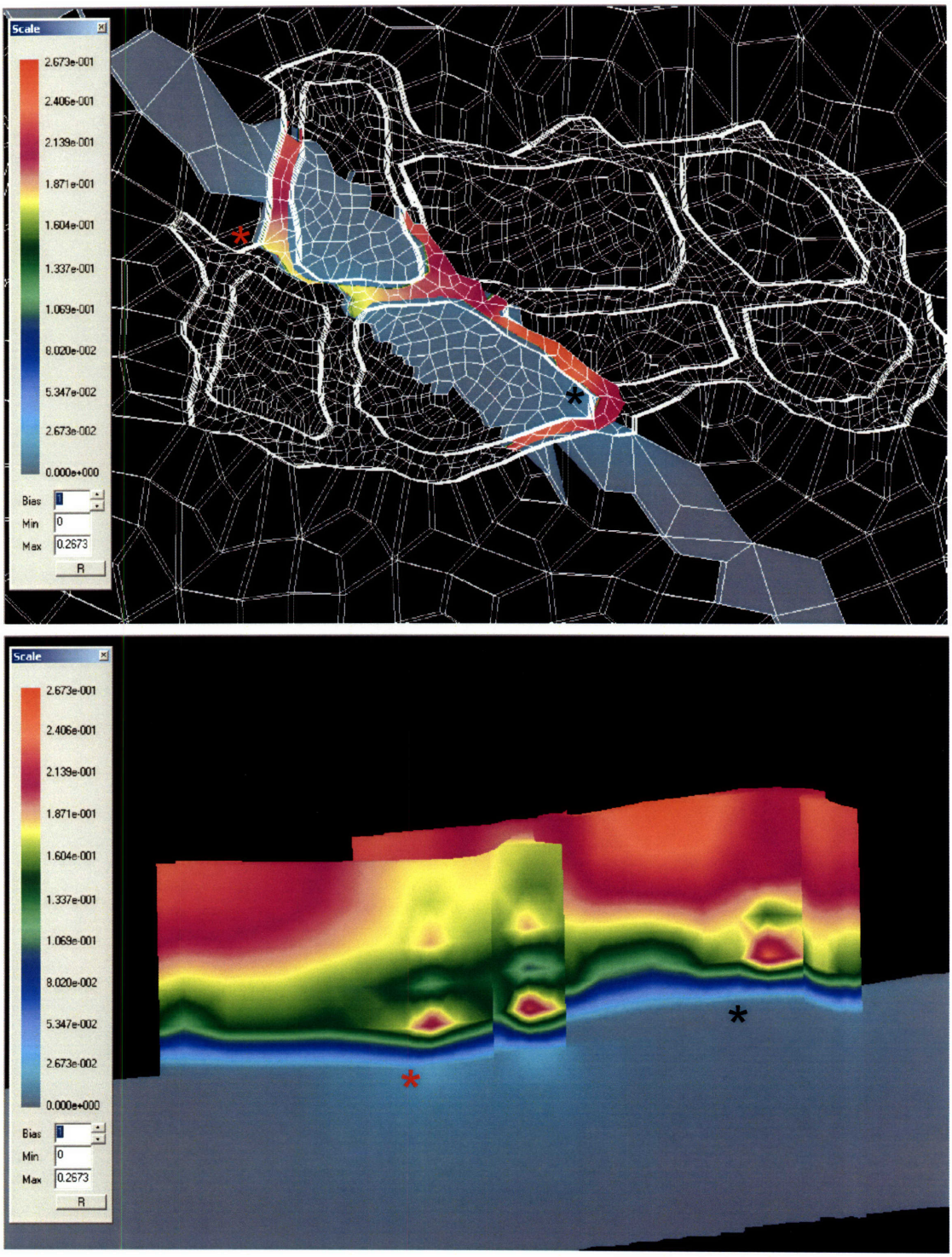

Figure 7.13 A segment of Fig. 7.11. Top: top-down view of the selected segment. FE mesh (white lines) included to indicate where the segment was chosen. Bottom: enlarged, side view of the segment. Stars represent the corresponding locations in the two views.

The non-uniform zones in the bottom panel (e.g. above the red star) indicate concentration hotspots.

In all of the above results we calculated the absolute concentration values, however of biological importance is the change in concentration relative to baseline (e.g. normalized mean LIS concentration obtained from the 2-D model). Thus, for both of the cases $t_{collapse}$=1s and $t_{collapse}$=20s we plotted the difference between the current concentration field and the initial, pre-collapse concentration (see Fig. 7.14). The figure employed identical scale bars, thus the magnitudes of the relative concentrations (i.e. colors) can be compared between the top ($t_{collapse}$=1s) and bottom ($t_{collapse}$=20s) panels. The top panel of Fig. 7.14 was obtained by subtracting Fig. 7.8 (the pre-collapse t=0 concentrations) from Fig. 7.11 (concentrations at the end of a 1s collapse), while the bottom panel represents the difference between Fig. 7.10 (concentrations at the end of a 20s collapse) and Fig. 7.8. By comparing the two panels of Fig. 7.14 it is apparent that the 1s collapse has a more dramatic effect on the change in concentration profiles. The rapid collapse causes the formation of concentration hotspots (see Figs. 7.11&14), whereas the slower 20s collapse roughly maintains the parabolic concentration profile along the apico-basal LIS axis (see Figs. 7.10&14). The latter can be seen in the bottom panel of Fig. 7.14, where the nearly uniform coloring indicates a relatively constant increase in concentration for the slower 20s collapse. This constant increase was largely due to the small convective effect, i.e. small velocities generated by the slower LIS collapse.

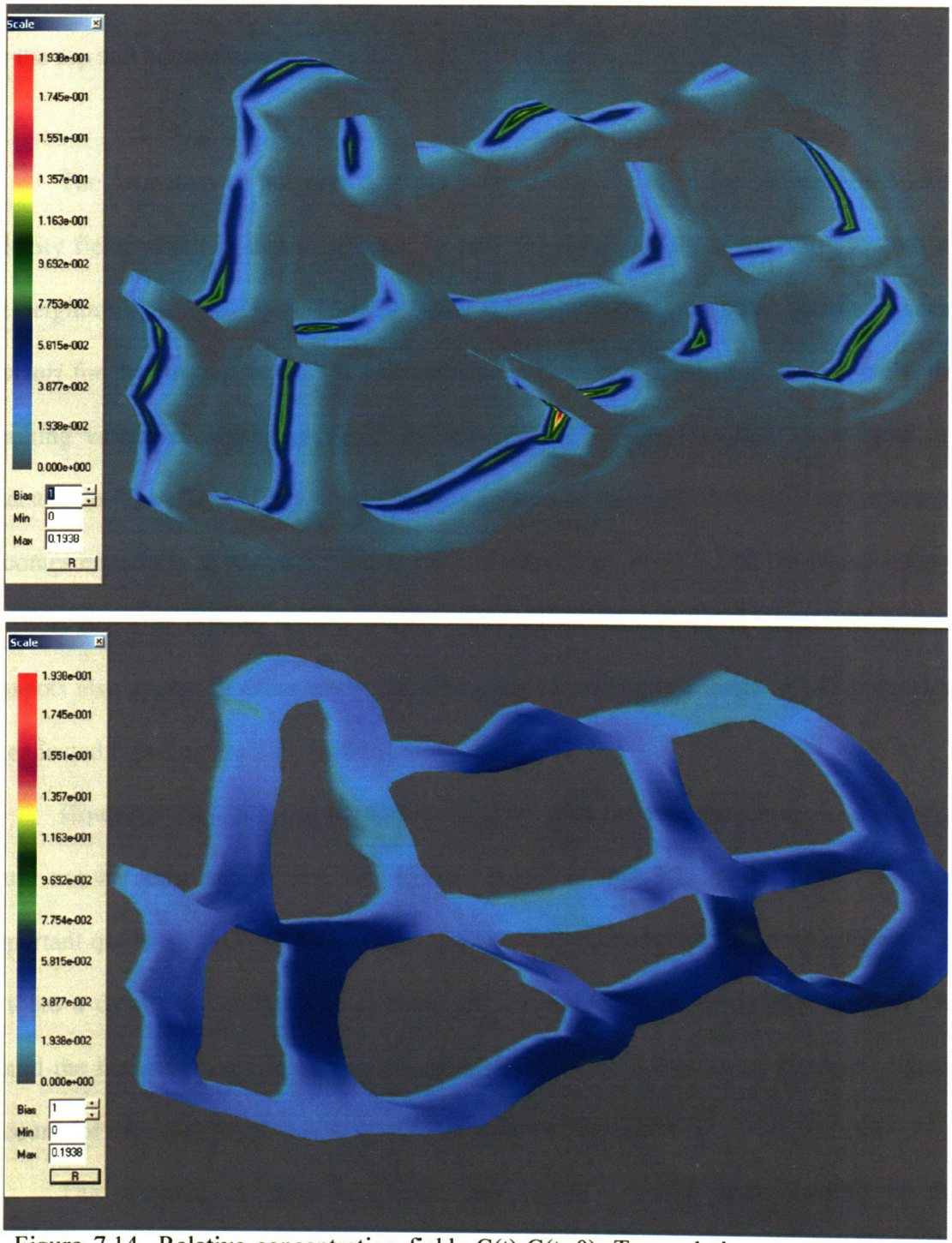

Figure 7.14 Relative concentration fields C(t)-C(t=0). Top: relative concentrations at the end of a 1s collapse (non-uniform areas indicate concentration hotspots). Bottom: relative concentrations at the end of a 20s collapse. Scale bars (concentration in ng/mL)

are identical, thus colors can be used for comparison between the relative concentrations for the top and bottom panels.

The formation of hotspots (see top panel of Fig. 7.14) is dependent on the local velocity field, which in turn is affected by both the local change in geometry as well as the neighboring LIS collapse. The calculated velocity field was complex and not evident *a priori* for the heterogenous 3-D LIS collapse. At the intersections of several cells, the resulting velocities depend on all of the surrounding LIS regions that "flow" into the intersection. The effect of interconnected LIS channels that collapse by different amounts becomes especially apparent for the rapid 1s collapse (see Figs. 7.11&14) where intense hotspots occur at regions where several LIS regions connect at an angle. Of course, hotspots also appear in areas where there is a drastic and rapid change in LIS geometry, as expected based on the 2-D model results.

However, LIS interconnectedness coupled with the inhomogenous LIS collapse could not be addressed by the 2-D model. Therefore, the 3-D model raises new and important questions such as: What is the biological significance of the local hotspots, e.g. is there a dynamical and/or kinetic range for the induction of the intracellular signal? Could the hotspots cause highly localized signaling? Could then these localized signals account for the majority of the measured intracellular response?

The answers to these questions may yield a better understanding of the mechanotransduction process in airway epithelial cells. This knowledge could then be used to design more localized and targeted pharmacogenetic therapeutic agents aimed at hindering unwanted activation of the asthmatic epithelium.

8. Conclusions

How airway epithelial cells sense and transduce mechanical stimuli is a complex and not fully understood process that could play a role in airway remodeling often associated with asthma and other airway diseases. In this thesis, we examined cultured normal human bronchial epithelial (NHBE) cells that were exposed to a transcellular pressure gradient as a model for the mechanical stimulus that a cell experiences during bronchoconstriction. The mechanotransduction process involves functional autocrine loops, consisting of ligands, produced by the cells and shed into the lateral intercellular space (LIS), and the corresponding ligand receptor (also made by the cell and found on the cell surface). In the NHBE cells, the key ligand-receptor mechanotransduction pair is EGFR and HB-EGF.

We attempted to measure the basal (and pressure-induced) shedding rates of three EGFR ligands: TGF-alpha, EGF, and HB-EGF. The only detectable rate was for TGF-alpha, being about 22 molecules/cell/hour, whereas EGF was close to the detection limit at about 1 molecule/cell/hour, and HB-EGF was well below the detection limit. For TGF-alpha, the application of a transcellular pressure gradient equal to 30 cmH_2O increased the shedding rate by nearly 50% to 31 molecules/cell/hour.

Besides the shedding measurements, we focused mostly on how a collapse in the compliant LIS, due to the applied compressive stress, affects calculated ligand concentrations in the LIS. The analysis of ligand dynamics consisted of two interconnected parts: numerical modeling and experimental imaging. The evolution of three generations of numerical models was presented: a 2-D model based on pure diffusion (no convection), a dynamic diffusion-convection 2-D model which included the

space below the LIS, and finally a 3-D model whose geometry was obtained directly from imaging. The experimental imaging involved the use of a custom-built high-speed two photon microscope that enabled the acquisition of real-time high-resolution images of the entire LIS during a pressure induced collapse. To quantify how much the LIS geometry changed we developed an automated multi-step image-analysis algorithm which relied on the adaptive thresholding method. The algorithm enabled the determination of LIS volume collapse curves (i.e. LIS volume vs. time) for a variety of conditions. The cells we used were primary cultures of human airway epithelia from different donors, and testing different donors suggested that there is great variability in cell "collapsibility" among the various donors, while for a given a donor the results were reproducible. Since we do not know if any of the donors were asthmatic, i.e. donations were anonymous, we cannot relate the response to pressure to any clinical or physiological conditions. It is tempting, however, to speculate that if cells with a collapsible LIS *in vitro* manifest the same characteristics *in vivo*, that such cells would be more likely to be remodeled as a result of a bronchoconstrictor insult.

The obtained collapse curves were then used as direct input into the diffusion-convection 2-D model. The output of the model (i.e. the ligand concentration dynamics) could only partly explain corresponding biochemical data of EGFR phosphorylation (pEGFR) during pressure application. An initial rise in ligand concentration mirrored an increase in EGFR activation during the first 180s of the collapse, but then the measured EGFR phosphorylation decreased whilst the predicted ligand concentration kept increasing toward a plateau value. About 80% of the total LIS collapse occurred within the first 180s suggesting that this initial surge could be the onset of signaling. The

discrepancy between the modeled ligand dynamics and the measured pEGFR curve could be due to the lack of presence of receptors in the model.

The final generation model was a 3-D model whose geometry was determined directly from analyzed collapsed images (one at t=0 and one at t=20s into the collapse). The 3-D model captured inhomogeneities of the LIS collapse for a group of seven cells. Since each LIS collapsed somewhat differently, the cumulative effect on the velocity field, directly coupled to the concentration field, was the appearance of localized high concentration regions. For the same geometry, but a hypothetical, rapid 1s collapse the concentration hotspots became even more apparent. These results indicate that LIS interconnectedness coupled with the heterogenous LIS collapse could induce the formation of highly localized and complex signaling hotspots. Understanding how signaling hotspots function and affect intracellular responses could provide more insight into the mechanotransduction process. This insight could then one day be applied to the design of novel pharmacogenetic therapeutics aimed at preventing airway over-activation and potentially hindering the progression of airway remodeling in asthmatic patients.

References:

Batchelor, G. K. (1967). An introduction to fluid dynamics. Cambridge,: U. P.

Bathe, K.-J. (1996). Finite element procedures. Englewood Cliffs, N.J.: Prentice Hall.

Bird, R. B., Stewart, W. E. and Lightfoot, E. N. (2007). Transport phenomena. New York: John Wiley & Sons.

Chow, C. K. and Kaneko, T. (1972). Automatic boundary detection of the left ventricle from cineangiograms. *Comput Biomed Res* **5**, 388-410.

Chu, E. K., Foley, J. S., Cheng, J., Patel, A. S., Drazen, J. M. and Tschumperlin, D. J. (2005). Bronchial epithelial compression regulates epidermal growth factor receptor family ligand expression in an autocrine manner. *Am J Respir Cell Mol Biol* **32**, 373-80.

Deen, W. M. (1998). Analysis of transport phenomena. New York: Oxford University Press.

DeWitt, A., Iida, T., Lam, H. Y., Hill, V., Wiley, H. S. and Lauffenburger, D. A. (2002). Affinity regulates spatial range of EGF receptor autocrine ligand binding. *Dev Biol* **250**, 305-16.

DeWitt, A. E., Dong, J. Y., Wiley, H. S. and Lauffenburger, D. A. (2001). Quantitative analysis of the EGF receptor autocrine system reveals cryptic regulation of cell response by ligand capture. *J Cell Sci* **114**, 2301-13.

Dong, J., Opresko, L. K., Dempsey, P. J., Lauffenburger, D. A., Coffey, R. J. and Wiley, H. S. (1999). Metalloprotease-mediated ligand release regulates autocrine signaling through the epidermal growth factor receptor. *Proc Natl Acad Sci U S A* **96**, 6235-40.

Dong, J. and Wiley, H. S. (2000). Trafficking and proteolytic release of epidermal growth factor receptor ligands are modulated by their membrane-anchoring domains. *J Biol Chem* **275**, 557-64.

Dowd, C. J., Cooney, C. L. and Nugent, M. A. (1999). Heparan sulfate mediates bFGF transport through basement membrane by diffusion with rapid reversible binding. *J Biol Chem* **274**, 5236-44.

Evans, M. J., Van Winkle, L. S., Fanucchi, M. V. and Plopper, C. G. (2001). Cellular and molecular characteristics of basal cells in airway epithelium. *Exp Lung Res* **27**, 401-15.

Filipovic, N., Mijailovic, S., Tsuda, A. and Kojic, M. (2006). An implicit algorithm within the arbitrary Lagrangian-Eurlerian formulation for solving incompressible fluid flow with large boundary motions. *Comp Meth Appl Mech Eng* **95**, 6347-6361.

Forsyth, D. A. and Ponce, J. (2003). Computer vision: A modern approach. Upper Saddle River, NJ: Prentice Hall.

Freeman, M. and Gurdon, J. B. (2002). Regulatory principles of developmental signaling. *Annu Rev Cell Dev Biol* **18**, 515-39.

Fung, Y. C. (1981). Biomechanics, mechanical properties of living tissues. New York: Springer-Verlag.

Gonzalez, R. C. and Woods, R. E. (2002). Digital image processing. Upper Saddle River, NJ: Prentice Hall.

Harris, R. C., Chung, E. and Coffey, R. J. (2003). EGF receptor ligands. *Exp Cell Res* **284**, 2-13.

Haslach, H. W., Jr. (2005). Nonlinear viscoelastic, thermodynamically consistent, models for biological soft tissue. *Biomech Model Mechanobiol* **3**, 172-89.

Hrousis, C. A., Wiggs, B. J., Drazen, J. M., Parks, D. M. and Kamm, R. D. (2002). Mucosal folding in biologic vessels. *J Biomech Eng* **124**, 334-41.

Huebner, K. H. (1975). The finite element method for engineers. New York: John Wiley and Sons.

Hughes, T. J. R. (1987). The finite element method. Linear static and dynamic finite element analysis. Englewood Cliffs, N. J.: Prentice Hall.

Jones, J. T., Akita, R. W. and Sliwkowski, M. X. (1999). Binding specificities and affinities of egf domains for ErbB receptors. *FEBS Lett* **447**, 227-31.

Kholodenko, B. N., Demin, O. V., Moehren, G. and Hoek, J. B. (1999). Quantification of short term signaling by the epidermal growth factor receptor. *J Biol Chem* **274**, 30169-81.

Kim, K. H., Buehler, C. and So, P. T. C. (1999). High-speed, two-photon scanning microscope. *Applied Optics* **38**, 6004-6009

Koay, E. J., Shieh, A. C. and Athanasiou, K. A. (2003). Creep indentation of single cells. *J Biomech Eng* **125**, 334-41.

Kojic, M. and Bathe, K.-J. (2005). Inelastic analysis of solids and structures. Berlin: Springer-Verlag.

Kojic, M., Filipovic, N., Slavkovic, R., Zivkovic, M. and Grujovic, N. (1998). PAK-F Finite Element Program for Laminar Flow with Mass and Heat Transfer. *University of Kragujevac, Serbia.*

Kojic, M., Slavkovic, R., Zivkovic, M. and Grujovic, N. (1997). PAK-T Finite Element Program for Linear and Nonlinear Heat Conduction. *University of Kragujevac, Serbia.*

Kojic, N., Kojic, M. and Tschumperlin, D. J. (2006). Computational modeling of extracellular mechanotransduction. *Biophys J* **90**, 4261-70.

Kovbasnjuk, O. N., Bungay, P. M. and Spring, K. R. (2000). Diffusion of small solutes in the lateral intercellular spaces of MDCK cell epithelium grown on permeable supports. *J Membr Biol* **175**, 9-16.

Lauffenburger, D. A. and Linderman, J. J. (1993). Receptors: Models for Binding, Trafficking, and Signaling: Oxford University Press.

Lauffenburger, D. A., Oehrtman, G. T., Walker, L. and Wiley, H. S. (1998). Real-time quantitative measurement of autocrine ligand binding indicates that autocrine loops are spatially localized. *Proc Natl Acad Sci U S A* **95**, 15368-73.

Lee, S. and Hayes, M. H. (2001). Scene change detection using adaptive threshold and sub-macroblock images in compressed sequences. In *2001 IEEE International Conference on Multimedia and Expo*, pp. 53-56.

Maheshwari, G., Wiley, H. S. and Lauffenburger, D. A. (2001). Autocrine epidermal growth factor signaling stimulates directionally persistent mammary epithelial cell migration. *J Cell Biol* **155**, 1123-8.

Monine, M. I., Berezhkovskii, A. M., Joslin, E. J., Wiley, H. S., Lauffenburger, D. A. and Shvartsman, S. Y. (2005). Ligand accumulation in autocrine cell cultures. *Biophys J* **88**, 2384-90.

Munson, B. R., Young, D. F. and Okiishi, T. H. (2002). Fundamentals of fluid mechanics. New York: Wiley.

Oehrtman, G. T., Wiley, H. S. and Lauffenburger, D. A. (1998). Escape of autocrine ligands into extracellular medium: experimental test of theoretical model predictions. *Biotechnol Bioeng* **57**, 571-82.

Ohya, J., Shio, A. and Akamatsu, S. (1994). Recognizing characters in scene images. *IEEE Transactions on Pattern Analysis and Machine Intelligence* **16**, 214-220.

Raab, G. and Klagsbrun, M. (1997). Heparin-binding EGF-like growth factor. *Biochimica et Biophysica Acta* **1333**, F179-F199.

Resat, H., Ewald, J. A., Dixon, D. A. and Wiley, H. S. (2003). An integrated model of epidermal growth factor receptor trafficking and signal transduction. *Biophys J* **85**, 730-43.

Ressler, B., Lee, R. T., Randell, S. H., Drazen, J. M. and Kamm, R. D. (2000). Molecular responses of rat tracheal epithelial cells to transmembrane pressure. *Am J Physiol Lung Cell Mol Physiol* **278**, L1264-72.

Sasagawa, S., Ozaki, Y., Fujita, K. and Kuroda, S. (2005). Prediction and validation of the distinct dynamics of transient and sustained ERK activation. *Nat Cell Biol* **7**, 365-73.

Schoeberl, B., Eichler-Jonsson, C., Gilles, E. D. and Muller, G. (2002). Computational modeling of the dynamics of the MAP kinase cascade activated by surface and internalized EGF receptors. *Nat Biotechnol* **20**, 370-5.

Shvartsman, S. Y., Hagan, M. P., Yacoub, A., Dent, P., Wiley, H. S. and Lauffenburger, D. A. (2002a). Autocrine loops with positive feedback enable context-dependent cell signaling. *Am J Physiol Cell Physiol* **282**, C545-59.

Shvartsman, S. Y., Muratov, C. B. and Lauffenburger, D. A. (2002b). Modeling and computational analysis of EGF receptor-mediated cell communication in Drosophila oogenesis. *Development* **129**, 2577-89.

Shvartsman, S. Y., Wiley, H. S., Deen, W. M. and Lauffenburger, D. A. (2001). Spatial range of autocrine signaling: modeling and computational analysis. *Biophys J* **81**, 1854-67.

Stamenovic, D., Fredberg, J. J., Wang, N., Butler, J. P. and Ingber, D. E. (1996). A microstructural approach to cytoskeletal mechanics based on tensegrity. *J Theor Biol* **181**, 125-36.

Swartz, M. A., Tschumperlin, D. J., Kamm, R. D. and Drazen, J. M. (2001). Mechanical stress is communicated between different cell types to elicit matrix remodeling. *Proc Natl Acad Sci U S A* **98**, 6180-5.

Tschumperlin, D. J., Dai, G., Maly, I. V., Kikuchi, T., Laiho, L. H., McVittie, A. K., Haley, K. J., Lilly, C. M., So, P. T., Lauffenburger, D. A. et al. (2004). Mechanotransduction through growth-factor shedding into the extracellular space. *Nature* **429**, 83-6.

Tschumperlin, D. J. and Drazen, J. M. (2001). Mechanical stimuli to airway remodeling. *Am J Respir Crit Care Med* **164**, S90-4.

Tschumperlin, D. J., Shively, J. D., Swartz, M. A., Silverman, E. S., Haley, K. J., Raab, G. and Drazen, J. M. (2002). Bronchial epithelial compression regulates MAP

kinase signaling and HB-EGF-like growth factor expression. *Am J Physiol Lung Cell Mol Physiol* **282**, L904-11.

Vinante, F., Marchi, M., Rigo, A., Scapini, P., Pizzolo, G. and Cassatella, M. A. (1999). Granulocyte-macrophage colony-stimulating factor induces expression of heparin-binding epidermal growth factor-like growth factor/diphtheria toxin receptor and sensitivity to diphtheria toxin in human neutrophils. *Blood* **94**, 3169-77.

Wiggs, B. R., Hrousis, C. A., Drazen, J. M. and Kamm, R. D. (1997). On the mechanism of mucosal folding in normal and asthmatic airways. *J Appl Physiol* **83**, 1814-21.

Wiley, H. S., Shvartsman, S. Y. and Lauffenburger, D. A. (2003). Computational modeling of the EGF-receptor system: a paradigm for systems biology. *Trends Cell Biol* **13**, 43-50.

Willumsen, N. J., Davis, C.W., and Boucher, R.C. (1994). Selective response of human airway epithelia to luminal but not serosal solution hypertonicity. *Journal of Clinical Investigation* **94**, 779-787.

Xia, P., Bungay, P. M., Gibson, C. C., Kovbasnjuk, O. N. and Spring, K. R. (1998). Diffusion coefficients in the lateral intercellular spaces of Madin-Darby canine kidney cell epithelium determined with caged compounds. *Biophys J* **74**, 3302-12.

Yarden, Y. and Sliwkowski, M. X. (2001). Untangling the ErbB signalling network. *Nat Rev Mol Cell Biol* **2**, 127-37.